1-1-2015

Load-Independent And Regional Measures Of Cardiac Function Via Real-Time Mri

Francisco Contijoch
University of Pennsylvania, francisco.contijoch@gmail.com

Load-Independent And Regional Measures Of Cardiac Function Via Real-Time Mri

Abstract
LOAD-INDEPENDENT AND REGIONAL MEASURES OF CARDIAC FUNCTION VIA REAL-TIME MRI

Francisco Jose Contijoch

Robert C Gorman, MD

Expansion of infarcted tissue during left ventricular (LV) remodeling after a myocardial infarction is associated with poor long-term prognosis. Several interventions have been developed to limit infarct expansion by modifying the material properties of the infarcted or surrounding borderzone tissue.

Measures of myocardial function and material properties can be obtained non-invasively via imaging. However, these measures are sensitive to variations in loading conditions and acquisition of load-independent measures have been limited by surgically invasive procedures and limited spatial resolution.

In this dissertation, a real-time magnetic resonance imaging (MRI) technique was validated in clinical patients and instrumented animals, several technical improvements in MRI acquisition and reconstruction were presented for improved imaging resolution, load-independent measures were obtained in animal studies via non-invasive imaging, and regional variations in function were measured in both naïve and post-infarction animals.

Specifically, a golden-angle radial MRI acquisition with non-Cartesian SENSE-based reconstruction with an exposure time less than 95 ms and a frame rate above 89 fps allows for accurate estimation of LV slice volume in clinical patients and instrumented animals. Two technical developments were pursued to improve image quality and spatial resolution. First, the slice volume obtained can be used as a self-navigator signal to generate retrospectively-gated, high-resolution datasets of multiple beat morphologies. Second, cross-correlation of the ECG with previously observed values resulted in accurate interpretation of cardiac phase in patients with arrhythmias and allowed for multi-shot imaging of dynamic scenarios.

Synchronizing the measured LV slice volume with an LV pressure signal allowed for pressure-volume loops and corresponding load-independent measures of function to be obtained in instrumented animals. Acquiring LV slice volume at multiple slice locations revealed regional differences in contractile function. Motion-tracking of the myocardium during real-time imaging allowed for differences in contractile function between normal, borderzone, and infarcted myocardium to be measured.

Lastly, application of real-time imaging to patients with arrhythmias revealed the variable impact of ectopic beats on global hemodynamic function, depending on frequency and ectopic pattern.

This work established the feasibility of obtaining load-independent measures of function via real-time MRI and illustrated regional variations in cardiac function.

Degree Type
Dissertation

LOAD-INDEPENDENT AND REGIONAL MEASURES OF CARDIAC FUNCTION VIA REAL-TIME MRI

Francisco Jose Contijoch

A DISSERTATION

in

Bioengineering

Presented to the Faculties of the University of Pennsylvania in

Partial Fulfillment of the Requirements for the

Degree of Doctor of Philosophy

2015

Supervisor of Dissertation	Graduate Group Chairperson
Robert C. Gorman, M.D.	Jason A Burdick, Ph.D.
Professor of Surgery	Professor, Department of Bioengineering

Dissertation Committee:

Yuchi Han, M.D., MMsc, Assistant Professor of Medicine (Cardiology)

Kenneth Margulies, M.D., Professor of Medicine (Cardiology, Transplant)

Ravinder Reddy, Ph.D., Professor of Radiology

Hee Kwon Song, Ph.D., Associate Professor of Radiology

Walter RT Witschey, Ph.D., Assistant Professor of Radiology

Paul Yushkevich, Ph.D., Assistant Professor of Radiology

LOAD-INDEPENDENT AND REGIONAL MEASURES OF CARDIAC FUNCTION VIA REAL-TIME MRI

“To my parents Carmen and Frank, my brother Eduardo, and my wife Paige.”

Acknowledgements

I would like to thank everyone who helped me reach this point. First and foremost, I thank my advisor, Dr. Robert Gorman, for his mentorship. His guidance and support allowed me to pursue my interests and encouraged me to take risks.

I am thankful to the truly interdisciplinary thesis committee of Professors Hee Kwon Song, Yuchi Han, Kenneth Margulies, Ravinder Reddy, Walter Witschey, and Paul Yushkevich. Their wide-ranging expertise, insights, and guidance were invaluable to this effort. I especially thank Walter Witschey. This project would not have been possible without his patience during my summer research rotation in the Gorman Cardiovascular Group and his subsequent guidance and dedication to the projects in this thesis.

I would like to thank the entire Gorman Cardiovascular Research Group. The team of surgeons, surgery residents, and veterinary and radiology technicians were critical to the animal studies in this thesis, especially Christen Dillard, Joyce Han Madonna Lee, Jeremy McGarvey, and Jerry Zsido. Jim Pilla provided vital help with the design and interpretation of the animal studies as well as numerous fruitful conversations throughout my dissertation.

My thanks also go to the HHMI Interfaces Program leadership for providing me the opportunity to be a part of such a unique and innovative curriculum. My experience in the program was made even more enjoyable thanks to my fellow students, especially Matt Churgin, Shauna Dorsey, Erin Englund, Ben Kandel, Feliks Kogan, Alison Pouch, Alan Seifert, and Sarmad Siddiqui.

None of this would have been possible without the love and support of my friends and family, especially my parents Carmen and Frank, my grandparents, Lourdes, Jose, Virginia, and Francisco, my brother Eduardo, and my best friend Robert.

I am thankful for my wife Paige, especially her foolishness in marrying me, her patience during my studies, and her enthusiasm about what the future holds. She inspires me everyday to be better and do more.

ABSTRACT

LOAD-INDEPENDENT AND REGIONAL MEASURES OF CARDIAC FUNCTION VIA REAL-TIME MRI

Francisco Jose Contijoch

Robert C Gorman, MD

Expansion of infarcted tissue during left ventricular (LV) remodeling after a myocardial infarction is associated with poor long-term prognosis. Several interventions have been developed to limit infarct expansion by modifying the material properties of the infarcted or surrounding borderzone tissue.

Measures of myocardial function and material properties can be obtained non-invasively via imaging. However, these measures are sensitive to variations in loading conditions and acquisition of load-independent measures have been limited by surgically invasive procedures and limited spatial resolution.

In this dissertation, a real-time magnetic resonance imaging (MRI) technique was validated in clinical patients and instrumented animals, several technical improvements in MRI acquisition and reconstruction were presented for improved imaging resolution, load-independent measures were obtained in animal studies via non-invasive imaging, and regional variations in function were measured in both naïve and post-infarction animals.

Specifically, a golden-angle radial MRI acquisition with non-Cartesian SENSE-based reconstruction with an exposure time less than 95 ms and a frame rate above 89 fps allows for accurate estimation of LV slice volume in clinical patients and instrumented animals. Two technical developments were pursued to improve image quality and spatial resolution. First, the slice volume obtained can be used as a self-navigator signal to generate retrospectively-gated, high-resolution datasets of multiple beat morphologies. Second, cross-correlation of the ECG with previously observed values resulted in accurate interpretation of cardiac phase in patients with arrhythmias and allowed for multi-shot imaging of dynamic scenarios.

Synchronizing the measured LV slice volume with an LV pressure signal allowed for pressure-volume loops and corresponding load-independent measures of function to be obtained in instrumented animals. Acquiring LV slice volume at multiple slice locations revealed regional differences in contractile function. Motion-tracking of the myocardium during real-time imaging allowed for differences in contractile function between normal, borderzone, and infarcted myocardium to be measured.

Lastly, application of real-time imaging to patients with arrhythmias revealed the variable impact of ectopic beats on global hemodynamic function, depending on frequency and ectopic pattern.

This work established the feasibility of obtaining load-independent measures of function via real-time MRI and illustrated regional variations in cardiac function.

Table of Contents

List of Tables

List of Figures

Preface

Chapter 4 has been published as: Contijoch F, Witschey WR, Rogers K, Rears H, Hansen MS, Yushkevich PA, et al. User-Initialized Active Contour Segmentation and Golden-angle Real-Time Cardiac MRI Enable Accurate Assessment of LV Function in Patients with Sinus Rhythm and Arrhythmias. J Cardiovasc Magn Reson. 2015;17(37):In Press DOI: 10.1186/s12968-015-0146-9

Chapter 5 has been presented as *Non-Cartesian Retrospective Reconstruction of Cardiac Motion in Patients with Severe Arrhythmia* at the ISMRM 2014 Annual Meeting in Milan, Italy and has been submitted to Magnetic Resonance in Medicine journal and is under revision as: Contijoch F, Han Y, Berisha S, Pilla JJ, Gorman JH III, Gorman RC, Witschey W. *Retrospective cine MRI reconstruction of multiple beat morphologies in the presence of arrhythmias*.

Chapter 6 has been submitted for publication IEEE Transaction on Medical Imaging and is currently under revision as: Contijoch F, Han Y, Hansen MS, Kellman P, Gualtieri E, Elliott M, Berisha S, Pilla JJ, Gorman JH III, Gorman RC, Witschey W. *Continuous Adaptive Radial Sampling of K-Space from Real-Time Physiologic Feedback in MRI.*

Chapter 7 has been published as: Witschey WR, Contijoch F, McGarvey JR, Ferrari VA, Hansen MS, Lee ME, Takebayashi S, Aoki C, Chirinos JA, Yushkevich PA, Gorman JH III, Pilla JJ, Gorman RC. *A Real-Time Magnetic Resonance Imaging Technique for Determining Left Ventricle Pressure-Volume Loops.* Ann Thorac Surg. 2014 May;97(5):1597-603. PMID: 24629301

Chapter 8 has been submitted to the American Journal of Physiology: Heart and Circulatory Physiology and is under review as Contijoch FJ, Witschey WRT, McGarvey J, Lee MA, Gorman JH III, Gorman RC, Pilla JJ. *Slice-by-slice PV loop analysis demonstrates native differences in regional cardiac contractility and response to inotropic agents.*

Chapter 9 has been presented at the annual meetings of the SCMR and ISMRM in 2014. Specifically, the use of different motion-tracking algorithms was presented at the 2014 Annual Meeting of the SCMR as Contijoch F, Rogers K, Avants B, Yushkevich P, Hoshmand V, Gorman RC, et al. *Quantification of left ventricular deformation fields from undersampled radial, real-time cardiac MRI*. J Cardiovasc Magn Reson; 2014;16(Suppl 1):P366. The use of motion-tracking to measure regional function was presented at the 2014 Annual Meeting of ISMRM as Contijoch F, Witschey WR, McGarvey JR, Lee MA, Kondo N, Shimaoka T, Aoki C, Takebayashi S, Zsido GA, Dillard C, Gorman JH III, Gorman RC, Pilla. *Regional Frank-Starling relations in infarcted swine via dynamic real-time MRI.* ISMRM 2014 Annual Meeting. Milan, Italy, May 10-16 2014

Chapter 10 has been submitted to the Journal of the American College of Cardiology and is under review as Contijoch FJ, Rogers K, Rears H, Kellman P, Gorman JH III, Gorman RC, Yushkevich P, Zado ES, Supple GE, Marchlinski FE, Witschey WRT, Han Y. *Quantification of LV function pre, during, and post premature ventricular complexes reveals variable hemodynamics.*

Chapter 1: Dissertation Overview

1.1: Clinical Relevance and Motivation

Over the past 15 years, there has been a significant decrease in mortality associated with acute myocardial infarction (decrease of 10.7% per year for men and 5.1% per year for women) (1). However, after surviving a myocardial infarction (MI), an adverse remodeling process may occur wherein the infarcted region expands or stretches as the infarcted tissue is replaced with scar tissue and results in a global dilation of the left ventricle (LV). This adverse remodeling process and infarct expansion in the LV is correlated with a poor long-term prognosis (2–4).

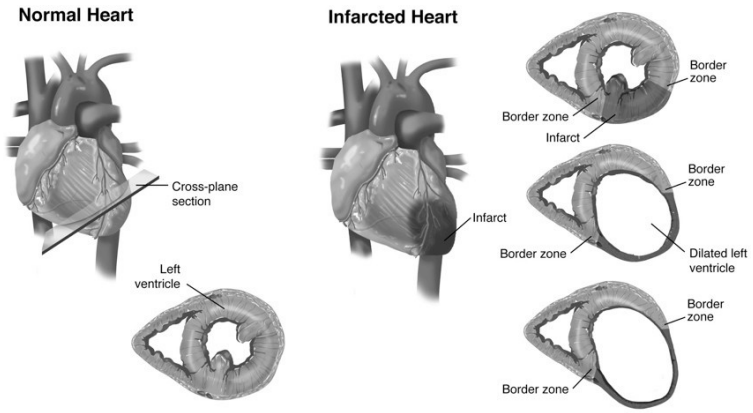

Figure 1.1: Diagram of LV remodeling after infarction. Adapted from (5).

As a result, although mortality from acute MI has decreased, the prevalence of heart failure has increased, and by 2030, is expected to increase 25% from 2013 levels (5,6). In addition, current treatments for heart failure have made little clinical impact as

evidenced by the lack of improvement in the risk-adjusted 1-year mortality of heart failure between 1999 (31.7%) and 2008 (29.6%) (1,7).

1.2: Current Technological Limitation

Previous studies have demonstrated that the expansion of the infarct is associated with stretching and decreased function of the borderzone myocardium, a region neighboring the infarct that is normally perfused (8–13).

Several novel pharmacologic, stem cell, and mechanical therapies such as the acorn support device, hydrogel therapy, or optimized local infarct restraint (shown below) have shown promise in limiting adverse remodeling in animal studies (14–17). However, subsequent patient trials for some of techniques have shown very limited success (17).

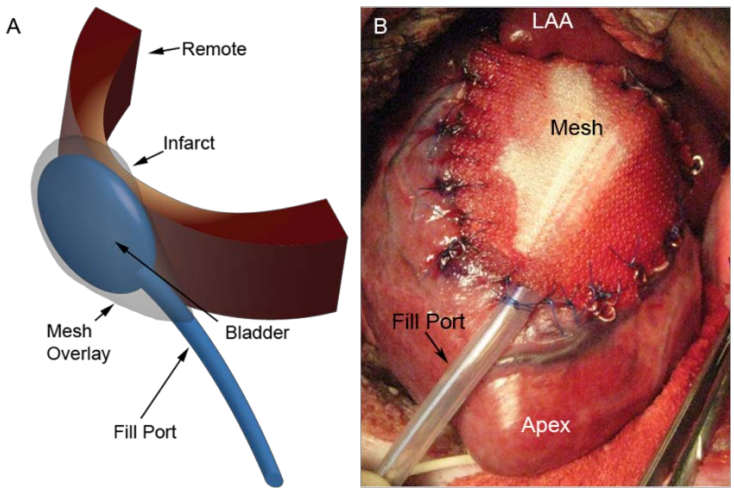

Figure 1.2: Local Infarct Restraint Device. Adapted from (16).

The design and implementation of these techniques has typically been guided by measuring global ventricular remodeling. A method to assess how these interventions

impact the regional function and material properties of the borderzone would allow for more robust design and development. Advanced measures of cardiac function have been previously described (18–21), but their routine use in animal or human studies has been limited by surgically invasive methodology, limited spatial resolution, and assumptions regarding cardiac function.

1.3: Research Objectives

The ultimate goal of the research presented in this dissertation is to develop a framework to acquire measures of cardiac function, which can provide regional information regarding tissue function and material properties. This goal addresses a critical barrier in the development of advanced surgical interventions aimed at limiting adverse LV remodeling. In addition to providing estimates of cardiac function in different regions of the heart (including the borderzone), the framework may allow for improvement in modeling-based approaches by providing additional information for patient-specific computation models.

This dissertation includes several steps towards this long-term vision. Namely:

- Validation of a real-time MRI method for accurate estimation of LV slice volume.
- Development of advanced MRI acquisition techniques for higher spatiotemporal resolution imaging and possible multi-slice imaging.
- Use of the real-time MRI technique for minimally-invasive measurement of global load-independent measures of function.

- Application of the real-time MRI method for slice-by-slice assessment of cardiac function as well as borderzone function via wall thickness measurement.
- Extension of the imaging approaches to clinical patients with frequent ectopic contractions to evaluate the different hemodynamic function associated with premature ventricular contractions.

1.4: Dissertation Overview

This dissertation is organized as follows. Chapter 2 begins with a description of conventional measures of cardiac function and the limitations due to the load-dependence. The chapter continues with an introduction to the framework of both global and regional load-independent measures of function and the challenges in acquisition of these values in animals and humans.

Chapter 3 is a brief description of magnetic resonance imaging (MRI), focusing on challenges faced when imaging the heart. The chapter also outlines three techniques previously developed towards real-time MRI that are utilized in this work.

In Chapter 4, a semi-automated method for quantification of slice volume is presented and applied towards validating a real-time 2D MRI sequence. The 2D real-time MRI sequence is the imaging method used to acquire load-independent measures of function in this thesis.

Chapter 5 and Chapter 6 outline methods for higher spatiotemporal resolution imaging, including an ECG-free approach that allows for different beat morphologies to be

reconstructed as well as an approach that may allow for 3D imaging during dynamic studies.

Chapter 7 describes the use of 2D real-time MRI as a way to observe dynamic changes in cardiac function and estimate global load-independent measures of function. In Chapter 8, differences in cardiac function between the apex, mid-ventricle, and base observed using the real-time MRI technique in native sheep prior to myocardial infarction are described. The results demonstrated the potential of the technique to provide advanced measures of regional function.

In Chapter 9, an even more regional approach is presented. First, motion-tracking algorithms were evaluated and then regional wall thickness was measured throughout a dynamic study in swine, providing measures of regional function within a slice. Initial observations of borderzone function in post-infarct swine are shown.

Chapter 10 shifts gears towards a more clinical application and presents the use of the 2D real-time MRI technique for patients with irregular heart rhythms and ectopic contractions. By synchronizing the imaging technique with ECG recordings, different beat patterns can be observed and global volume measurements can be obtained. The results indicate that different arrhythmic patterns result in varying degrees of impairment in overall hemodynamic function.

Chapter 2: Measures of Cardiac Function

2.1: Conventional Measures of Cardiac Function

Measurement of potential cardiac dysfunction can be broadly obtained via two different schemes: 1) anatomic and functional measurements or 2) tissue characterization.

Anatomic and functional measurements can be obtained using several techniques, including non-invasive imaging (e.g. echocardiography) or more invasive approaches such as catheterization. Clinically, imaging-based techniques allow for non-invasive visualization of the heart and measurement of anatomical dimensions. For example, the extent of dilation of the left ventricle can be quantified by measuring the change in end-diastolic volume. Furthermore, the stroke volume (difference between end-diastolic and end-systolic volume) and ejection fraction (stroke volume divided by end-diastolic volume) provide measures of contractile function and efficiency. Hypokinetic regions (due to infarction) can be visualized from image sequences spanning the cardiac cycle, and measurement of wall thickness can provide information regarding a scarring process, dilated cardiomyopathy, or hypertrophic cardiomyopathy.

Tissue characterization aims to measure dysfunction by identifying different tissue types based on changes in the tissue content and structure. For example, post-mortem histological staining (shown below) is able to clearly identify regions affected by a myocardial infarction and MRI-based techniques have been developed to allow for *in vivo* quantification (22).

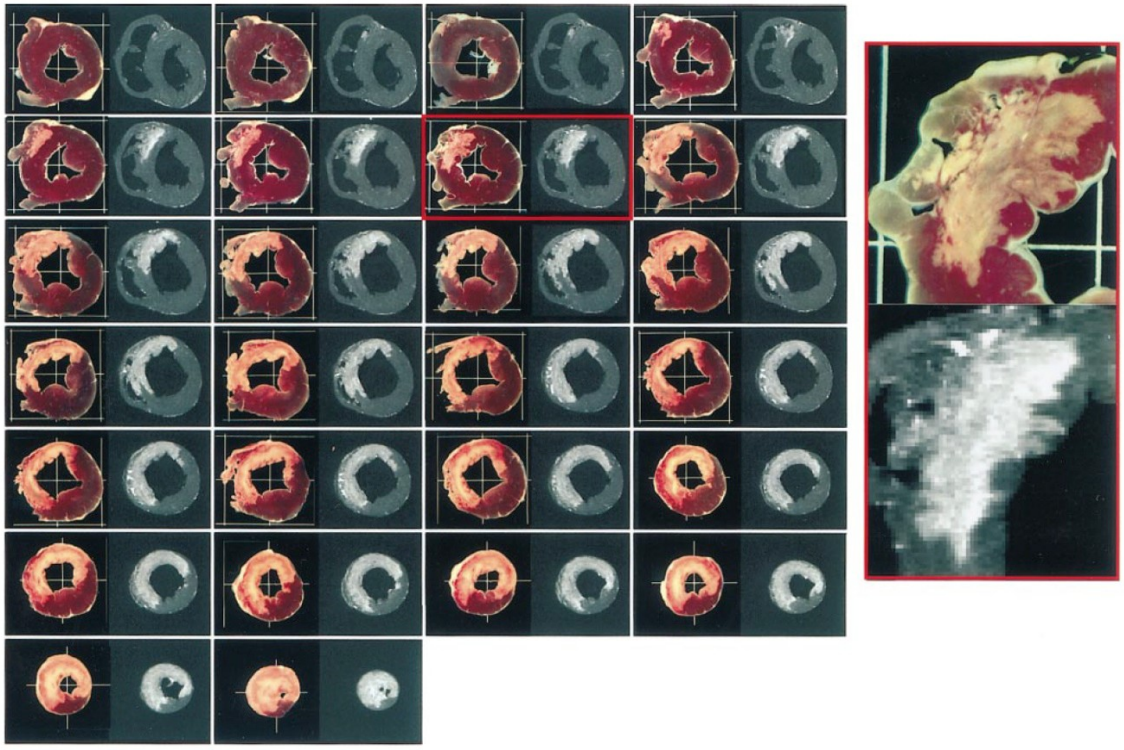

Figure 2.1: Histological and MRI-based characterization of infarcted tissue. Adapted from (22).

2.2: Borderzone Function

As mentioned previously, adverse expansion of the LV has been associated with stretching and decreased contractile function in the borderzone myocardium (myocardial tissue normally perfused despite the myocardial infarction but localized around the infarct) (14).

However, conventional methods for evaluating cardiac function are limited in their ability to quantify the borderzone function and material properties. The sensitivity of tissue characterization MRI methods to molecular changes in the borderzone myocardium is unclear. Furthermore, as will be elaborated in the following section, anatomic and

functional measures are impacted by the complex interaction between apparent cardiac function and the loading conditions of the heart, which may vary during the ventricular remodeling process and confound observed changes in function.

2.3: Contractile Mechanism and Apparent Cardiac Function

The observed function of the heart is a combination of the effectiveness of the myocardial contractile mechanism as well as myocardium-independent variables such as the loading conditions under which the heart operates (namely, the preload and afterload).

A cardiomyocyte generates contractile force via a calcium-induced release of calcium from the sarcoplasmic reticulum (SR), which is triggered by a depolarizing action potential.

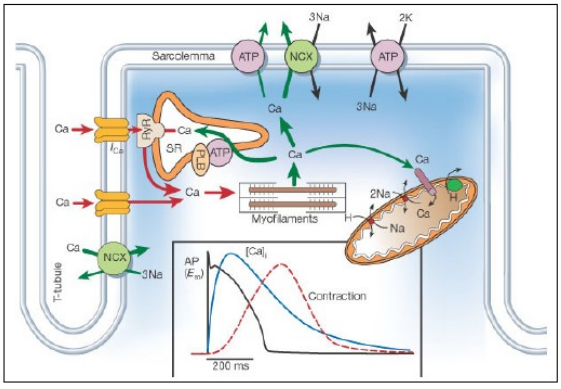

Figure 2.2: Cardiac Excitation-Contraction Coupling. Entry of calcium causes a release of calcium from the sarcoplasmic reticulum. This increase in intracellular calcium triggers the contractile mechanism. Adapted from (23)

The released calcium binds to troponin and causes a conformational change in tropomyosin, exposing a myosin-binding site on the actin filament.

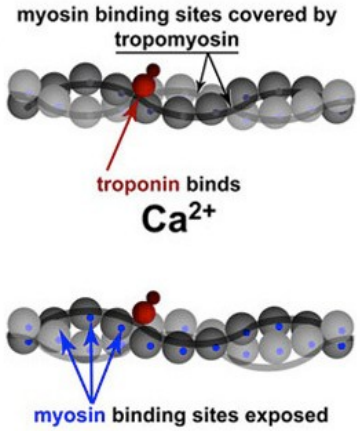

Figure 2.3: Calcium Control of Myosin Binding. After being released from the sarcoplasmic reticulum, intracellular calcium binds to troponin, which exposes myosin binding sites on actin filaments. Adapted from (24)

Once myosin binds to the actin filament, the myosin “pulls” on the actin filament through a conformational change in the head group, which causes a shortening of the myocyte and generates contractile force.

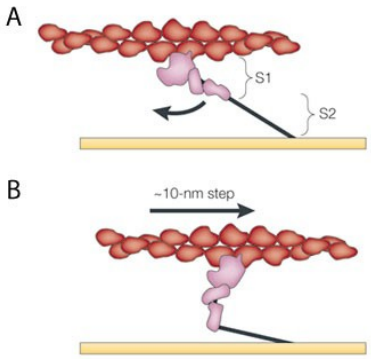

Figure 2.4: Myosin Swinging Cross-Bridge Model. After binding, the conformational change in the myosin head group (S1) causes the myosin to pull on the actin fiber and shorten the myocyte. Adapted from (25)

The strength of this contractile event is regulated by many factors: sympathetic and parasympathetic activity, circulating catecholamines, heart rate, intracellular calcium cycling, affinity of myofilaments to calcium, and the number of myofilaments available for contraction. As a result, isolating changes in function related to ischemia requires controlling for systemic changes in sympathetic activity, parasympathetic activity, circulating catecholamines, or heart rate. Even if these factors are perfectly isolated, another factor - the loading conditions of the heart - will impact the observed cardiac function.

The loading conditions of the heart are typically characterized by two parameters: the preload (the load or blood volume the heart has at the beginning of contraction) and the afterload (the load, often aortic pressure, against which the heart beats).

The impact of the preload on cardiac function is based on the observations of Otto Frank and Ernest Starling. The Frank-Starling Law of the Heart states that increased diastolic filling results in more forceful contraction (leading to increased stroke volume). As the figure below demonstrates, varying the preload of the heart can vary the amount of work performed (measured by stroke volume). One important result of this diagram is that the same heart can produce varying amounts of stroke volume depending on the preload conditions. This organ-level relationship stems from the myocyte-level Force-Length relationship.

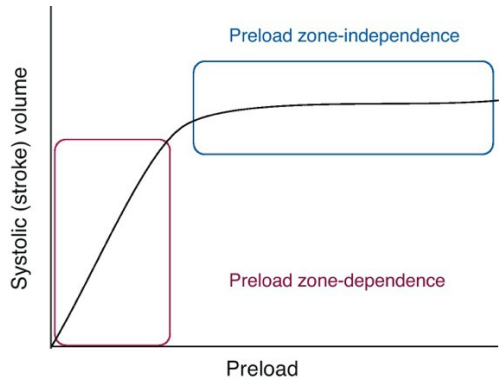

Figure 2.5: Frank-Starling Law of the Heart. Varying the preload of the heart results in variations in stroke volume. The dependence on preload can vary as shown. Adapted from (26)

The load against which the ventricle contracts will also impact the work performed (quantified via the stroke volume). The figure below demonstrates how increased afterload can decrease the stroke volume. The sensitivity of a failing heart to afterload (shown in red) is higher than a normal (black) or moderately failing (green) heart.

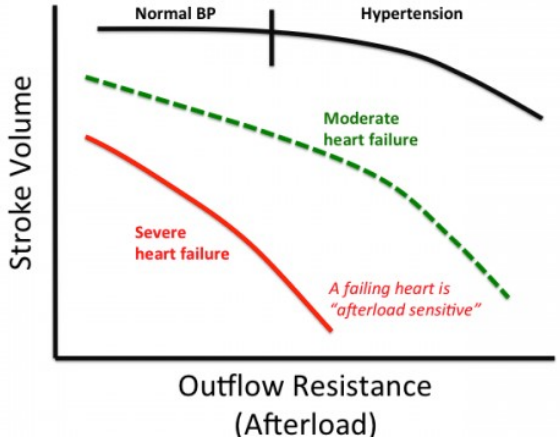

Figure 2.6: Effect of Afterload on Stroke Volume. Increasing the afterload decreases stroke volume. Adapted from (27)

The afterload is often quantified via the aortic pressure since the blood ejected during contraction must overcome the aortic pressure to leave the ventricle.

2.4: Load-Independent Measures of Cardiac Function

To overcome the challenges of quantifying cardiac function in the presence of potentially varying preload and afterload, Hiroyuki Suga developed a framework for evaluation of load-independent cardiac function by modeling the heart as a pump (18–21) where the phases of the cardiac cycle can be plotted on a pressure-volume diagram (shown below). Point A indicates end-diastole, B is the beginning of ejection, C indicates end-systole, and D is the beginning of filling. The cycle of contraction generates a Pressure-Volume loop whose width is the stroke volume and the area is the stroke work (analogous to a piston in a combustion engine).

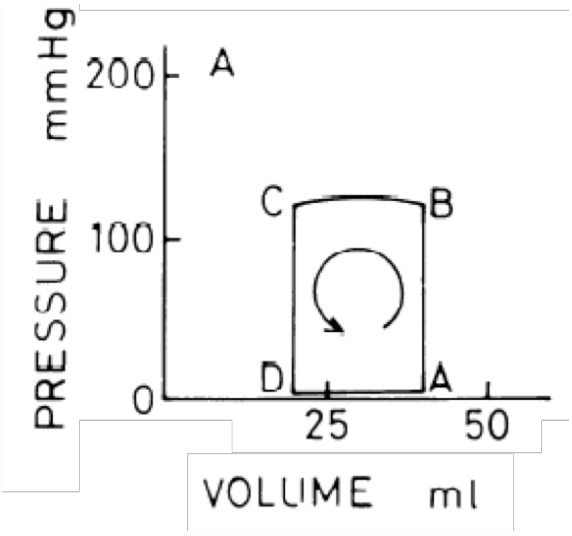

Figure 2.7: Pressure-Volume Diagram of Cardiac Contraction. Adapted from (28)

In this model, the heart is modeled as a globally homogenous material with time-varying material properties. As the diagram below demonstrates, the contractile apparatus

causes the heart to transition from a relaxed (diastolic) state to a stiff (systolic) state. This change in elastance (1/stiffness) can be measured as pressure divided by volume.

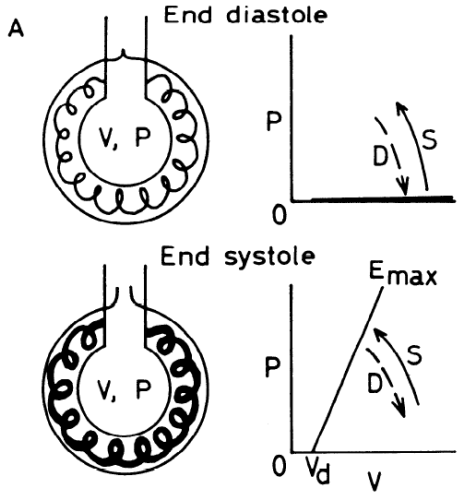

Figure 2.8: Time-Varying Elastance Model of the Heart. Adapted from (28)

In this approach, the maximum and minimum elastance occur at the end-systolic and end-diastolic states, respectively, and have been termed the end-systolic pressure-volume relations (ESPVR) and end-diastolic pressure-volume relations (EDPVR). These two relationships were shown to be independent of loading conditions. This implies that these two parameters provide information regarding the myocardial tissue properties without being confounded by the preload and afterload of the heart.

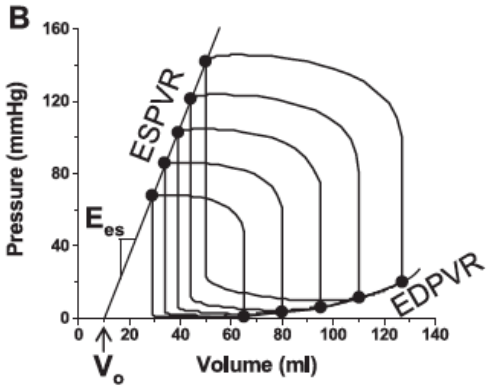

Figure 2.9:Quantification of ESPVR and EDPVR. Adapted from (18)

Experimentally, quantification of ESPVR and EDPVR requires accurate and simultaneous measurement of both ventricular pressure and volume to estimate pressure-volume (PV) loops. Furthermore, ESPVR and EDPVR cannot be estimated from a single PV loop. Therefore, to vary the loading conditions, acute preload reductions can be performed through inflation of a balloon catheter placed in the IVC and/or SVC which causes rapid reduction in the ventricular pressure and volume resulting in a series of PV loops as shown above (29–32).

One limitation of the PV technique is that the global nature of the ESPVR and EDPVR limits the technique's ability to detect changes in the setting of regional myocardial infarction. As a result, although temporal changes in ESPVR and EDPVR in an infarcted heart have been described (33), the changes vary as a function of infarct location, size, and transmurality, which all may be unknown.

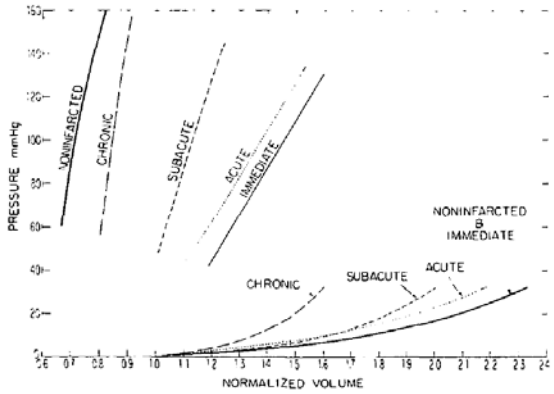

Figure 2.10: Changes in ESPVR and EDPVR with Myocardial Infarction. The temporal changes in ESPVR and EDPVR after infarction are shown for one type of infarct in one location with a predetermine size. Adapted from (33)

2.5: Regional, Load-Independent Measures of Cardiac Function

To address this limitation, Suga et al. also outlined a regional approach to quantify myocardial function. Instead of considering the whole ventricle as a material with time-varying elastance, each myocyte can be thought of as a spring with a time-varying spring constant. This converts Pressure-Volume measurements to Stress-Strain relationships.

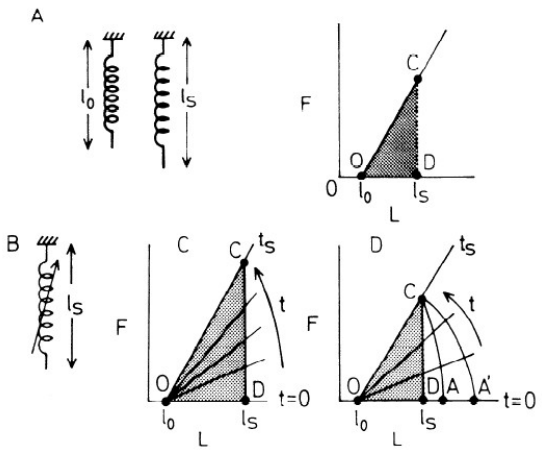

Figure 2.11: Regional Time-Varying Model for Cardiomyocyte. Adapted from (28)

According to Hooke's law, the force (F) of a spring increases linearly with its distance (l_0 to l_S), shown in Figure 2.11. In a time-varying spring (panel B), the initial stretching (OD) generates a small Force due to the low spring constant. However, as the spring constant increases, the force increases (DC). This transition in the spring constant is analogous to the contraction mechanism in a cardiomyocyte.

This regional approach has been implemented using invasive strain gauges affixed to the epicardium as well as sonomicrometry crystals which can be placed at several points on and inside the heart to obtain distance measurements (34–36).

To reduce the complexity of the measurement of stress-strain loops, pressure-length loops (shown below) were proposed as a surrogate measure to simplify the experimental design. The loop area of the pressure-length loops was highly correlated with the global work performed by the heart.

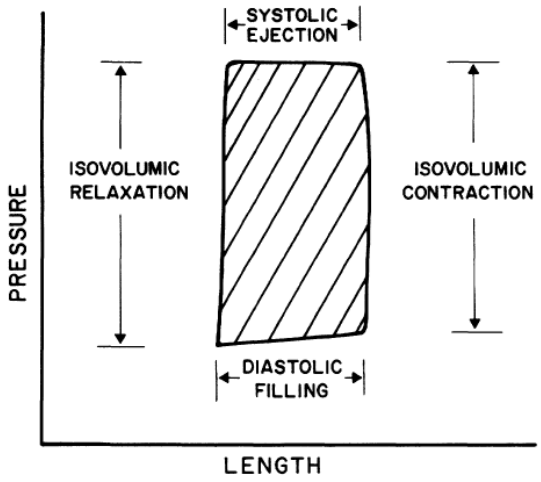

Figure 2.12: Proposed Use of Pressure-Length relationship to quantify segmental work. Adapted from (34)

Furthermore, this approach allowed for changes in myocardial tissue function during ischemia to be observed. As the figure below illustrates, prior to ischemia (circles), manipulation of the loading conditions of the heart resulted in substantial changes in the Loop Area. Ischemia (triangles) resulted in a decrease in the measured Loop Area. Subsequent variation of loading conditions showed a loss of contractile properties of the tissue.

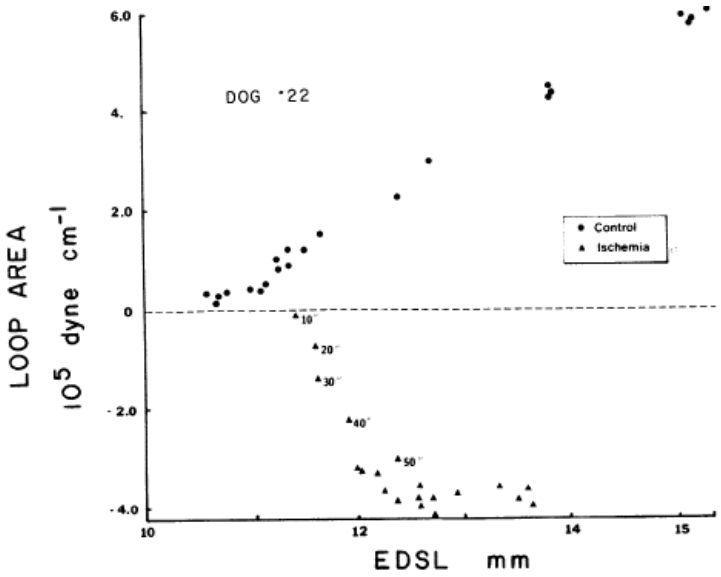

Figure 2.13: Time Course of Ischemic Alterations in Loop Area. Adapted from (34)

In order to obtain these strain or wall thickness measurements, animal subjects underwent an invasive procedure to have strain gauges surgically placed on the epicardium or Sonomicrometry crystal pairs placed at key locations throughout the heart. The invasive nature of the approach substantially limited the potential scope of the studies performed. Furthermore, the placement of individual gauges or Sonomicrometry crystal pairs limited the spatial resolution to surgically-accessible regions. Imaging-based approaches hold the potential to eliminate both of these limitations. Strain imaging via tagged-MRI and DENSE has been used towards this purpose. However, the image acquisition times (described in Chapter 3), limited the ability to perform the desired variations in loading conditions to replicate these experiments. As a result, current strain imaging approaches only acquired a single physiologic state (resulting in a single Pressure-Length loop and a single point along the Frank-Starling curve).

The goal of this thesis is to obtain the previously described load-independent measures of function such as ESPVR (globally) and Loop Area relations (regionally) using an imaging-based approach. This would eliminate the limitations currently faced by these invasive measures and allow for routine acquisition with high spatial resolution. As a result, advanced analysis of borderzone function and material properties could be performed.

Chapter 3: Magnetic Resonance Imaging

3.1: Introduction

As mentioned previously, imaging is often used to quantify global and regional cardiac function because it is non-invasive and has high spatial and temporal resolution, allowing for each phase of the cardiac cycle to be observed at many points along the heart in a single image set.

However, image acquisition techniques, to date, have been too slow to measure load-independent parameters. Specifically, the acquisition times are too long given the brief manipulation of the heart necessary to get multiple Pressure-Volume or Pressure-Length loops before neurohormonal changes affect the cardiac function.

In this chapter, we provide an overview of MRI signal generation and image acquisition and describe recent technical developments, which may open the door for real-time MRI imaging. Such a technique, if accurate, would allow for advanced measurement of cardiac function.

3.2: Overview of Magnetic Resonance Imaging

The nucleus of an atom has an intrinsic magnetic momentum and angular momentum, termed magnetic nuclear spin. Nuclei with non-zero spin will align or polarize in the direction of an applied magnetic field and precess around the direction of the applied magnetic field. In Magnetic Resonance Imaging (MRI), the main magnetic field of the

scanner, termed B_0, is used to generate this net magnetization M, which precesses at the frequency ω which is related to the magnetic field by the Larmor Equation

$$\omega = \gamma B_0 \qquad \text{[Equation 3-1]}$$

The Larmor frequency ω is linearly proportional to the magnetic field, and γ is the gyromagnetic ratio. In the figure below, B_0 is in the z direction.

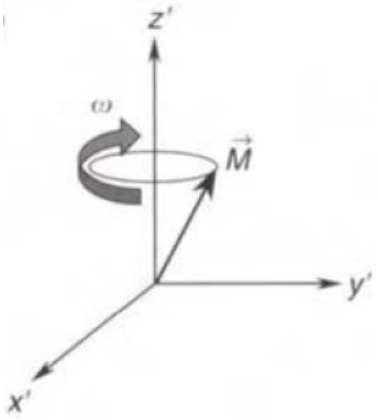

Figure 3.1: Depiction of Net Magnetization M and Precession of Nuclear Spin. Adapted from (51)

Once the nuclei (typically hydrogen nuclei from water molecules) in a tissue have aligned with the main field B_0, perturbations to this polarization are necessary to generate an imaging signal. These perturbations are achieved through a combination of radiofrequency pulses and magnetic field gradients. After excitation, two additional steps are required to convert the signal into a useful image: k-space sampling and image reconstruction.

3.2.1: Signal Generation

MRI signal is generated by recording the electromagnetic field produced by nuclear spins as they revert to the original magnetization. In addition to generating a signal based on the number of spins in a piece of tissue (proton density imaging), differences in the time taken by spins to reorient themselves with the main magnetic field can be exploited for additional image information. The reorientation process is typically quantified via two relaxation processes termed longitudinal relaxation (T_1) and transverse relaxation (T_2). Depending on the imaging application, different combinations of RF pulses and gradients can be utilized to exploit differences in tissue properties.

One imaging sequence that has become integral to clinical cardiac imaging is the balanced Steady-State Free Precession acquisition (37–39). In this technique, RF pulses are repeatedly applied, driving the magnetic spins into a driven-steady state. In this framework, tissue contrast is based on differences in the T_2 / T_1 ratio. This is particularly useful for cardiac imaging as the difference in intensity between blood (bright) and myocardium (intermediate) is high. Furthermore, fat and air result in high and low signal intensities, respectively, which further help produce clinically pertinent images. This can be observed in the figure below which shows the change in cardiac shape between end-diastole (left) and end-systole (right) in the short-axis of a sheep.

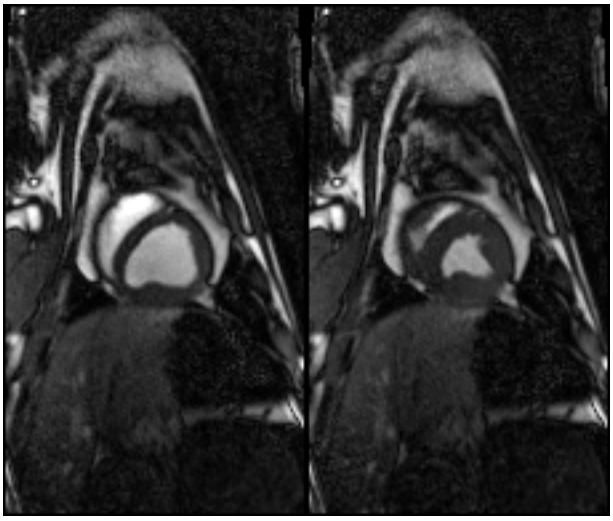

Figure 3.2: Tissue Contrast and Changes in Anatomy with Cardiac Contraction Observed via bSSFP Imaging in a Sheep

3.2.2: K-Space Sampling

The MRI signal s, acquired in a Fourier encoding scheme, can be described by the signal equation

$$s(\vec{k}_i) = \int_{\Re^2} m(\vec{r}) e^{-i2\pi \vec{k}_i \cdot \vec{r}} \, d\vec{r} + \varepsilon_i \qquad [3\text{-}2]$$

where $s(\vec{k}_i)$ is the observed signal at the location in k-space $\vec{k}_i$. This signal is a result of the discrete sampling of the object m at locations $\vec{r}$ in space $\Re^2$, the Fourier encoding of the imaging process $e^{-i2\pi \vec{k}_i \cdot \vec{r}}$, and some noise ε_i.

As a result, instead of acquiring data corresponding to physical portions of the object, an MRI signal s quantifies the amount of a particular spatial frequency k_i in the object.

Therefore, the manner in which the k-space is sampled will impact the reconstructed image. In conventional MRI, a Cartesian grid of k-space samples k_i is acquired in the two-dimensional $k_x - k_y$ plane. The extent of the Fourier sample acquired ($k_x^{\max}$ and $k_y^{\max}$) determines the spatial resolution while the spacing between the samples Δk_x and Δk_y defines the field-of-view (FOV) of the acquisition. The relationship between these values and the corresponding image are shown in the figure below.

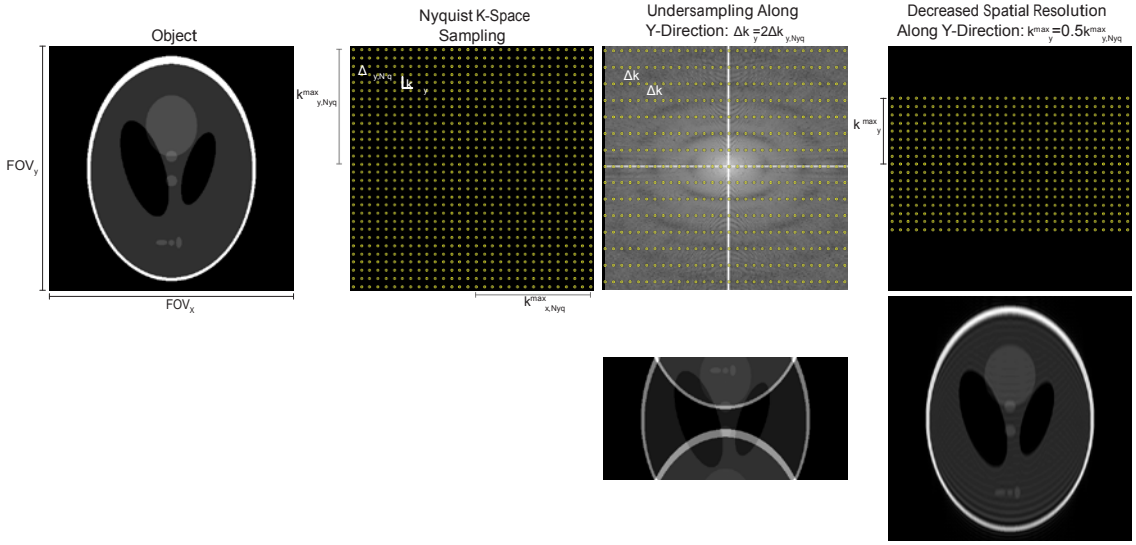

Figure 3.3: Relationship between Extent and Density of K-Space Sampling and Reconstructed Image. The extent and density of sampling necessary for an object within a certain FOV can be determined via the Nyquist Sampling Criteria. If the number of samples is decreased by decreasing the sampling density, aliasing occurs in the direction of undersampling. If the extent of sampling is decreased, a loss of spatial resolution (blurring) occurs in the direction of decreased sampling.

3.2.3: Image Reconstruction

As described in the section above, MRI data $s(k_i)$ is acquired in k-space. Therefore, generating an image requires taking the inverse Fourier transform of the acquired data.

For a conventional Cartesian acquisition, data is acquired on a rectilinear grid, which allows for straightforward use of two-dimensional Fourier transforms. A more detailed explanation of the image reconstruction problem is described in 3.4.1.

3.3: MRI of the Heart

The description of the MRI data acquisition has thus far assumed a stationary object. As the heart is constantly in motion, some motion occurs during the acquisition of MRI data. To obtain images without blurring key anatomical features, an acquisition must 'freeze' the motion of the heart. This is analogous to the need for a high shutter speed (left) on a camera to effectively capture a moving object (such as traffic shown below).

Figure 3.4: Example of high shutter speed necessary to image moving objects. Adapted from (40)

Generally, to eliminate blurring due to motion, there are three possible approaches, all of which are used in clinical cardiac MRI. First, the shutter speed could be increased. One example of this approach is the use of cardiac gating, which exploits the repetitive nature of the cardiac cycle to improve the effective shutter speed of the acquisition (41–43). In a

gated acquisition, data acquired during different heartbeats is synthesized into a single dataset. This reduces the amount of time over which data is acquired in a particular beat, increasing the shutter speed of the acquisition, but makes the scan sensitive to any variation in cardiac position between the multiple heartbeats sampled. A second approach (discussed in Chapter 3.4) is to decrease the amount of sampling necessary. The final option is to decrease, or slow down, the motion of the object. If a single cardiac phase is sufficient for the desired imaging task, imaging can be performed during end-diastole, a typically quiescent phase in which there is low cardiac motion.

To visually observe each phase of cardiac motion and quantify elements such as the change in blood volume, a sequence of images, each of which 'freezes' cardiac motion, is necessary. The Wiggers diagram below demonstrates the changes in ventricular pressure and volume associated with the different phases of the cardiac cycle. The duration of the shortest phases (isovolumic contraction and relaxation) range between 35-40 ms to 70-80 ms, respectively.

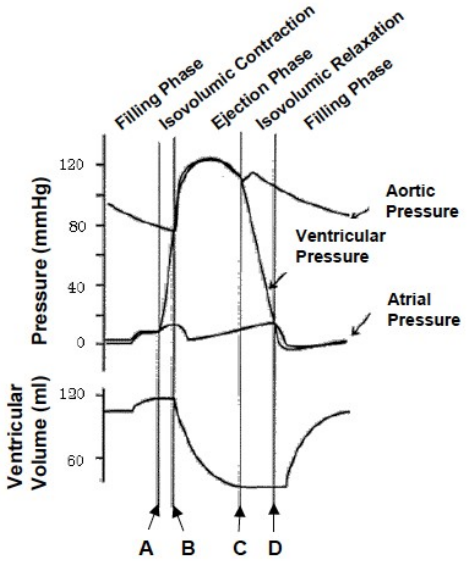

Figure 3.5: Wiggers Diagram Depicting Ventricular Pressure and Volume Changes During the Cardiac Cycle. Adapted from (44).

The effective shutter speed of the MRI acquisition is determined by several scan parameters (e.g. repetition times and spatial resolution) as well as physiologic limits (maximum gradient strength). As a result, the bSSFP scan mentioned previously is typically acquired with a repetition time (TR) of approximately 3 ms, and Nyquist sampling requires approximately 128 repetitions to fill a 128x128 grid of k-space data. With these parameters, the image exposure time would be 384 ms. When compared with the duration of isovolumic contraction, this would cause substantial blurring as the duration of the scan is more than 10 times too slow to freeze the cardiac phase of interest. Furthermore, acquiring an image every 384 ms would result in a frame rate of < 3 fps, which would not allow for all of the cardiac phases to be captured in an image sequence.

The clinical solution to this limitation is the use of ECG-gating, which allows for images with short exposure times (< 50 ms) and high frame rates (> 20 fps) to be obtained. In a gated acquisition, a portion of k-space is repeatedly acquired across the cardiac cycle.

As the figure below demonstrates, when a new beat is detected via the ECG, a different portion of k-space is sampled (phase encoding step PES transitions) such that after several beats, the entire k-space is acquired throughout the cardiac cycle.

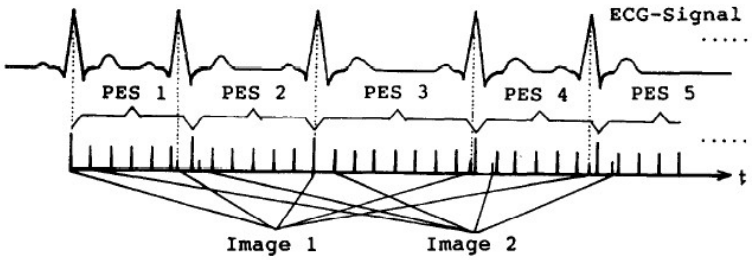

Figure 3.6: Retrospective Gating Diagram Depicting Incremental Phase Encoding Steps. Adapted from (41).

Any discrepancy in the motion between the beats synthesized will result in incorrect data synthesis and poor image quality. Potential sources of variation include patient motion, respiratory motion, ectopic contractions, changes in loading conditions, and changes in inotropic state. As a result, cardiac MRI is typically performed as the subject holds their breath. The scan must also reject and reacquire data acquired during ectopy. For clinical spatiotemporal resolution, k-space data obtained during 8 – 12 distinct heartbeats are combined. As a result, the variations in loading conditions outlined in Chapter 2.4, which result large changes in cardiac position and motion within 3-5 heartbeats, are too rapid to be observed via this imaging approach.

3.4: Developments Towards Real-Time MRI

Iterative reconstruction, multi-detector acquisition (parallel imaging), and non-Cartesian k-space sampling have been used to decrease the amount of MRI data required for reconstruction of an image. These methods allow for shorter data acquisitions while preserving the spatiotemporal resolution, and, to varying degrees, the image quality. The methods are summarized in the sections below.

3.4.1: Image Reconstruction: An Inverse Problem

In a Fourier-encoded MRI experiment, the inverse Fourier transform is an easy and efficient method to generate an MRI image and is readily implemented in a variety of software packages. However, as will be shown below, this approach is a shortcut, which can be performed only under certain conditions, specifically Cartesian sampling satisfying the Nyquist Sampling Criteria. More generally, the imaging process can be modeled as linear system where an M x N imaging matrix A transforms an object m (N pixels) into an acquired MRI signal s (M samples) in the presence of noise ε .

$$s = Am + \varepsilon \qquad [3\text{-}3]$$

In the case of Fourier sampling, each element $a_{i,j}$ of the M x N imaging matrix A can be described by

$$a_{i,j} = \int p_j(\vec{r}) e^{-i2\pi \vec{k}_i \cdot \vec{r}} d\vec{r} \quad \textbf{and} \quad p_j(\vec{r}) = \delta(\vec{r} - \vec{r}_j) \qquad [3\text{-}4]$$

where $p_j(\vec{r})$ describes the discrete sampling of the continuous object m in space r using the delta function and $e^{-i2\pi k_i \cdot \vec{r}}$ corresponds to the Fourier encoding of the MRI acquisition.

In expanded matrix notation, this becomes

$$\begin{bmatrix} s_1 \\ \vdots \\ s_M \end{bmatrix} = \begin{bmatrix} \int p_1(r) e^{-2\pi k_1 \cdot r}\, dr & \cdots & \int p_N(r) e^{-2\pi k_1 \cdot r}\, dr \\ \vdots & \ddots & \vdots \\ \int p_1(r) e^{-2\pi k_M \cdot r}\, dr & \cdots & \int p_N(r) e^{-2\pi k_M \cdot r}\, dr \end{bmatrix} \begin{bmatrix} m_1 \\ \vdots \\ m_N \end{bmatrix} + \begin{bmatrix} \varepsilon_1 \\ \vdots \\ \varepsilon_N \end{bmatrix}$$

Mx1 **MxN** **Nx1** **Mx1** [3-5]

The use of the delta function allows for $p_j(\vec{r})$ to be substituted

$$\begin{bmatrix} s_1 \\ \vdots \\ s_M \end{bmatrix} = \begin{bmatrix} \int \delta(r - r_1) e^{-2\pi v_1 \cdot r}\, dr & \cdots & \int \delta(r - r_N) e^{-2\pi v_1 \cdot r}\, dr \\ \vdots & \ddots & \vdots \\ \int \delta(r - r_1) e^{-2\pi v_M \cdot r}\, dr & \cdots & \int \delta(r - r_N) e^{-2\pi v_M \cdot r}\, dr \end{bmatrix} \begin{bmatrix} m_1 \\ \vdots \\ m_N \end{bmatrix} + \begin{bmatrix} \varepsilon_1 \\ \vdots \\ \varepsilon_N \end{bmatrix} \quad [3\text{-}6]$$

This allows for the Fourier Shift Theorem to be used, simplifying the imaging operator.

$$\begin{bmatrix} s_1 \\ \vdots \\ s_M \end{bmatrix} = \begin{bmatrix} e^{-2\pi v_1 \cdot r_1} \mathbf{F}[\delta(r)]\big|_{v_1} & \cdots & e^{-2\pi v_1 \cdot r_N} \mathbf{F}[\delta(r)]\big|_{v_1} \\ \vdots & \ddots & \vdots \\ e^{-2\pi v_M \cdot r_1} \mathbf{F}[\delta(r)]\big|_{v_M} & \cdots & e^{-2\pi v_M \cdot r_N} \mathbf{F}[\delta(r)]\big|_{v_M} \end{bmatrix} \begin{bmatrix} m_1 \\ \vdots \\ m_N \end{bmatrix} + \begin{bmatrix} \varepsilon_1 \\ \vdots \\ \varepsilon_N \end{bmatrix}$$

$$= \begin{bmatrix} e^{-2\pi v_1 \cdot r_1} & \cdots & e^{-2\pi v_1 \cdot r_N} \\ \vdots & \ddots & \vdots \\ e^{-2\pi v_M \cdot r_1} & \cdots & e^{-2\pi v_M \cdot r_N} \end{bmatrix} \begin{bmatrix} m_1 \\ \vdots \\ m_N \end{bmatrix} + \begin{bmatrix} \varepsilon_1 \\ \vdots \\ \varepsilon_N \end{bmatrix} \quad [3\text{-}7]$$

In this framework, image reconstruction equates to solving the inverse problem in the presence of complex Gaussian noise ε . A common approach is to utilize the least-squares estimation method such that the image estimate $\hat{m}$ minimizes the residual error $e = s - Am$.

$$\hat{m} = \underset{\hat{m}}{\arg\min} \left\| s - A\hat{m} \right\|^2 \qquad [3\text{-}8]$$

As shown in Appendix A, this formulation allows for estimation of the image $\hat{m}$ without direction inversion of the imaging matrix *A* via the Moore-Penrose pseudo-inverse

$$\hat{m} = (A!A)^{-1} A!s \qquad [3\text{-}9]$$

where $A!$ is the complex conjugate transpose. Furthermore, in the case of conventional Cartesian sampling, which satisfies the Nyquist Sampling Criteria, the imaging matrix A becomes square and the inverse operation A^{-1} simplifies to

$$A^{-1} = \frac{1}{M} A^* \qquad [3\text{-}10]$$

where A^* denotes the complex conjugate. As a result, estimation of the image $\hat{m}$, shown below, is the two-dimensional inverse Fourier transform $\Im^{-1}$ of the rectilinear data s .

$$\hat{m} = (A!A)^{-1} A!s = A^{-1} s = \frac{1}{M} A^* s = \frac{1}{M} \Im^{-1}[s] \qquad [3\text{-}11]$$

Although the solutions in **Error! Reference source not found.** and [3-11] do not apply during undersampling and/or non-Cartesian trajectories, the general solution outlined in [3-8] and [3-9] can be used to estimate the image $\hat{m}$ via the Moore-Penrose pseudo-inverse.

During undersampling or non-Cartesian trajectories, the imaging matrix A can become ill-conditioned, resulting in undesirable noise amplification. This can be controlled via the use of a regularization term R, which is often calculated from the image m. This addition modifies the minimization problem to be

$$\hat{m} = \arg\min_{\hat{m}} \left\{ \left\| s - A\hat{m} \right\|^2 + \lambda R(m) \right\} \quad [3\text{-}12]$$

where the regularizer $R(m)$ can be selected to penalize a feature of the image and λ controls the tradeoff between data-fidelity and noise. This results in a slight modification of the pseudo-inverse solution shown in **Error! Reference source not found.** above

$$\hat{m} = (A'A + \lambda R)^{-1} A's \quad [3\text{-}13]$$

3.4.2: Iterative Image Reconstruction

The direct inversion in [3-9] or [3-13] above may not be practical (given the size of the image matrix A) or even possible (if R is non-quadratic). As a result, image $\hat{m}$ is often found through an iterative process. In Appendix 2, a simple example, adapted from Shechuk, of an iterative solver is included which describes the general methodology and provides a description of the steps in the iterative process.

Fast and efficient implementations of these iterative algorithms have been developed by several groups (45–47). Several implementations make use of graphics processing units to accelerate the calculations and perform the reconstruction in computational and memory efficient ways. In particular, this dissertation utilized Gadgetron, an open-source implementation from the National Institutes of Health (NIH, Bethesda, MD) (47). In Gadgetron, processing steps are applied in a modular manner, allowing for quick modification of the reconstruction process. An example of a processing pipeline in Gadgetron is shown below.

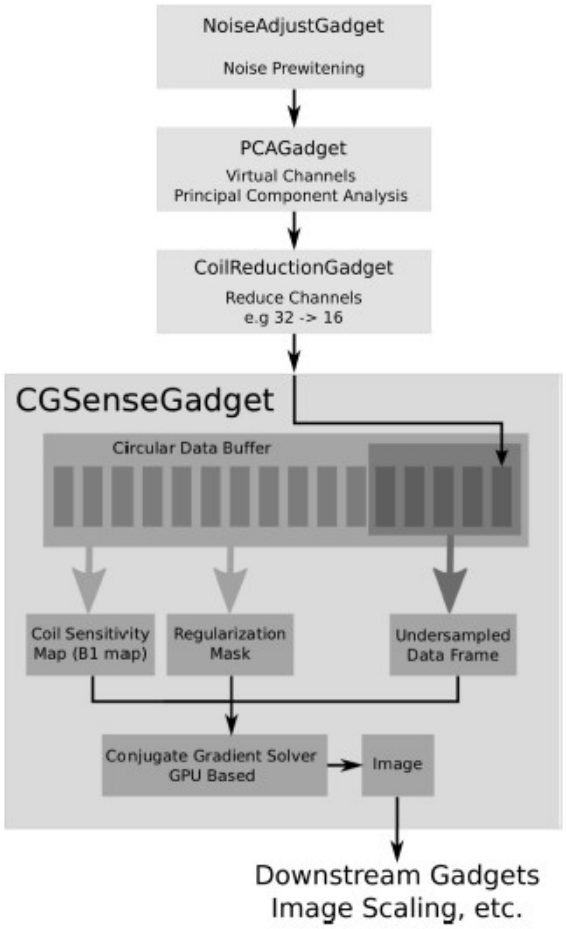

Figure 3.7: Modular Processing Pipeline in Gadgetron. Adapted from (47)

As shown in the figure above, each step in the reconstruction is a step in a pipeline. For example, first noise pre-whitening is performed, followed by a principal component analysis to identify virtual coils, which allows for efficient coil reduction. As a result, customization of an image reconstruction can be performed by modifying individual functions without disturbing the remaining components.

3.4.3: Parallel Imaging

In 1999, Pruessman, et al. outlined an approach, SENSE, to utilize the spatial location of multiple receiver coils to unfold images that are undersampled (48). The approach utilizes estimated coil sensitivity profiles as an additional element of the imaging matrix A . The figure below shows the typical fold-over artifact associated with undersampling along the y-direction. The use of multiple receivers with different spatial coverage allows for the aliased pixel to be resolved.

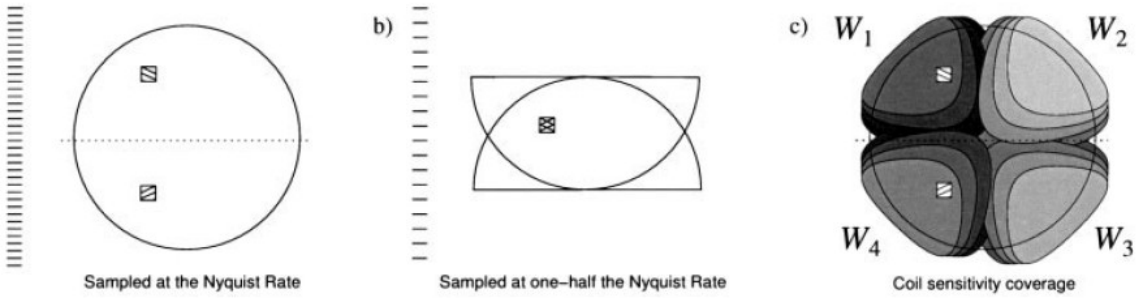

Figure 3.8: Coil Sensitivity Information Helps Resolved Sub-Nyquist Aliasing Artifact. Adapted from (48).

For multiple coils, the vector of acquired data s and imaging matrix A increases along the row direction (from M row to MC rows where C is the number of coils) which improves the conditioning of imaging matrix A , allowing for improved estimation of the object m.

$$\begin{bmatrix} s_{1,1} \\ \vdots \\ s_{M,1} \\ \vdots \\ s_{1,C} \\ \vdots \\ s_{M,C} \end{bmatrix} = \begin{bmatrix} c_1(r_1)e^{-2\pi v_1 \cdot r_1} & \cdots & c_1(r_N)e^{-2\pi v_1 \cdot r_N} \\ \vdots & & \vdots \\ c_1(r_1)e^{-2\pi v_M \cdot r_1} & \cdots & c_1(r_N)e^{-2\pi v_M \cdot r_N} \\ \vdots & & \vdots \\ \vdots & & \vdots \\ \vdots & & \vdots \\ c_C(r_1)e^{-2\pi v_1 \cdot r_1} & \cdots & c_C(r_N)e^{-2\pi v_1 \cdot r_N} \\ \vdots & & \vdots \\ c_C(r_1)e^{-2\pi v_M \cdot r_1} & \cdots & c_C(r_N)e^{-2\pi v_M \cdot r_N} \end{bmatrix} \begin{bmatrix} m_1 \\ \vdots \\ m_N \end{bmatrix} + \begin{bmatrix} \varepsilon_{1,1} \\ \vdots \\ \varepsilon_{M*C} \end{bmatrix} \quad [3\text{-}14]$$

MC x 1 **MC x N** **N x 1** **MC x 1**

For this method to improve the estimation of the image object m, two key elements of the coils sensitivity maps are necessary. First, the coil sensitivities $c(r)$ must be unique such that the row-rank of the imaging matrix A increases. Furthermore, accurate estimates of the coil sensitivity profiles $c_j(r)$ is required for each coil. A variety of approaches have been previously outlined for estimation of the coil sensitivity profiles and their relative benefits are beyond the scope of this dissertation (48–50).

The potential to accelerate cardiac imaging was demonstrated in the original manuscript where the number of heartbeats necessary for acquisition of an image was decreased from 15 to 5 with the corresponding image quality shown below.

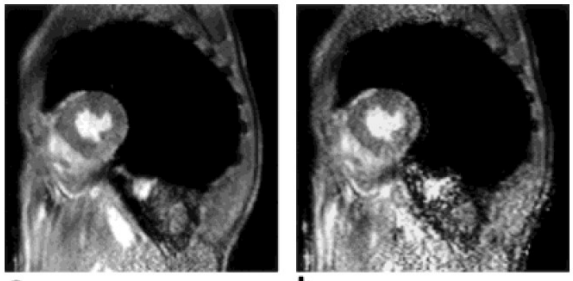

Figure 3.9: Multi-Detector Acquisition Accelerates Cardiac Imaging. a) 15 heartbeats are synthesized for a full image without acceleration. b) SENSE allows for a reduction to 5 heartbeats with comparable image quality. Adapted from (48)

Furthermore, combining this multiple detector approach with an iterative reconstruction allowed for substantial undersampling while preserving image quality and spatiotemporal resolution. The image below shows the fold-over aliasing that occurs with a single receiver coil and the improvement with SENSE at the initial, intermediate, and final stages of the iterative reconstruction.

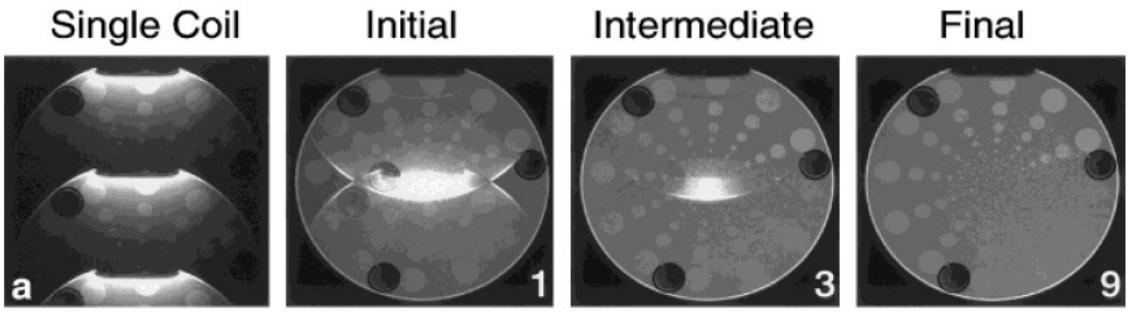

Figure 3.10: Multi-Detector Acquisiton and Iterative Reconstruction Allow for Substantial Sub-Nyquist Sampling. a) A single coil image shows substantial fold-over artifact, which is improved with multi-detector reconstruction (1). Subsequent iterations of the iterative reconstruction algorithm further improve the result. Adapted from (45)

3.4.4: Non-Cartesian k-Space Sampling

The original MRI acquisition experiments were performed using a radial trajectory. While this was driven mainly by hardware limitations, the use of a non-Cartesian trajectory has become, once again, popular due to advantageous undersampling properties.

The Nyquist Sampling Criteria dictates the sampling rate necessary for a discrete-time signal to avoid aliasing when sampling a continuous-time signal. In MR imaging, this criteria informs the spacing of k-space samples necessary to avoid aliasing when reconstructing an image. In conventional Cartesian sampling, the distance between samples is determined based on the bandwidth of the analog-to-digital converter (Δk_x) as well as the number of phase-encoding steps performed (Δk_y). The bandwidth utilized is typically much higher than the number of phase-encoding steps performed. To accelerate the image acquisition, the number of phase encode steps could be reduced as the acquisition time is directly proportional to the number of phase-encode steps. If the number of phase-encoding steps is decreased (and Δk_y is increased), the resulting aliasing in a Cartesian acquisition can be seen below. The aliasing in the middle panel results from $\Delta k_y = 3\Delta k_{y,Nyquist}$ while the right panel results from $\Delta k_y = 4\Delta k_{y,Nyquist}$.

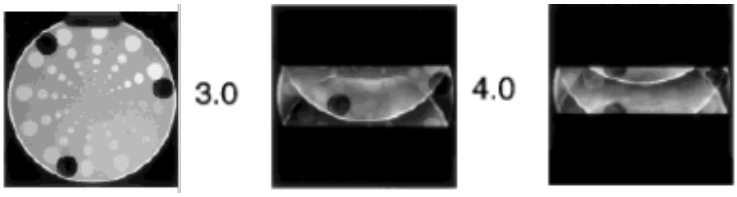

Figure 3.11: Aliasing Artifact from Sub-Nyquist Cartesian Sampling. Adapted from (45)

The amount of aliasing corresponds to the distance between k-space samples. In the Cartesian case shown above, the distance between samples in the k_y direction is uniform, causing a typical 'fold-over' pattern which becomes worse as the subsampling increases (from 3 to 4). For a radial acquisition, the distance between k-space sampled can be quantified using polar coordinates: Δk_r and Δk_θ.

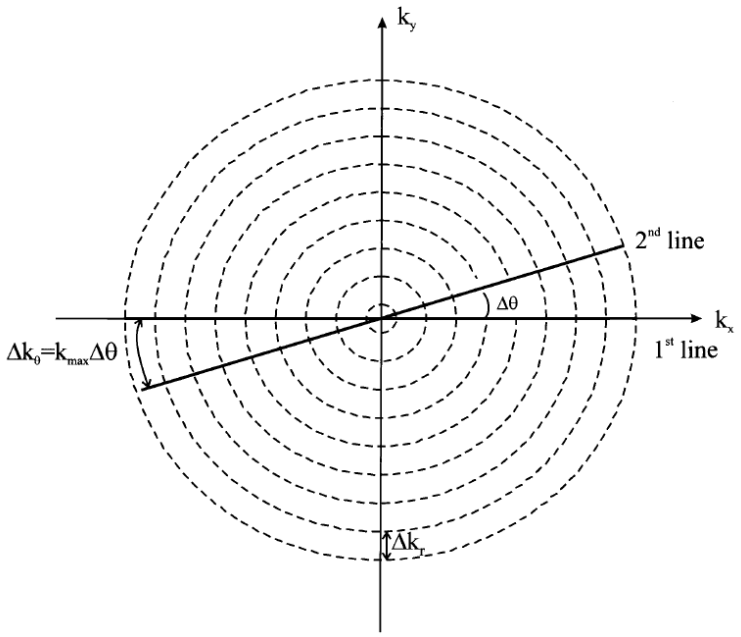

Figure 3.12: K-Space Sampling in a Radial (Projection) Acquisition. Adapted from (51)

As is the case in Cartesian sampling, the bandwidth of the analog-to-digital converter determines Δk_r and does not typically cause aliasing. Δk_θ is determined by the number of radial projections acquired as well as the radius from the center, $k_{\max}$. As a result, more radial projections are necessary to satisfy the Nyquist criteria than the Cartesian acquisition where the number of radial projections N_θ

$$N_\theta = \pi N_R / 2 \qquad [3\text{-}15]$$

where N_R is the number of points sampled along the projection.

Despite this increased requirement, the pattern of aliasing in radial undersampling, shown below, is significantly different than that observed in the Cartesian case. For the image shown, N_R = 256 and therefore N_θ = 402 to satisfy the Nyquist criteria. Despite undersampling by a factor of 6 and 16, the images reconstructed from 64 and 24 radial projections do not have the same 'fold-over' artifact and still demonstrate considerably high image quality despite the obvious gaps in the k-space sampling shown in the lower right panel. The aliasing pattern in radial imaging is typically referred to as 'streaking'.

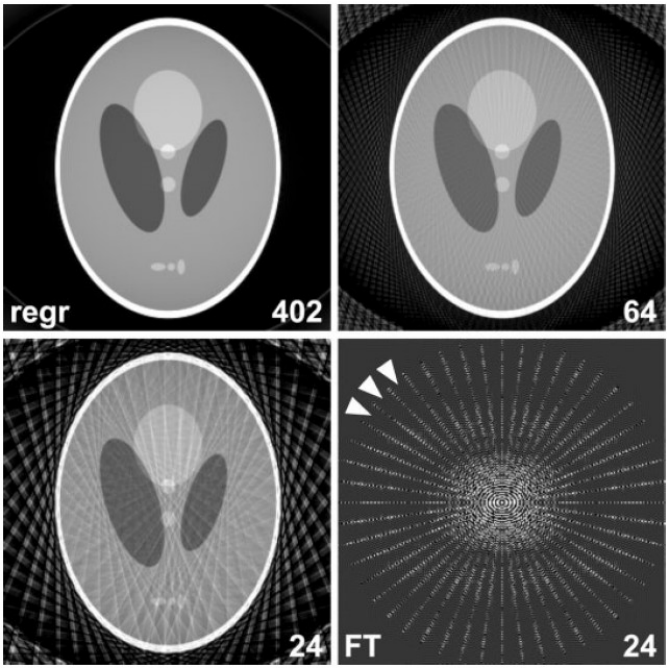

Figure 3.13: Sub-Nyquist Aliasing Pattern in Radial Acquisition. Adapted from (52)

As a result, if radial sampling can be implemented accurately, it holds the potential to provide images with improved spatiotemporal resolution while preserving image quality. Combining this sampling pattern with an iterative reconstruction approach and multiple detector acquisition (shown below) can provide high-quality images with high spatiotemporal resolution.

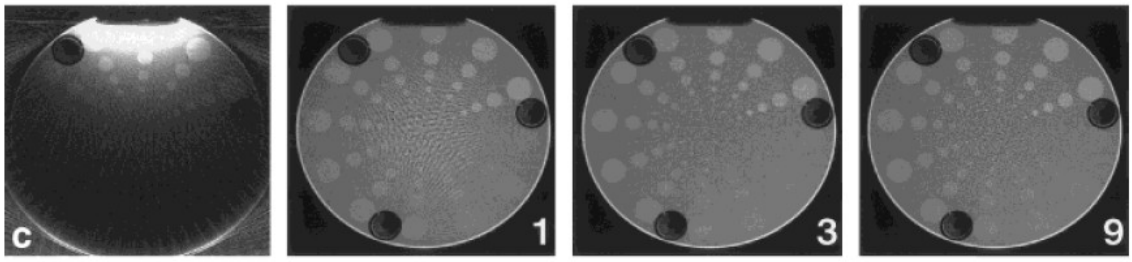

Figure 3.14: Multi-Detector Acquisition with a Radial K-Space Trajectory and Iterative Reconstruction Allows for Substantial Undersampling While Preserving Image Quality. Adapted from (45)

3.5: Potential Real-Time Cardiac MRI

The technical goal of this thesis is to apply these recent developments in real-time MRI towards the goal of performing imaging during dynamic changes in loading conditions and obtain advanced measures of cardiac function. Although the methods to perform real-time cardiac imaging have been published, the accuracy of the different approaches has not been robustly quantified. As a result, the first step (Chapter 4) in this thesis work was to develop a method to quantify the trade-off between spatiotemporal resolution and image quality by measuring slice volume. The approach determined imaging parameters which allowed for accurate measurement of real-time slice volume to be identified.

Chapter 4: User-Initialized Active Contour Segmentation and Golden-Angle Real-Time Cardiac MRI Enables Accurate Assessment of LV Function

4.1: Abstract

Real-time cardiac magnetic resonance (CMR) depicts motion from each cardiac cycle, but there is limited and inconsistent evidence to show that rt-CMR can accurately assess beat-to-beat variation in left ventricular (LV) function or during an arrhythmia.

Multi-slice, short axis cine and real-time golden-angle radial CMR data was collected in 22 clinical patients (18 in sinus rhythm and 4 patients with arrhythmia). A user-initialized active contour segmentation (ACS) software was validated via comparison to manual segmentation on clinically accepted software. For each image in the 2D acquisitions, slice volume was calculated and global LV volumes were estimated via summation across the LV using multiple slices. Real-time imaging data was reconstructed using different image exposure times and frame rates to evaluate the effect of temporal resolution on measured function in each slice via ACS. Finally, global volumetric function of ectopic and non-ectopic beats was measured using ACS in patients with arrhythmias.

ACS provides global LV volume measurements that are not significantly different from manual quantification of retrospectively gated cine images in sinus rhythm patients. With an exposure time of 95.2 ms and a frame rate of > 89 frames per second, golden-angle real-time imaging accurately captures hemodynamic function over a range of patient

heart rates. In four patients with frequent ectopic contractions, initial quantification of the impact of ectopic beats on hemodynamic function was demonstrated.

User-initialized active contours and golden-angle real-time radial CMR can be used to determine time-varying LV function in patients. These methods will be very useful for the assessment of LV function in patients with frequent arrhythmias or in the setting of dynamic changes in preload in animal models.

4.2: Introduction

Cine cardiovascular magnetic resonance (CMR) imaging is the gold standard for quantification of ventricular function. However image quality is often compromised in patients with severe rhythm disturbances. To preserve image quality, most 2D multi-slice CMR methods discard data obtained during an arrhythmia, but beat-to-beat variation in left ventricular (LV) function in arrhythmic patients may be important to provide a more accurate estimate of cardiac function and ventricular performance.

Real-time or ‘single-shot’ CMR (rt-CMR) methods have been developed to acquire 2D images continuously, capturing uninterrupted cardiac motion for each heartbeat. Assessment of LV function in normal subjects and patients has been performed using several rt-CMR methods with varying degrees of accuracy, summarized in Table 4-1 (53–58).

Publication:	Exposure Time (ms)	Frame Rate^{-1} (ms)	Trajectory	Parallel Imaging	Compressed Sensing	Result:
Bauer, et al. I J Cardiovasc Imag 2013 (53)	315	63	Radial	SENSE	No	28% underestimate
	125	25	Radial		No	4% underestimate
Voit, et al. JCMR 2013 (54)	40	40	Radial	SENSE	Yes	10% underestimate
Muthurangu, et al. Radiology 2008 (55)	40	16	Radial	Yes	No	EF: 1.2% lower
Boll et al. JCMR 2005 (56)	83	42	Radial	No	No	4% underestimate
Kuehl, et al. Radiology 2004 (57)	208	100	Radial	No	No	Wall Motion: Comparable
Spuentrup, et al. Radiology 2003 (58)	200	67	Radial	No	No	No Sig Diff
			Spiral			No Sig Diff
Range:	**40-315**	**16-100**				

Table 4-1: Real-time MRI acquisition methods and accuracy of measured hemodynamic values with standard retrospective CINE imaging

These studies imaged patients in sinus rhythm and a single cardiac cycle from each 2D acquisition was selected for LV function assessment. To date, the potential to measure beat-to-beat variation in LV function has not been described using rt-CMR methods.

The first challenge in systematic measurement of beat-to-beat LV function is that there have been no methods presented for continuous quantitative measurement of LV slice volume during several seconds of MR imaging. A single scan can result in thousands of image frames rendering manual segmentation impractical. As a result, we first sought to

develop a quantification method using user-initialized active contours segmentation (ACS) to extract LV slice volume for each image frame, and measure beat-to-beat slice LV function in human subjects (59,60). We validated our approach via comparison to manual segmentation on clinically accepted software.

The second challenge is the determination of adequate temporal resolution for capturing beat-to-beat differences. Temporal resolution, in non-view sharing techniques, describes both the image exposure time (T_{ex}) and the reconstructed image frame rate (FR). However, when view sharing is performed, these two parameters can be evaluated separately. Recent reconstruction techniques have increased achievable undersampling and have led to improved temporal resolution (Table 4-2) (59,61–75). However, there has been a lack of consensus regarding the image exposure time and image frame rates necessary for accurate measurement of cardiac motion and function

We utilized the flexibility of golden-angle imaging to explore the impact of these two parameters (T_{ex} and FR) on measured LV slice function. We reconstructed 2D rt-CMR data with varying number of projections to determine the trade-off between image quality and endocardial border blurring. Varying image frame rates allowed us to explore the trade-off between temporal spacing of LV slice volume measurements and the dataset size. The impact of these two basic image parameters was evaluated in clinical patients using measured LV slice volume. Finally, a preliminary study of patients with arrhythmias illustrates the varying hemodynamic function that can be observed with this technique.

Publication:	Exposure Time (ms)	Frame Rate^{-1} (ms)	Trajectory	Parallel Imaging:	Compressed Sensing:
Li, et al. MRM 2013 (61)	30	30	Radial	SENSE	Yes
Lurz, et al. Eur Heart Journal 2012 (62)	35	35	Radial	SENSE	No
Jones, et al. JMRI 2011 (63)	35	35	Radial	SENSE	No
Seiberlich, et al. MRM 2011 (64)	35	35	Spiral	GRAPPA	Yes
	18	18		GRAPPA	Yes
Seiberlich, et al. MRM 2011 (65)	35	35	Radial	GRAPPA	No
Saybisili, et al. MRM 2010 (66)	151	151	Radial	GRAPPA	
Uecker, et al. NMR Biomed 2010 (67)	20	30	Radial	SENSE	Yes
Uecker, et al. MRM 2010 (68)	250	50	Radial	SENSE	No
	90	18		SENSE	No
Zhang, et al. JCMR 2010 (69)	52	52	Radial	SENSE	Yes
	22	22		SENSE	Yes
Zhang, et al. JMRI 2010 (70)	250	50	Radial	No	No
Lurz, et al. JMRI 2009 (71)	35	35	Radial	Yes	No
Sorensen, et al. IEEE TMI 2009 (59)	125	125	Radial	Yes	No
	50	50			No
Winkelmann, et al. IEEE TMI 2007 (72)	603	2.59	Golden	No	No
	88	2.6			
Spuentrup, et al. Invest Radiol 2003 (73)	200	100	Radial Spiral	No	No
Larson, et al. MRM 2001 (74)	91	45	Radial Multi-Echo	No	No
Shankaranarayanan, et al. Radiology 2001 (75)	150	55	Radial	No	No

Table 4-2: Recent cardiac real-time MRI publications demonstrate improvements image exposure time and frame rate but have not performed quantiative evaluations

4.3: Method

4.3.1: Patients

The study was approved by our Institutional Review Board and all subjects (N=22, 44.7 ± 16.0 years old and 55% male) gave written informed consent. 18 subjects were in sinus rhythm and did not have rhythm disturbances during scanning. 4 patients had frequent rhythm disturbances where premature ventricular contractions occurred at least as frequently as every 4^{th} beat. All patients were referred for assessment of non-ischemic cardiomyopathy: premature ventricular contractions (PVC) (n=8), rule out sarcoid (n=3), hypethrophic cardiomyopathy (HCM) (n=2), arrhythmogenic right ventricular dysplasia (ARVD) (n=2), nonspecific cardiomyopathy (n=6), pulmonary hypertension (n=1).

4.3.2: Image Acquisition

CMR was performed on a 1.5 T clinical imaging system (Avanto, Siemens Healthcare, Erlangen, Germany) equipped with nominal 40 mT/m magnetic field gradients, body RF transmit and a 32-channel, anterior and posterior RF receiver array.

Cine-CMR was obtained using a conventional 2D, breath-held, multi-slice, retrospectively-gated, balanced steady-state free-precession (bSSFP) sequence with the following imaging parameters, TE = 1.12-1.31 ms, TR = 2.24-2.62 ms, matrix = 144-192 x 192, FOV = 240-320 mm x 240-400 mm, pixel size = 1.25 – 2.08 x 1.25 - 2.08 mm, BW

= 930 Hz/pixel, phases = 30, slices = 12-16, slice thickness = 8 mm, slice spacing = 10 mm and temporal resolution = 29.8 ± 7.0ms.

Real-time data was obtained using a 2D, multi-slice, free-breathing bSSFP sequence with a golden-angle radial trajectory with the following imaging parameters, TE = 1.4 ms, TR = 2.8 ms, number of radial k-space data = 128, FOV = 220 mm - 300 mm, pixel size = 1.72 – 2.34 x 1.72 – 2.34 mm, bandwidth = 1184 Hz/pixel, slice thickness = 8 mm, and k-space sampling according to the golden-angle $\Phi = 111.25°$. Imaging was performed in the short axis of the left ventricle over the same volume as cine-CMR by copying slice positions acquired in cine-CMR. 4000 radial projections (11 seconds) per slice were acquired in sinus rhythm. 6000 radial projections (17 seconds) per slice were acquired in patients with arrhythmia.

4.3.3: Reconstruction of real-time CMR

Real-time image reconstruction was performed offline using a non-Cartesian SENSE algorithm in open-source software (45,47,59). Examples of the image quality of conventional cine (**A-B**) and the real-time reconstruction with 34 radial projections (**C-D**) in a patient with frequent rhythm disturbances are shown in the figure below.

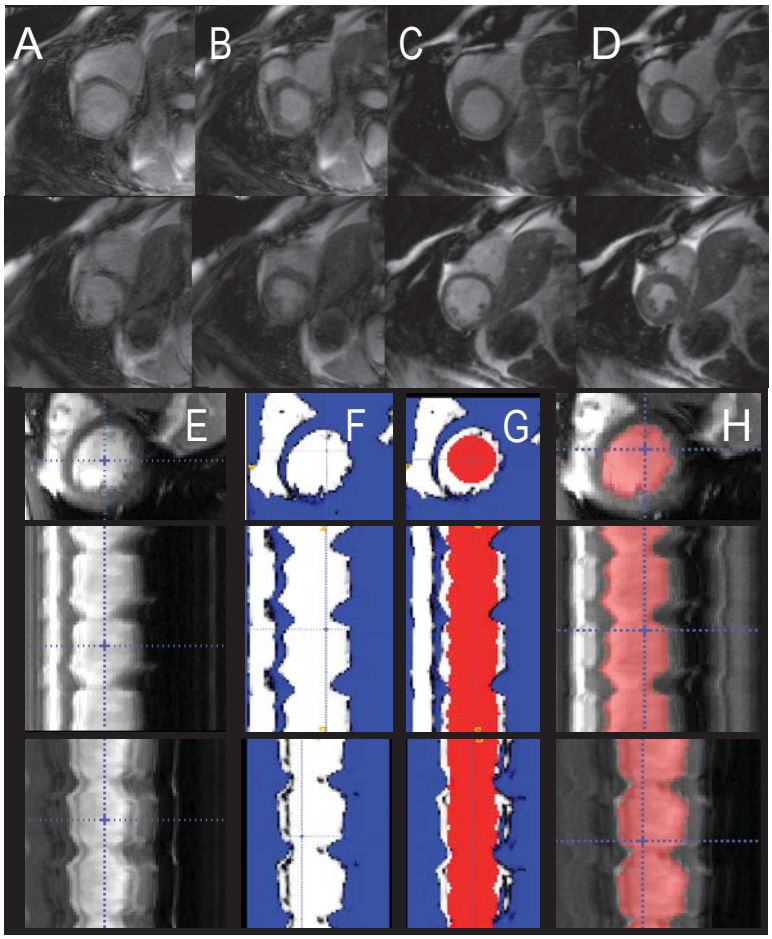

Figure 4.1: Example of image quality and visual depiction of quantification process. Two slice locations imaged during severe arrhythmia demonstrate the corruption of conventional CMR during **A** end-diastole and **B** end-systole. Real-time imaging does not demonstrate corruption at **C** end-diastole and **D** end-systole. Panels **E**-**H** illustrate the active contour segmentation (ACS) process. The short axis image is shown in the top row. The second and third rows illustrate projections along time. **E** Image sequences are loaded as 3D volumes (2D+t) into software. **F** The user defines an intensity threshold, which defines the endocardial border and results in a feature image. **G** Region growing is then performed inside the feature image. **H** The resulting segmentation can be manually corrected for any errors. Adapted from (76).

We reconstructed data with maximum view sharing, resulting in one image frame for each radial projection. For the highest image frame rate, there were approximately 4,000 images for each 11-second acquisition per slice location. Reconstruction of a complete multi-slice dataset took approximately 45 minutes for 34 radial projections per image

with a 357 frames per second (fps) reconstructed frame rate on a workstation with a single graphics processing unit (GPU).

4.3.4: Conventional Hemodynamic Quantification

Gold-standard volumetric measurements were obtained using JCMR/SCMR 2013 guidelines for manual segmentation in clinically accepted software (Qmass, Medis, Netherlands). Detailed tracing of the endocardial border in standard 2D multi-slice, cine-CMR images yielded end-diastolic and end-systolic LV slice volume (EDV and ESV) estimates for each slice (slice area multipled by slice thickness). Papillary muscles were excluded from segmentations and resulting volume estimates. Volumetric quantification of two cardiac phases was obtained in approximately 10-15 minutes per patient. Global measurements of EDV and ESV were obtained by summation of of slice volumes from the short-axis stack.

4.3.5: Active Contour Segmentation (ACS)

Quantification of slice volume in all image frames of a 2D acquisition was performed offline through user-initialized active contour segmentation (ACS) (ITK-SNAP, University of Pennsylvania, Philadelphia, PA) as detailed in Figure 4.1 **(E-H)** (60). 2D image data was arranged in a 3D stack Nx x Ny x Nt; the typical size was 128 x 128 x 4,000. Manual intensity thresholding was used to generate a set of feature images of the LV intraventricular volume. Ventricular segmentation was automatically initialized using a 3 x 3 x Nt pixel column centered in the ventricle. 3D active contour segmentation was performed using region competition with user-defined, patient- and slice-specific balloon

and curvature forces (77). The advantage of this arrangement was that contours between consecutive image frames were smooth, resulting in temporally consistent and smooth LV slice area. Papillary muscles were excluded from the segmentation and volume calculation using the feature image and, if necessary, manual correction. Typically, 1-2 slices per patient would require manual correction due to LV outflow tract, papillary muscle, or radial streak artifact. Using ACS, segmentation takes approximately 3 minutes for a single slice and 30 minutes for the entire LV (all slices and all phases). LV slice volume was quantified by multiplying the slice area multiplied by slice thickness and slice ED and ES volumes were automatically determined from local maxima and minima using a peak detection algorithm (Matlab, The MathWorks, Natick, MA). Global EDV, ESV, stroke volume (SV), and ejection fraction (EF) were measured by summation of measured slice EDV and ESV values.

4.3.6: Effect of image parameters on measured LV function

To determine the effect of imaging parameters on measured LV slice function, we reconstructed the same golden-angle radial data at different temporal resolutions. Although there are a large number of potential reconstruction parameters that contribute to temporal resolution, we focused on the image exposure time T_{ex} and frame rate FR.

In this image acquisition, image exposure time is the number of radial projections used to reconstruct a single image frame and is analogous to camera exposure time. Like camera exposure time, increasing the number of radial projections results in high image signal-to-noise ratio (SNR). However, it also introduces blurring due to cardiac motion.

Increasing the exposure time leads to blurry endocardial wall boundaries, which compromises endocardium visualization.

The image frame rate was defined as the number of image frames per second. It was possible for the frame rate to exceed the exposure time because a single projection could be shared in more than one image frame. The maximum possible frame rate, with view sharing is determined by the TR of the bSSFP sequence (TR = 2.8 ms leads to a FR = 357 fps). Decreasing the amount of view sharing decreases the size (and time) of the reconstruction and reduces the number of images for segmentation. However, it could result in undersampling of the slice volume curves leading to errors in both volume and time detected for slice EDV and ESV values.

Seven datasets in normal sinus rhythm were used to investigate the sensitivity of measured LV function to changes in exposure time and frame rate. These patients had exact agreement in slice location between cine and real-time images. The patients had a range of normal heart rates (54 - 86 bpm). For each patient, a single mid-ventricular slice location acquired using both real-time and cine imaging was selected for analysis. Exposure time was varied by reconstructing images from N_p = 10-300 radial projections, corresponding to an exposure time $T_{ex} = TR*N_p$ = 28-840 ms. The image frame rate was evaluated by modifying the number of shared projections at fixed exposure time T_{ex} = 95.2 ms. This resulted in image data with display frame rates FR of 1.2 - 357 fps. For each dataset, ACS was performed to measure time-varying slice volume and the relationship between measured slice EDV, ESV, SV, and EF was quantitatively compared to manual segmentation of the corresponding cine-CMR slice.

4.3.7: Statistical Analysis

A two-tailed paired Student's t-test ($p < 0.05$) was used to detect significant differences in hemodynamic values between the three different approaches (cine with QMass, cine with ACS, and rt-CMR with ACS). A Bland-Altman test was performed to measure differences in measured hemodynamics between the approaches. A two-tailed paired Student's t-test ($p<0.05$) was used to detect significant differences in slice hemodynamic values at different image exposure times and frame rates.

4.4: Results

4.4.1: Validation of active contour segmentation (ACS)

To validate the use of ACS, we processed cine-CMR images with ACS and compared measured LV values to those obtained by manual segmentation of the same cine-CMR images. The results from 18 clinical patients in sinus rhythm are shown in Figure 4.2.

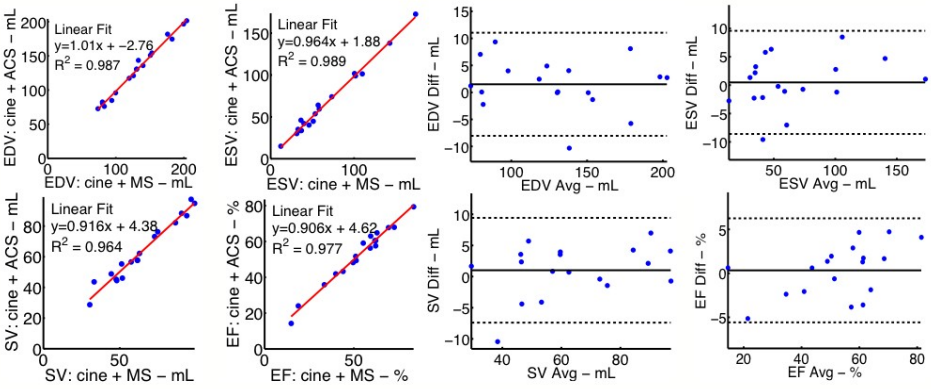

Figure 4.2 Consistency between global LV function measured using manual and semi-automated segmentation (ACS) of standard retrospectively gated cine images. **Left** Correlation between end-diastolic volume (top left), end-systolic volume (top right), stroke volume (bottom left), and

ejection fraction (bottom right) obtained via manual segmentation (MS) using QMass and ACS. **Right** Bland Altman analysis for the same measurements. Adapted from (76)

The patients had a range of global volume and function (EDV range = 80 - 204 mL, ESV range = 31 - 174 mL, EF range = 14.8 - 72.7%). The same cine-CMR images were processed using the two segmentation methods and there was no significant difference in measured global EDV ($p = 0.20$), ESV ($p = 0.66$), SV ($p = 0.32$), or EF ($p = 0.63$). Bland-Altman analysis shows negligible biases, which are not statistically significant (bias: EDV = 1.5 mL, ESV = 0.5 mL, SV = 1.0 mL, and EF = 0.3%).

4.4.2: Influence of image exposure time and frame rate on measured LV function

After validation of ACS, we determined the effect of image exposure time on measured LV slice function by reconstructing golden-angle radial real-time data using a varying number of radial projections. We performed ACS on a single slice in seven clinical patients in sinus rhythm with heart rates in normal physiologic range (54 - 86 bpm). Comparison of measured slice EDV, ESV, SV, and EF to the corresponding cine slice values allowed for the percent error of real-time measurements with respect to the manually segmented cine data to be calculated and averaged among the patients. Figure 4.3 shows results from one subject (**A-D**) as well as the error observed from the seven subjects (**E-H**).

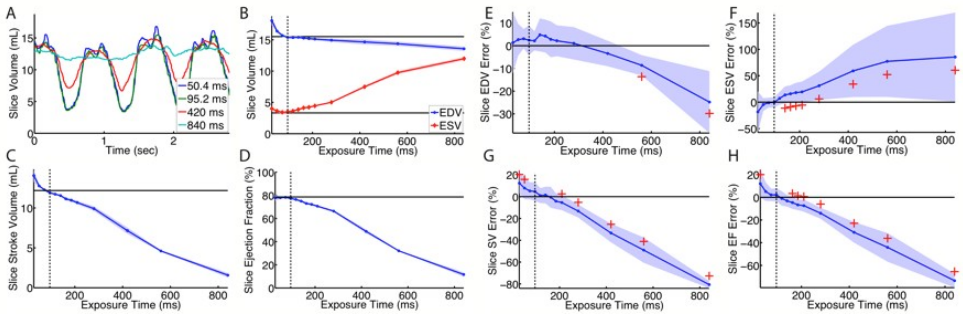

Figure 4.3 Effect of exposure time on measured LV function. Panels **A**-**D** illustrate the effect of exposure time on measured slice volume in one patient. **A** Measured LV slice volumes for 4 exposure times (50-840 ms) in a clinical patient in sinus rhythm with a heart rate of 76 bpm. **B** Dependence of measured end-diastolic (blue) and end-systolic (red) slice volumes on exposure time. **C** The effect of exposure time on measured stroke volume in a slice. **D** The effect of exposure time on measured ejection fraction in a slice. The corresponding cine slice measurements are depicted with a horizontal black line in **B**, **C** and **D**. The real-time values depict the mean (solid line) and standard deviation (shaded area) of the volume measured across real-time beats. Panels **E**-**H** illustrate the error between manual segmentation of cine images and semi-automated processing of real-time images from single slices in 7 different patients. The change in the measured error (blue line) and standard deviation (blue shaded area) as a function of exposure time are shown for measured slice EDV (**E**), ESV (**F**), SV (**G**), and EF (**H**). An exposure time of 95.2 ms resulted in no statistical difference of the measured error (vertical black dotted line). The occurrence of a statistically significant difference is shown in each panel with red crosses. Adapted from (76)

In all patients, there was a progressive reduction in measured slice EDV and SV and an increase in slice ESV with increasing exposure time, consistent with a blurring of cardiac motion, specifically blurring of the endocardial wall. We found that an exposure time of 95.2 ms (34 radial projections) resulted in the best LV volume accuracy as compared to cine. Higher exposure times resulted in loss of accuracy due to cardiac blurring while lower exposure time results in loss of accuracy due to increased undersampling artifacts and loss of signal-to-noise ratio which makes accurate segmentation challenging (seen in the increased error bars).

We next determined the effect of image frame rate on measured LV slice volume by varying the number of shared radial projections. Results from one subject (**A-D**) and group values (**E-H**) appear in Figure 4.4.

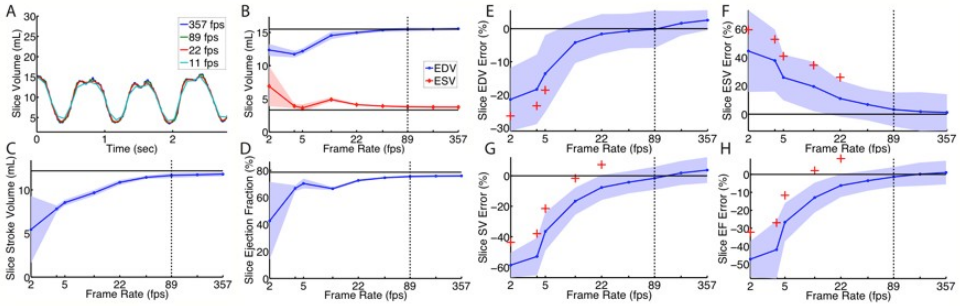

Figure 4.4 Effect of image frame rate on measured LV function. Panels **A**-**D** illustrate the effect of frame rate on measured slice volume in one patient. **A** Measured LV volumes for 4 frame rates 11, 22, 89, and 357 fps in a single clinical subject in normal sinus rhythm (heart rate = 76 bpm) from images with an exposure time of 95.2 ms. **B** Dependence of measured end-diastolic (blue) and end-systolic (red) slice volumes on frame rate. **C** Effect of image frame rate on measured stroke volume in a slice. **D** Effect of frame rate on measured ejection fraction in a slice. The corresponding cine slice measurements are depicted with a solid black line in B C, and D. Real-time measurements are shown with the mean (solid colored line) and standard deviation (shaded area) obtained from several beats during the acquisition. Panels **E**-**H** illustrate the mean error between manual segmentation of cine images and semi-automated processing of real-time images from single slices in 7 different patients. The mean error (blue line) and standard deviation (shaded area) as a function of frame rate is shown for measured slice EDV (**E**), ESV (**F**), SV (**G**), and EF (**H**). The hemodynamic values show statistically significant errors (red cross) at frame rates lower than 44 fps. The black dotted line at 89 fps illustrates the close agreement in hemodynamic values. Adapted from (76)

As the frame rate decreases, the size of the dataset processed decreased and the volume curve was increasingly undersampled, which resulted in errors in both time and volume when selecting maximum and minimum volumes. Our findings indicate that frame rates above 89 fps provide accurate measurement of LV slice volumes relative to values obtained via manual segmentation of cine-CMR for all observed heart rates.

4.4.3: Validation of the adequacy of real-time imaging for volume assessment:

Despite variation in FOV, the difference in pixel length or pixel area between cine and real-time acquisitions was not statistically significantly different (paired t-test yielded p-values of p = 0.25 and p=0.97, respectively). Using the exposure time (95.2 ms) and frame rate (89 fps) , global LV volume measurements made using real-time images and ACS were compared to those obtained from cine images using ACS (Figure 4.5).

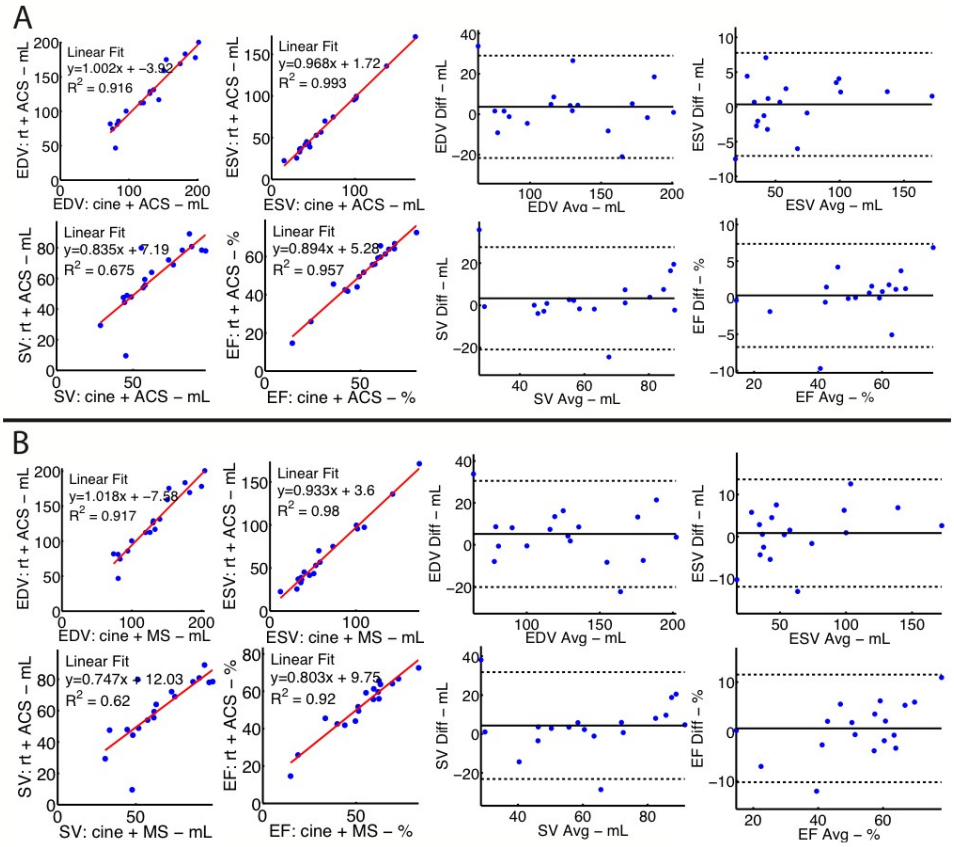

Figure 4.5 Consistency between global LV function measured using manual and semi-automated segmentation (ACS) of both cine and real-time datasets. Panel **A** illustrates the consistency in measured hemodynamic values obtained from ACS in cine and real-time images. **Left** Correlation between global end-diastolic volume (top left), end-systolic volume (top right), stroke volume

(bottom left), and ejection fraction (bottom right) obtained via ACS of cine and real-time image sets. **Right** Bland Altman analysis of the measurements. Panel **B** illustrates the agreement between LV function measured via manual segmentation of cine images and ACS of real-time image data **Left** Correlation between end-diastolic volume (top left), end-systolic volume (top right), stroke volume (bottom left), and ejection fraction (bottom right). **Right** Bland Altman analysis of the measurements. Adapted from (76)

There was no significant difference in global EDV ($p = 0.24$), ESV ($p = 0.69$), SV ($p = 0.26$), or EF ($p = 0.72$). Bland-Altman analysis shows negligible biases, which are not statistically significant (EDV = 3.7 mL, ESV = 0.4 ml, SV = 3.3 mL, and EF = 0.3 %). Furthermore, measurements using the real-time image acquisition and ACS were compared to manual segmentation of cine-CMR images (Figure 4.5**B**). Again, there was no significant difference in global EDV ($p = 0.10$), ESV ($p = 0.58$), SV ($p = 0.20$), or EF ($p = 0.62$). Bland-Altman analysis shows negligible biases, which are not statistically significant (bias: EDV = 5.2 mL, ESV = 0.8 mL, SV = 4.3 mL, and EF = 0.6%).

4.4.4: Evaluation of time-varying LV slice volumes:

Representative cine (black) and real-time (blue/red) slice volume measurements at a representative slice position are shown in Figure 4.6**A.**

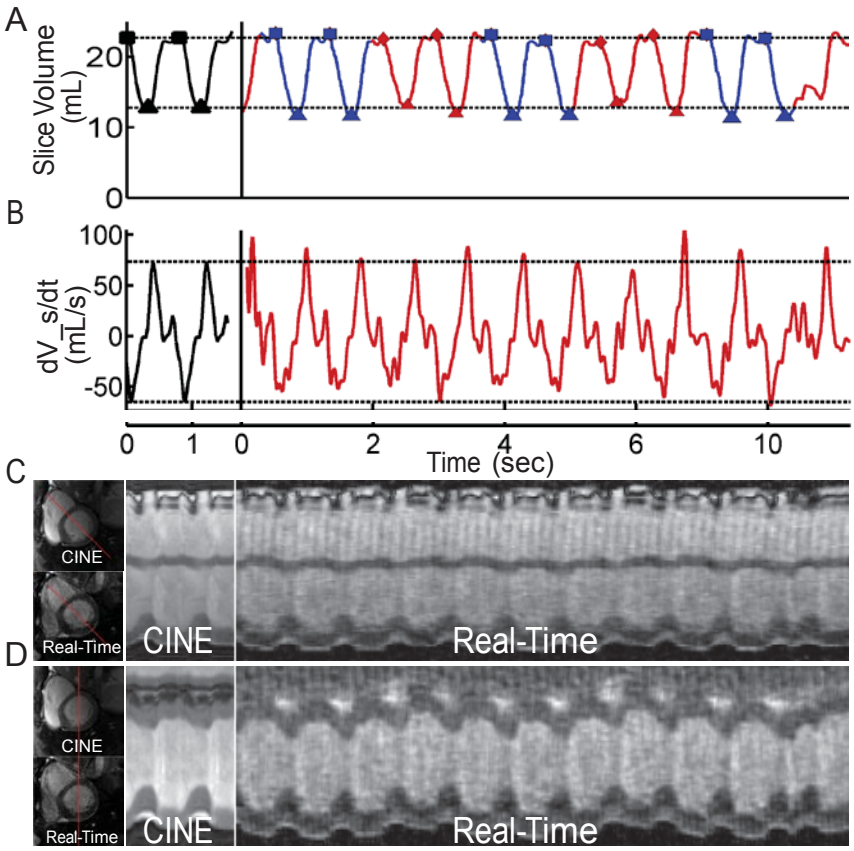

Figure 4.6 Cine and real-time LV slice volumes and volume rates in a single clinical patient in predominantly sinus rhythm (heart rate = 76 bpm). **A** Single-slice volume over time for cine (black) and real-time (red = end-expiration, blue = inspiration). In the cine images, two cardiac cycles are shown by repeating the image data to observe the continuity in volume around end-diastole. Slice end-diastolic volume (EDV) (square) and end-systolic volume (ESV) (triangle) points were identified in both cine and real-time data for volumetric comparison. Slice EDV and ESV from manual segmentation of cine images are plotted as dashed horizontal lines. Respiratory phase was determined by tracking diaphragm motion. **B** Slice Volume change rate (dV_s/dt) for cine and real-time data. Maximum and minimum dV_s/dt from cine frames are plotted as dashed horizontal lines. **C** 1D projections through cine and real-time images, with the line indicating the projection location which intersects the anteroseptum and inferolateral wall, and **D** 1D projections through cine and real-time images, with the line indicating the projection through the anterior and inferior walls. In the real-time data, a single arrhythmic event can be seen (t = 10 sec). Adapted from (76)

There was close agreement between the slice volume curve shape (normalized correlation coefficient = 0.96) as well as measured slice end-systolic and end-diastolic

values. In all patients, the slice volume was affected by respiratory motion. Since cine images were acquired at end-expiration, volumes obtained via real-time during end-expiration were utilized for volumetric comparison (red). Periods of end-expiration were identified based on the diaphragm motion observed in the images. A single PVC was observed at approximately t=10 sec. The ability of this technique to accurately capture the change in slice volume (dV_s/dt) throughout the cardiac cycle is shown in the Figure 4.6**B** (correlation coefficient = 0.90). The maximum and minimum dV_s/dt observed from cine values agree with those obtained during the real-time scan. Furthermore, the features of the curve were similar in both techniques, with the most rapid change in LV slice volume occurring during ventricular relaxation. The change in volume demonstrates that the real-time method can accurately measure the change in slice filing and ejection. Figure 4.6**C** and Figure 4.6**D** show 1D projections through the left ventricle for both methods along two different directions.

4.4.5: Acquisition of real-time images in patients with persistent rhythm disturbances

After validating the ACS quantification and real-time imaging parameters in patients without rhythm disturbances, 4 clinical patients with rhythm disturbances were imaged. For one of these subjects, the cine images obtained at end-diastole as well as a projection through the heart over the cardiac cycle are shown in Figure 4.7**A-B**. Real-time imaging allows for severe multi-focal PVCs to be visualized along the projection (Figure 4.7**C-D**).

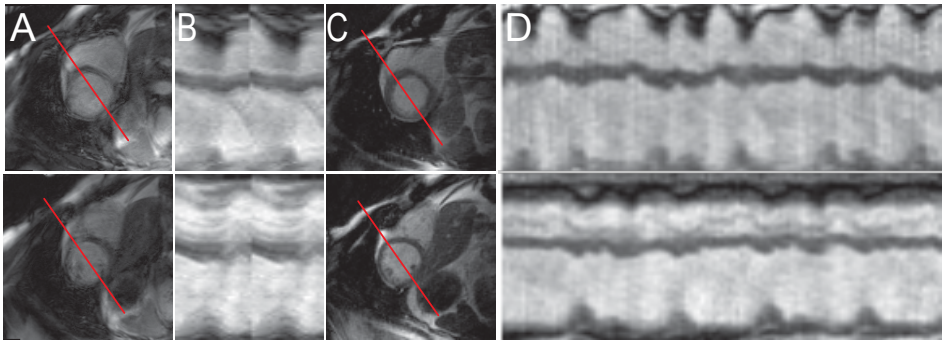

Figure 4.7 Comparing cine acquisition with real-time acquisition in a patient with severe rhythm disturbances at two slice locations (top and bottom) **A** Cine acquisitions with the line indicating the location of 1D projection. The images are blurred due to acquisition during ectopic beats **B** 1D projection shows temporally blurred cine acquisition due to errors in ECG-gating. **C** Real-time end-diastolic images at two corresponding slice locations. The images are free from corruption due to ectopic beats. **D** The real-time acquisition shows the frequency of ectopic beats with no spatial or temporal blurring. Adapted from (76)

In addition to obtaining images of high quality for clinical interpretation, quantification of slice volume from real-time images via ACS permitted evaluation of the effects of the rhythm disturbances on ventricular volumes. Slice-by-slice analysis of ventricular volumes of another patient is shown in Figure 4.8.

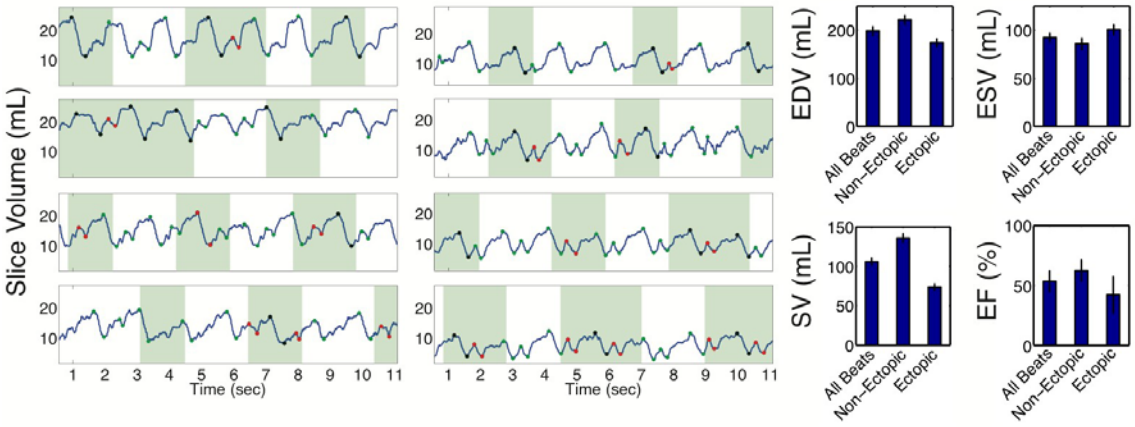

Figure 4.8 Analysis of one patient with frequent PVCs. **Left** Slice volume over time curve of all short axis slices from base to apex. The slice volume curve allows for separation of end-diastolic and end-systolic slice volumes from PVC contractions (red points within the green boxes) from

non-ectopic end-diastolic volume (black points within green boxes). Green boxes illustrate end-expiration period of respiration based on visualization of the diaphragm. **Right** Volumetric analysis that included all beats (ectopic and non-ectopic), only ectopic beats, and only non-ectopic beats. Adapted from (76)

For each slice location, the observed slice EDV and ESV varied depending on the timing of the PVC. To obtain global volumetric values, the average slice EDV and SV for each beat morphology (within the end-expiratory period) were summed across slice locations. End-expiratory periods were identified by visual observation of diaphragm motion. As a result, volumes from different slices were combined to characterize the same type of beats. For this patient, global EDV, ESV, SV, and EF from all beats, ectopic beats, and non-ectopic beats are shown in bar graphs. Table 4-3 shows the values for all four arrhythmic subjects.

Subject:	**End-Diastolic Volume (mL)**		**End-Systolic Volume (mL)**		**Ejection Fraction (%)**	
	Non-Ectopic	Ectopic	Non-Ectopic	Ectopic	Non-Ectopic	Ectopic
1	231.4 ± 9.9	165.6 ± 7.3	84.4 ± 4.4	106.6 ± 4.5	63.5 ± 9.2	35.7 ± 9.6
2	149.4 ± 5.9	114.8 ± 5.2	69.7 ± 3.8	84.9 ± 5.1	53.3 ± 8.4	26.0 ± 14.9
3	128.3 ± 7.6	88.7 ± 6.2	57.9 ± 4.7	54.9 ± 4.5	54.9 ± 8.2	38.2 ± 13.5
4	130.3 ± 7.3	104.1 ± 5.8	44.9 ± 4.5	42.1 ± 2.4	65.5 ± 13.4	59.6 ± 9.6

Table 4-3 Variation in volumetric evaluation due to ectopic contractions. Adapted from (76)

4.5: Discussion

We proposed and validated an active contour segmentation (ACS) algorithm for measurement of time-varying LV slice volume and estimation of global LV function. We used this method to determine the impact that two key components of temporal resolution, image exposure time and frame rate, have on accurate quantification of LV function by reconstructing golden-angle radial data at multiple image exposure times and frame rates. Furthermore, we illustrate that our method of real-time imaging combined

with ACS, can provide estimates of time-varying global LV function during severe arrhythmias.

For nearly all types of CMR sampling trajectories, resolution must be determined *a priori*, so it is not known whether spatial, temporal resolution and signal-to-noise ratio are optimal or if Nyquist undersampling artifacts are minimized. The golden-angle radial trajectory is one exception; it allows for reconstruction of images from any number of radial views and a large number of these radial views are guaranteed not to overlap, permitting uniform k-space sampling density, regardless of the number of projections chosen for reconstruction (72). Like all radial trajectories, view sharing is also possible. Overall, the flexibility to control both exposure time and frame rate resulted in a large continuum of possible image reconstructions with varying temporal resolution, for which the accuracy of a real-time scan could be determined retrospectively.

As reported in Table 4-1 and Table 4-2, there are a number of previous rt-CMR studies that employed considerable variability in exposure time and frame rate. Our results indicate that golden-angle radial sampling permits accurate measurement of LV volume with image exposure times of 95 ms at high image frame rates (> 89 fps).

Bauer et al showed that imaging with an exposure time of 315 ms and frame rate of 16 fps or exposure time of 125 ms with frame rate of 40 fps does not result in accurate LV estimation and our results agree with this evaluation (53). Voit et al used a much shorter exposure time (40 ms) and frame rate of 25 fps and found an underestimation of EF (54). For our reconstruction, the loss of image quality associated with a 40 ms exposure

time prohibited robust quantification at all slice positions. It is possible that the underestimation reported was due to a lack of image quality and the use of view sharing to increase the exposure time while maintaining a high frame rate may allow for more accurate volumetric evaluation.

The image exposure time we found is longer than recent publications, but it may be advantageous due to the higher SNR (61–65,67–71). Although, the long exposure time may introduce errors during rapid wall motion, the use of a very high image frame rate (>89 fps) may limit these errors. The exposure time and frame rate we determined may be impacted by several elements of our approach including the radial k-space trajectory, the spatial resolution (128 points per readout), and quantification method (semi-automated extraction of slice volume). For different approaches including spiral or Cartesian imaging, compressed-sensing reconstructions, higher spatial resolution, or different imaging tasks such as wall motion abnormality imaging, a more restrictive set of parameters may be necessary.

As discussed in Setser et al, the optimal rate to sample the left ventricular volume curve must be sufficient to capture the highest frequency cardiac motions (78). They reported 40 ms sampling rate (frame rate^{-1}) was sufficient for measurement of LV function at heart rates up to 100 bpm. Our findings (> 89 fps) indicate a higher frame rate is necessary. This might be due to the interplay between frame rate and image exposure time or the impact of radial k-space sampling. Although a higher frame rate is desirable for accurate sampling the LV volume curve, it directly impacts the size of the reconstruction problem and necessary computational power. As a result, the determination of the minimum

frame rate necessary is important for online reconstructions as well as subsequent post-processing steps.

An additional advantage of retrospective reconstruction of image frames is that the reconstruction can be adapted to changes in heart rate during pharmacologic or exercise stress testing, although the relationship between exposure time, frame rate and LV function should again be determined.

One limitation of this study is that temporal filtering or regularization of either k-space data or image frames were not used, since this would complicate interpretation of the temporal resolution (79). However, the framework presented offers an approach to measure the impact of these techniques.

One major impediment to routine use of real-time imaging is the task of synchronizing data obtained from different slices to obtain meaningful cardiac volumes. In this method, we use the maximum and minimum slice volume. Previous studies have utilized this assumption (53,54,56,58) and in this work, we are able to demonstrate that the difference from cine-CMR is small, as shown in Figure 4.2.

For real-time imaging to replace conventional cine acquisitions, other capabilities beyond volumetric quantification such as the evaluation of regional wall motion abnormalities, are necessary. Unfortunately, we are unable to evaluate this in our patient population due to lack of regional wall motion abnormalities. New constraints and future work is needed to evaluate regional wall motion.

It is possible that the heart position varied between breathheld acquisitions (cine imaging) and end-expiration during free breathing (real-time imaging). This potential source of error is included in the comparison of cine+ACS and rt+ACS and no significant differences in measured volumes were observed.

Conventional cine CMR is severely corrupted during ectopy, which necessitates the use of arrhythmia rejection techniques that may not work well. As a result, real-time methods are essential in patients with severe arrhythmia to characterize LV function. Real-time imaging also allows for imaging of ectopic beats and we present an initial quantitative beat-to-beat analysis of time-varying LV function in patients with severe arrhythmia where characterization of sinus, PVC, and post-PVC beats become possible. In patients with sinus rhythm, beat-to-beat left and right ventricular volumes obtained during changes of respiration might be important in diseases such as constrictive pericarditis.

4.6: Conclusions

In conclusion, we demonstrated that 2D golden-angle rt-CMR combined with ACS can be used to obtain accurate slice volume analysis in clinical patients in sinus rhythm. The use of LV slice volume (and measures such as slice EDV, ESV, SV, and EF) to evaluate imaging and reconstruction parameters provides a quantitative and physiologically-based approach to evaluate parameters of different imaging techniques. Initial results obtained from patients with severe rhythm disturbances illustrate the clinical potential of this 2D method to obtain time-varying LV function. Future work is planned to improve

this technique to combine ECG information with image frames as well as to explore simultaneous acquisition of multiple slices.

Chapter 5: Retrospective CINE MRI Reconstruction of Multiple Beat Morphologies

5.1: Abstract

Despite determining that real-time MRI provides an accurate measure of LV slice volume (Chapter 4), multi-shot acquisitions hold the potential for higher spatial or temporal resolution imaging or higher image quality. Non-periodic LV motion can severely compromise cine MR image quality in subjects with arrhythmia or during preload occlusions.

The purpose of this study was to develop a retrospective reconstruction method to obtain high quality images of different left ventricular (LV) heartbeat morphologies, uncorrupted by motion artifacts, in arrhythmia subjects within a single breath-hold.

Real-time golden angle radial MRI data was obtained in normal subjects and two subjects with abnormal cardiac rhythms and images of distinct beat morphologies were reconstructed using a novel reconstruction approach. Real-time radial k-space data were reconstructed using a non-Cartesian SENSE algorithm at high frame rate and long exposure time. From these images, heartbeat morphology categorization was performed by image segmentation to derive an image-based navigator of cardiac motion. For the final reconstruction, each observed beat morphology was retrospectively reconstructed to generate a composite cine of all observed morphologies at high spatiotemporal resolution.

The use of LV volume image-based navigators to detect distinct beat morphologies was evaluated in 3 volunteers in sinus rhythm. Image quality was evaluated with image contrast and edge sharpness criteria and quantitatively compared to standard cine images. Two subjects with rhythm disturbances were imaged to obtain high quality and high spatiotemporal resolution images of the observed beat morphologies.

In subjects with frequent and repeated rhythm disturbances, the proposed approach allows for observation of different beat morphologies. In the presence of rhythm disturbances, the method resulted in accurate data synthesis and higher scan efficiency.

5.2: Introduction

Retrospective cine magnetic resonance imaging (MRI) is a preferred acquisition and reconstruction approach for cardiac imaging due to several key properties, such as very high image signal-to-noise ratio and spatiotemporal resolution, preservation of a magnetization steady-state and uninterrupted scanning throughout diastole (41). In cine MRI, a subset of the total image data is acquired at each phase of the cardiac cycle and, after several heart beats, there is sufficient data for image reconstruction. Cardiac rhythm regularity is essential to accurately synthesize image data across multiple heartbeats; therefore non-periodic or inconsistent heart motion poses a considerable problem for the acquisition and reconstruction of cine MRI data.

Arrhythmia rejection is an important approach to prevent inclusion of inconsistent motion data during cine MRI, but there are some challenges that limit its usefulness. In arrhythmia rejection, each RR-interval is compared to a reference obtained during

normal rhythm, and if the difference exceeds a predefined tolerance, then the data is rejected and immediately reacquired in the next heartbeat (80). Even if arrhythmia rejection is used, however, there are several situations in which the cine MRI data could be combined improperly and result in image corruption (Figure 5.1).

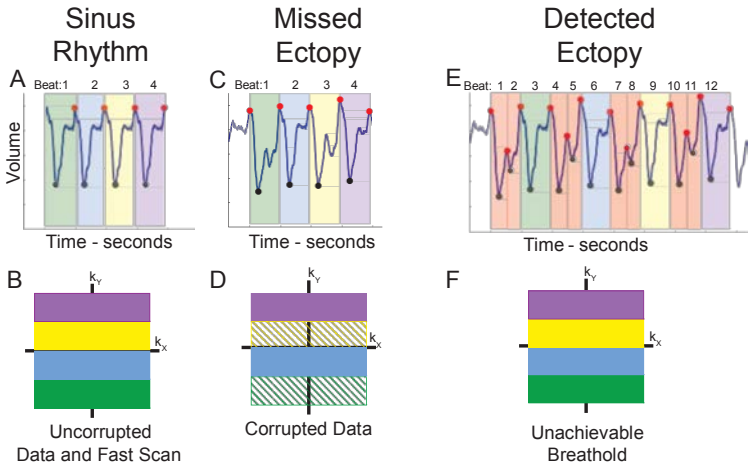

Figure 5.1 Mechanisms for retrospective cine image corruption in the presence of arrhythmias. **A** Normal LV volume in sinus rhythm (end-diastole = red points and end-systole = black). **B** In the normal subject in **A**, 4 k-space subsets (shots) were acquired, with 1 subset acquired per heartbeat. Each k-space subset color corresponded to the heartbeat in which it was sampled in **A**. When all subsets were acquired, k-space was fully sampled and images were reconstructed. **C**, **D** Image corruption occurred when ectopic data was reconstructed as if it were normal data. This happened when the ectopic depolarization was not detected and the observed RR-interval was not rejected. In this example, two ectopic contractions occurred (green and yellow boxes), but were not rejected. The corrupted portions of k-space acquired during these beats are shown with a hashed pattern in **D**. **E**, **F** Image corruption also occurred when ectopic beats were detected and rejected (red boxes), however, the decreased scan efficiency resulted in a unachievable breath-hold duration and respiratory motion artifacts. Adapted from (81).

For instance, the morphology of an ectopic contraction, such as an irregular, prolonged, or widened QRS complex, may not be correctly detected as a trigger event and cause acceptance of ectopic data. Arrhythmia rejection can also result in corrupted images if frequent ectopic contractions result in unachievable breath-hold durations and

respiratory motion occurs during the acquisition. Altogether, these potential errors make imaging using ECG-gating prone to corruption by arrhythmias.

Another concern is that ectopy is a fundamental aspect of the subject's cardiovascular state so imaging these events may be important for determination of true function. Cine MRI assumes that all heartbeats are identical and integrates these data to create a synthetic beat. The imaged beat masks the features of beats that may be categorically different with respect to several important functional parameters, such as stroke volume or ejection fraction. Methods are needed that provide more detail about each category of beat, normal or ectopic.

To improve cine MRI image quality in the presence of arrhythmias, we developed an MRI acquisition and retrospective reconstruction approach that detects and reconstructs different beat morphologies. When certain morphologies were repeatedly observed, the data was combined to provide high spatial and temporal resolution images of each beat type. We quantified the intrinsic variation of measured slice volume during sinus rhythm in volunteers and determined the feasibility of using the slice volume signal to reconstruct high quality images of recurring sinus beats. Then, data acquired in patients with arrhythmias was successfully reconstructed. During bigeminy, multiple beat morphologies were imaged and separately reconstructed. In the presence of irregular arrhythmia, the approach allowed for improved arrhythmia rejection and improved scan efficiency.

5.3: Method

5.3.1: Human Subjects

The study was approved by the University of Pennsylvania Institutional Review Board and all subjects gave informed written consent. We imaged five human subjects, three volunteers in sinus rhythm and two subjects with different rhythm disturbances: one with irregular ventricular bigeminy and one with premature ventricular contractions (PVCs).

5.3.2: Image Acquisition

Cardiac MRI was performed on a 1.5 T clinical imaging system (Avanto, Siemens Healthcare, Erlangen, Germany) equipped with nominal 40 mT/m magnetic field gradients, body RF transmit and a 32-channel, anterior and posterior RF receiver array. In all subjects, three short-axis slice locations were imaged at mid-ventricle.

To enable reconstruction of different beat morphologies, we collected real-time data using a 2D golden-angle radial trajectory (82). As will be elaborated in the next section, golden angle sampling permitted multiple image reconstructions at varying spatiotemporal resolution and assured that a particular radial angle was only sampled once. These properties ensured high k-space sampling uniformity in all reconstructions, despite the presence of arrhythmias. The data was collected with the following imaging parameters, TE = 1.4 ms, TR = 2.8 ms, number of radial k-space data = 128, FOV = 220 mm - 300 mm, bandwidth = 1184 Hz/pixel. Consecutive k-space projections were acquired at golden angle intervals $\theta_{!!} = \theta_! + 111.25°$. After the initiation of the scan,

subjects were instructed to hold their breath and then to release after a period of 15-20 seconds. In the two subjects with arrhythmias, multiple beat morphologies were observed within this time period.

As a reference, retrospective Cartesian cine MR images were obtained using a 2D breath-held, multi-slice, retrospectively-gated, balanced steady-state free-precession sequence with the following imaging parameters, TE = 1.16 ms, TR = 2.32 ms, matrix = 156 x 192, field-of-view = 276 mm x 340 mm, BW = 930 Hz/pixel, slice thickness = 8 mm, gap = 2 mm and temporal resolution = 21.1 – 35.6 ms. In subjects with rhythm disturbances, arrhythmias resulted in unachievable breath-hold durations.

5.3.3: Image Reconstruction

Three image reconstructions were performed from golden angle radial k-space data at different spatiotemporal resolutions to produce the final composite cine images. As we will discuss, the first reconstruction had high spatial resolution, the second had high temporal resolution, and the final reconstruction had both high spatial and temporal resolution. An overview of this approach is shown in Figure 5.2.

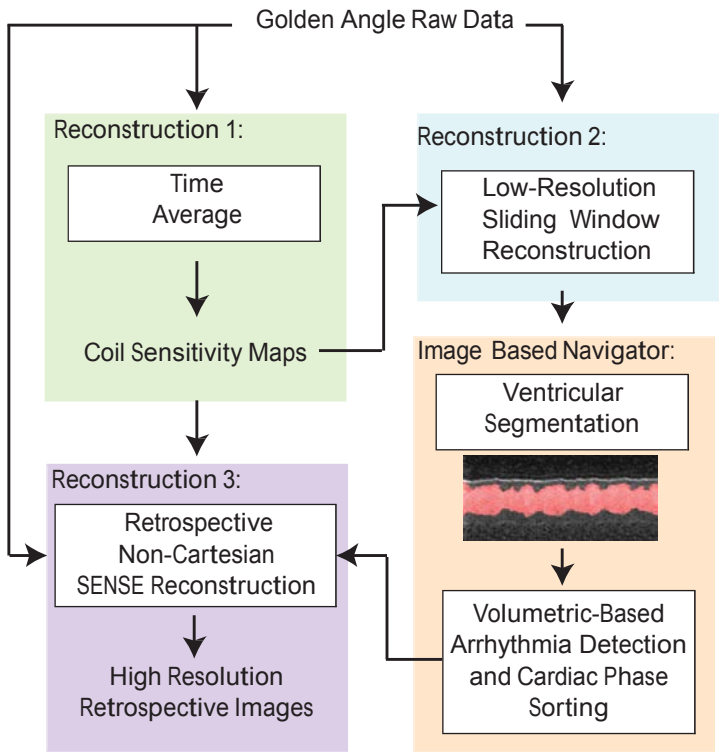

Figure 5.2 Triple retrospective reconstruction method using golden angle radial acquisition. First coil sensitivity maps are generated from the entire golden-angle acquisition. The second reconstruction uses the maps for undersampled, sliding window, SENSE-based reconstruction. LV slice volume is obtained by segmenting the high frame rate images and volumetric-based arrhythmia detection and beat morphology categorization is performed. Beats of interest as well as cardiac cycle information (for each radial projection) are generated from the LV slice volume signal. The final reconstruction combines projections acquired during similar beats and uses assigned cardiac phase information to perform retrospective non-Cartesian reconstruction. Adapted from (81).

Golden angle radial k-space sampling was essential to permit retrospective reconstruction at different spatiotemporal resolutions and ensure highly uniform azimuthal sampling density (82).

In the first reconstruction, for each RF detector, high signal-to-noise images were reconstructed from the entire set of acquired radial views by non-uniform fast Fourier

transform with an optimized Kaiser-Bessel gridding kernel (83,84). RF detector sensitivity profiles were then estimated from these images (50). The detector sensitivity profiles served as inputs for the second image reconstruction.

In the second reconstruction, an image-based navigator was estimated from low spatial resolution, real-time motion images that were produced using a Tikhonov-regularized, non-Cartesian SENSE algorithm (45) with radial projections N_θ = 34, temporal footprint = TR* N_θ = 95.2 ms, frame rate FR = TR (sliding window factor = 1). These parameters were previously found to be sufficient to estimate continuous LV volume up to a HR = 120 beats-per-minute (bpm) (85).

LV slice volume $\mathbb{R}$ was utilized as an image-based cardiac motion navigator, estimated using a level-set segmentation technique (86). First, the images were arranged in a 3D stack of size , where , were the sizes of the image spatial dimensions and was the total number of image frames; the typical size was 128 x 128 x 10,000. Next, binary images were generated using intensity thresh-holding. Segmentation was initialized with a propagation seed centered in the LV. 3D active contour segmentation was performed using region competition with user-defined balloon and curvature forces (87). The advantage of this arrangement was that contours between consecutive image frames were smooth, resulting in temporally consistent and smooth $\boldsymbol{V}$ of size 1. Papillary muscles were automatically excluded from the segmented volume.

The image-based navigator $\boldsymbol{V}$ provided the necessary information for retrospective reconstruction, specifically, categorization of individual beats and labeling of each radial angle to the normalized cardiac phase. The navigator was segmented into individual Beats $\boldsymbol{\mathcal{B}_i} \subset \boldsymbol{V}$, where $\boldsymbol{i} = 1, \ldots, N$, where N is the total number of observed beats. segmentation was performed via a local maxima algorithm, which marked the beginning and end of each beat $\boldsymbol{\mathcal{B}_i}$. An input to the local maxima algorithm was the minimum change in volume $\Delta \boldsymbol{V}$ lying between neighboring minima and maxima. $\Delta \boldsymbol{V}$ was adjusted based on slice volume and was confirmed by visual observation of real-time images to assure detection of ectopic contractions, when present. For each beat $\boldsymbol{\mathcal{B}_i}$, cardiac phase values within the beat $\boldsymbol{\mathcal{B}_i}(t = 0, 100\%$ were assigned to each radial projection.

To normalize cardiac phase, nonlinear temporal scaling of each beat was performed (88). After cardiac phase determination, repeatedly observed beat morphologies $\boldsymbol{\mathcal{M}_i} \subset \boldsymbol{V}$ where $\boldsymbol{i} = 1, \ldots, M$, where M is the total number of unique beats, were determined by calculating 4 parameters for each beat $\boldsymbol{\mathcal{B}_i}$: the beat duration $\boldsymbol{RR_i}$, initial slice volume $\boldsymbol{IS\mathcal{B}_i}$, minimum slice volume $\boldsymbol{M\mathcal{B}_i}$, and final slice volume $\boldsymbol{FS\mathcal{B}_i}$. These 4 parameters were used to detect the occurrence of ectopic contractions, changes in loading conditions, or undesired respiratory motion. When an ectopic contraction was found to disrupt diastolic filling of a cardiac cycle, the systolic duration of the normal contraction was estimated as the time between $\boldsymbol{IS\mathcal{B}_i}$ and $\boldsymbol{M\mathcal{B}_i}$ and used to estimate heart rate duration and re-assign cardiac phase information to projections acquired prior to the ectopic contraction.

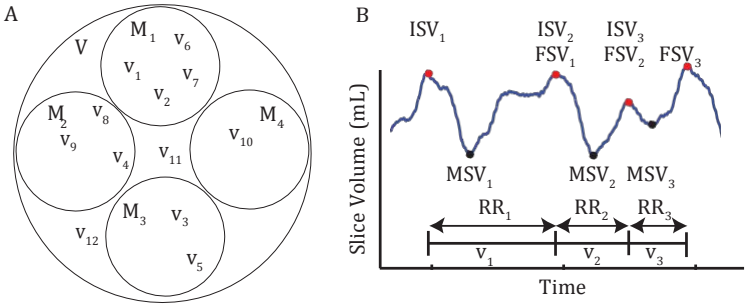

Figure 5.3. Segmentation of an image-based navigator $\boldsymbol{V}$ for retrospective reconstruction of multiple beat morphologies. **A** The image-based navigator $\boldsymbol{V}$ was segmented into individual beats $\boldsymbol{v_i}$. Beat morphologies $\boldsymbol{M_j}$ were generated from beats with similar parameter values. For example, $\boldsymbol{v_3}$ and $\boldsymbol{v_5}$ belong to the same type of beat morphology $\boldsymbol{M_3}$, $\boldsymbol{v_{10}}$ does not belong to any particular beat morphology and thus would be discarded. **B** Local maximum (red points) were detected and utilized to identify individual beats (labeled $\boldsymbol{v_1}$, $\boldsymbol{v_2}$, $\boldsymbol{v_3}$). For each beat, temporal and volumetric measurements were generated to identify observed beat morphologies $\boldsymbol{M_j}$. The beat duration $\boldsymbol{RR_i}$, initial slice volume $\boldsymbol{ISV_i}$, minimum slice volume $\boldsymbol{MSV_i}$, and final slice volume $\boldsymbol{FSV_i}$ for the three beats illustrated are shown. There are three beat morphologies observed (a normal contraction $\boldsymbol{M_1}$, a normal contraction interrupted by a ectopic beat during diastole $\boldsymbol{M_2}$, and an ectopic contraction $\boldsymbol{M_3}$). The three morphologies can be differentiated from one another combined, if repeated, using the parameters shown. Adapted from (81).

Figure 5.3 shows an example of an image-based navigator $\boldsymbol{V}$ segmented into 3 unique beats (labeled $\boldsymbol{v_1}$, $\boldsymbol{v_2}$, $\boldsymbol{v_3}$) and labeled with the 4 navigator-derived parameters $\boldsymbol{RR_i}$, $\boldsymbol{ISV_i}$, $\boldsymbol{MSV_i}$, and $\boldsymbol{FSV_i}$. The three beats corresponded to three different morphologies $\boldsymbol{M_1}$, $\boldsymbol{M_2}$, and $\boldsymbol{M_3}$ ($\boldsymbol{M_1}$: normal contraction, $\boldsymbol{M_2}$: normal contraction interrupted by an ectopic beat during diastole, $\boldsymbol{M_3}$: ectopic contraction). The three morphologies were differentiated from one another using the parameters described. Specifically, $\boldsymbol{M_1}$ was characterized by a long $\boldsymbol{RR}$, high $\boldsymbol{ISV}$, high $\boldsymbol{FSV}$ and low $\boldsymbol{MSV}$ while $\boldsymbol{M_2}$ by a short $\boldsymbol{RR}$,

high $\boldsymbol{IS}$$\boldsymbol{\diamond\diamond}$, low $\boldsymbol{FSV}$ and low $\boldsymbol{M}$$\boldsymbol{\diamond\diamond}$$\boldsymbol{V}$ and $\boldsymbol{\diamond\diamond_3}$ by a short $\boldsymbol{R}$$\boldsymbol{\diamond\diamond}$, low $\boldsymbol{IS}$$\boldsymbol{\diamond\diamond}$, high $\boldsymbol{FS}$$\boldsymbol{\diamond\diamond}$, and high

M****. Assignment of individual beats to a particular morphology was based on similar parameter values that were controlled via tunable tolerances.

The navigator V obtained from a volunteer is shown in Figure 5.4A. Radial projections from accepted beats were sorted by assigned cardiac phase. The small variation in observed navigator values confirms a single beat morphology. The overlapping volume curves as well as the range of observed volume values during the breathhold are shown in Figure 5.4 (B and C).

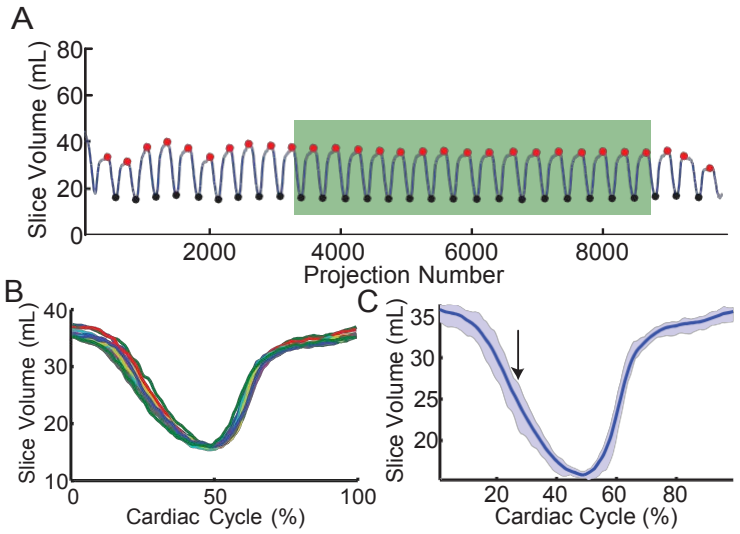

Figure 5.4 Image-based navigator V and beat selection in a normal volunteer in sinus rhytm. **A** V illustrates the effects of respiratory motion prior to the breathhold (projection number 3,500-8,500). A single beat morphology was observed and beats accepted for retrospective reconstruction are labeled with the green box. **B** Comparison of individual beat curves Φ_i illustrate the close agreement of the navigator signal and confirm a single beat morphology. **C** The variation within the beat morphology is small throughout the cardiac cycle (solid line represents the mean of the accepted beats and the shaded areas represent the range). The maximum variation (5.6 mL) occurred at 27% of the cardiac cycle (arrow). The minimum variation (0.8 mL) and variation observed at end-diastole (2.2 mL) provide feedback regarding beat morphologies and breathhold compliance. Adapted from (81).

Final images were reconstructed by binning the sorted readouts. To match typical cine temporal resolution, 30 images were reconstructed for each beat morphology; retrospective sorting resulted in at least 100 radial spokes being binned into each image frame during a typical breathhold in sinus rhythm. As a result, minimal streaking/undersampling artifacts were observed using the iterative SENSE reconstruction.

5.3.4: Quantitative Analysis of Image Quality:

Image quality for the proposed technique and standard cine images was quantified using image contrast and edge sharpness (89). Image contrast C at end-diastole was quantified via $C = SI_{myo} - SI_{blood}$, where SI_{blood} is the mean intensity of a circular region of interest (ROI) in the LV blood pool and SI_{myo} is the mean intensity of a similarly sized ROI in the LV septal myocardium. The edge sharpness ES for each image in the cardiac cycle was calculated via $ES = \max(|d_1|, |d_2|)$, where d_1 d_2 is the intensity gradient in the radial direction perpendicular to the mid-septal myocardium border. The mean and standard deviation throughout the cardiac cycle was compared among reconstruction approaches.

5.3.5: Statistical Analysis

A two-tailed paired Student's t-test ($p < 0.05$) was used to detect significant differences in image contrast. Two-tailed Welch's t-test ($p<0.05$) was used to detect significant differences in image sharpness between the standard retrospective cine and proposed reconstruction approach to account for the difference in variances. For patients with

rhythm disturbances, a two-tailed paired Student's t-test ($p<0.05$) was used to detect significant differences in image sharpness over the cardiac cycle between the acquired retrospective cine and the proposed reconstruction approach.

5.4: Results

5.4.1: Evaluation of beat volume v_i variation in normal subjects

To combine k-space data from multiple heartbeat morphologies, it was necessary for each type of observed rhythm morphology to be spatially consistent. We reasoned that an acceptable level of consistency would be on the order of the beat-to-beat variation of cardiac motion in sinus rhythm during breath-holding. Since multi-shot cine MRI combines data from multiple normal beats, the normal beat-to-beat motion variation must be sufficiently low as to produce images of acceptable quality. Therefore, we used real-time MRI to obtain images of beat-to-beat cardiac motion, quantified continuous LV volume (Figure 5.4A), and then determined the motion consistency of each cardiac phase (Figure 5.4B). Among the normal volunteers (N = 3) in sinus rhythm, 16-18 heartbeats were collected in a single breath-hold with a mean RR-interval = 877 ± 40 ms (heart rate HR = 68.5 ± 3.2 bpm). The maximum difference in slice volume at each cardiac phase from the multiple beats was measured and the variation in measured slice volume σ was determined by the taking the fraction relative to the mean slice volume observed at each cardiac phase. At 3 slice locations per subject (total slices = 9), we observed σ_{EDV} = 6.1% ± 1.6%. In the normal subject shown, the maximum variation $\sigma_{V,MAX}$ = 22.3% was observed at 27% of the cardiac cycle (Figure 5.4C, arrow).

Although the beat-to-beat variation can be sufficiently low to produce Cartesian cine images of acceptable quality, radial sampling may be more sensitive to beat-to-beat variations because the k-space center is repeatedly sampled at each heartbeat for differences in image acquisition. To evaluate the image quality of radial sampling, 30 phases were reconstructed to match the temporal resolution of standard CINE images. The results are shown in Figure 5.5. The figure illustrates image quality and spatial resolution that approximates that of the standard retrospective cine. The variation in measured slice volume for selected beats is shown (Figure 5.5B). In addition to quantifying the variability in maximum slice volume (Phase 1), we can observe that the variation is small throughout the cardiac cycle.

Quantification of blood-myocardium contrast C and edge sharpness E[illegible] are shown

in

Table 5-1.There was no significant difference in blood-myocardium contrast (p=0.30) between standard cine (3.91 ± 0.65) and the proposed reconstruction approach (3.76 ± 1.23) in the 3 subjects in sinus rhythm (N=9). Similarly, E[illegible] showed no

significant

difference (p=0.56) between standard CINE images (0.11 ± 0.02 mm^{-1}) and the proposed reconstruction approach (0.10 ± 0.02 mm^{-1}).

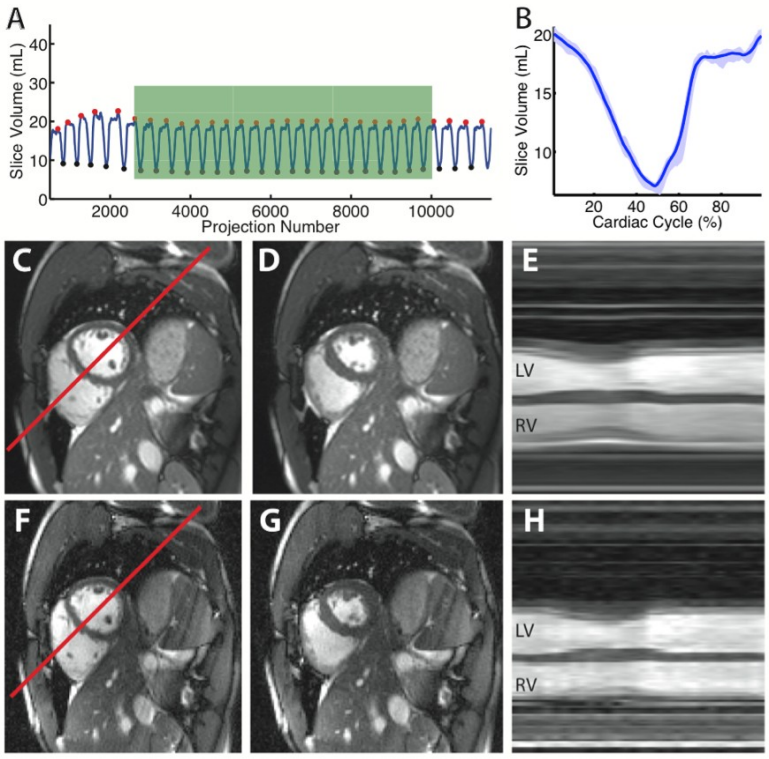

Figure 5.5 Cardiac motion consistency from a single subject in sinus rhythm **A** Volume over time during the imaging experiment. Beats accepted for retrospective reconstruction are labeled with the green box. **B** The variation in slice volume is small throughout the cardiac cycle (solid line represents the mean of the curves in A and the shaded areas represent the range). **C** End-diastole and **D** End-systole from a standard Cartesian acquisition. **E** Projection through the LV demonstrates cardiac motion. **F** Comparable images using the proposed method illustrate end-diastole, **G** end-systole, and **H** temporal motion Adapted from (81).

	Sinus Rhythm (N=3)		Bigeminy (N=1)		Frequent PVCs (N=1)	
	CINE	Proposed Approach	CINE	Proposed Approach	CINE	Proposed Approach
Image Contrast	3.91 ± 0.65	3.76 ± 1.23	2.36	4.62 3.29	2.21	2.93
Endocardial Sharpness - mm^{-1}	0.11 ± 0.02	0.10 ± 0.02	0.10 ± 0.02	0.12 ± 0.03 0.15 ± 0.03	0.05 ± 0.01	0.10 ± 0.02

Table 5-1 Comparison of quantitative image quality in sinus and arrhythmia subjects. During sinus rhythm, the proposed reconstruction provides comparable endocardial sharpness and image contrast. In subjects with rhythm disturbances, the proposed algorithm results in an increase in image contrast as well as a statistically significant increase in edge sharpness. Adapted from (81).

5.4.2: Reconstruction of beat morphologies during rhythm disturbances

Imaging was performed in two subjects with rhythm disturbances. In a subject with irregular bigeminy, two different beat morphologies were repeatedly observed. The other subject had PVCs and in the setting of PVCs, the method provided improved arrhythmia rejection. In both cases, high spatial and temporal resolution image sets were generated which were void of corruptions observed in standard clinical images.

The results obtained in a subject with irregular bigeminy are shown in Figure 5.6. During irregular bigeminy, two beat morphologjes were observed: 1) an uninterrupted cardiac cycle (similar to sinus rhythm) and 2) a cardiac cycle that is interrupted during diastole (resulting in a W-shaped volume curve). The self-gated volume signal, derived from low-resolution MRI data, exhibited both types of heartbeats. Repetitions of the morphologies were combined to provide high spatial and temporal images of each beat morphology.

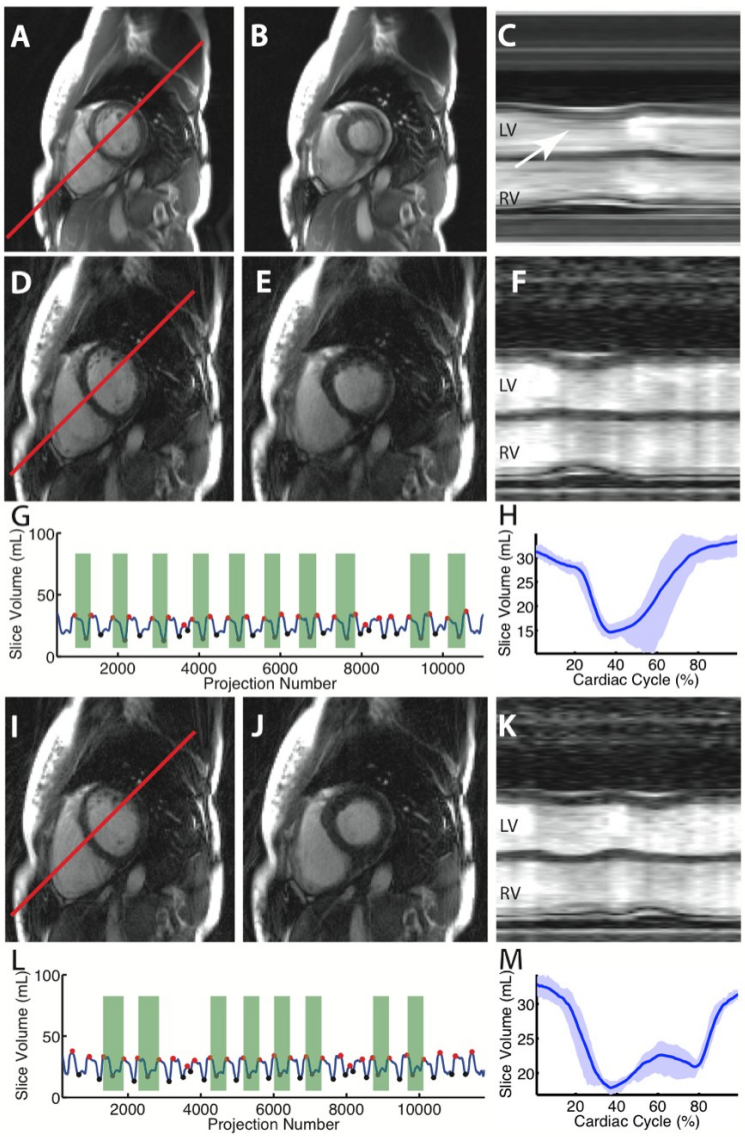

Figure 5.6 Results obtained from a subject in irregular bigeminy. **A** End-diastole, **B** end-systole, and **C** projection through the LV of a scan corrupted by combination of two beat morphologies. Blurring of endocardial motion is shown by the white arrow. The proposed method allows for two beat morphologies to be reconstructed separately. The uninterrupted beat is shown in **D-H** while the beat interrupted during diastolic filling is shown in **I-M.** Both were generated from a breathheld acquisition. **F** and **K** illustrate the differences in endocardial motion, which corresponds to the measured slice volume. **G** and **L** demonstrate how desired beats can be selected from a single breathheld scan. Specifically, for this arrhythmia, separation of the morphologies was achieved using beat duration RR, initial I[illegible], minimum M[illegible], and final FSV slice volume. Adapted

from (81).

Blood-myocardium contrast C increased from the standard cine (2.36) to the proposed reconstruction approach (4.62 and 3.29, respectively). Quantification of edge sharpness $E$$$ showed an improvement between standard CINE images (0.10 ± 0.02 mm^{-1}) and the two beats reconstructed using the proposed reconstruction approach (0.12 ± 0.03 mm^{-1} and 0.15 ± 0.03 mm^{-1}). In the uninterrupted beat, the increase in sharpness was not statistically significant (p=0.09), but in the interrupted beat, the increase in sharpness was highly significant p<0.0001).

In addition to reconstruction of separate beat morphologies, use of the slice volume curve as a gating signal allows for improved reconstruction of data in subjects with irregular ectopic beats. In a subject with frequent PVCs, the rhythm disturbances do not result in a repeating pattern as the PVCs occurred at different points during diastole. The volume curve allows for visualization of the maximum and minimum slice volume and this information can be utilized to estimate beat duration and appropriately scale data acquired prior to the ectopic beat. This allows for improved scan efficiency and results in variable sampling density during the reconstructed images (shown in Figure 5.7).

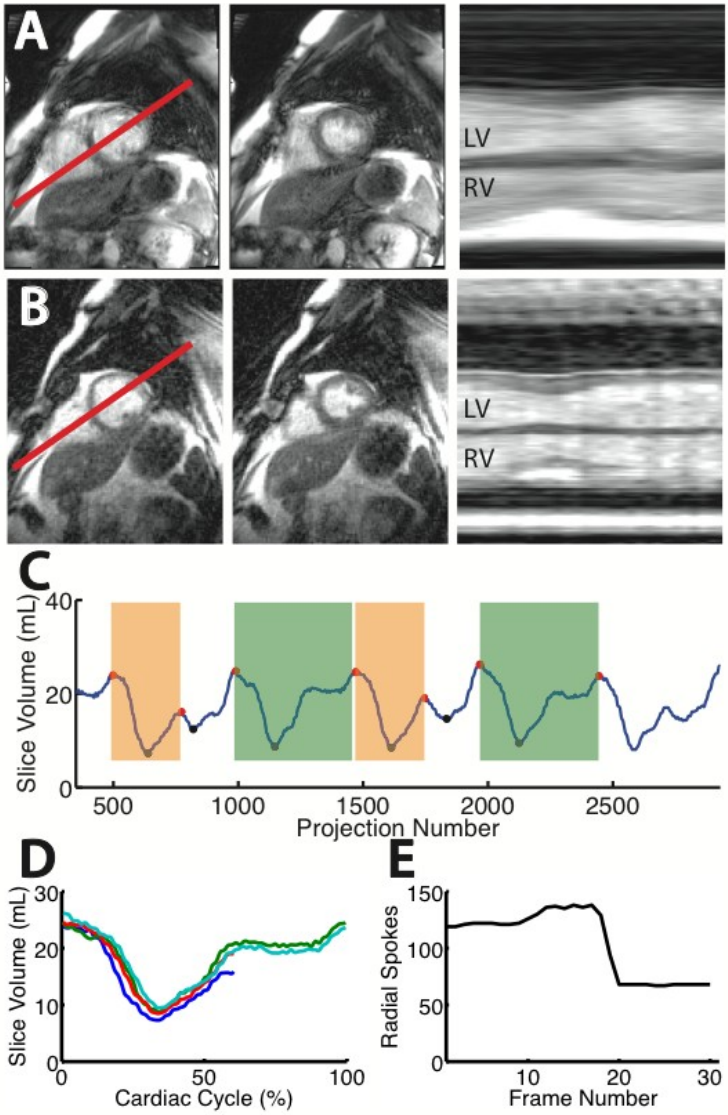

Figure 5.7 Retrospective reconstruction of a subject with frequent irregular PVC. **A** Standard cine imaging is corrupted by frequent premature ventricular contractions. **B** Proposed method allows for reconstruction of images free from corruption. **C** Volume curve demonstrates the occurrence of PVCs which can be excluded from reconstruction. Two uninterrupted beats are selected (green boxes) Additional data can be introduced from timepoints prior to PVC (orange boxes). This further improves image quality. **D** The overlapping volumes illustrate correct timing even for periods interrupted by PVCs. **E** Based on the occurrence of the PVC in diastole, sampling density will vary among the image frames. Sampling is higher for the end-diastolic frames since PVCs interrupted diastolic filling. Adapted from (81).

Once again, blood-myocardium contrast C increased between standard cine (2.21) and the proposed reconstruction approach (2.93). Edge sharpness $E$$$ showed a statistically

significant ($p < 0.0001$) improvement between corrupted standard CINE images (0.05 ± 0.01 mm^{-1}) and the images reconstructed using the proposed reconstruction approach (0.10 ± 0.02 mm^{-1}).

5.5: Discussion

We developed an MRI method to reconstruct images of multiple heartbeat morphologies at high spatiotemporal resolution in subjects with arrhythmias. These subjects have non-periodic cardiac motion and cine MRI is usually corrupted by motion artifacts. Even when arrhythmia rejection is used to eliminate ectopic beats from data reconstruction, these images can have low quality because of inconsistent R-wave detection or beat-to-beat variations in preload. The triple radial reconstruction allows for observation of each cardiac cycle including rhythm disturbances. The slice volume curve from high temporal resolution radial MR data can be used to detect different beats and categorize beats into various morphologies. This allows for better filtering of beat data so that only consistent data are combined during high spatiotemporal resolution image reconstruction.

In the presence of arrhythmias, ECG data appears to be a poor physiologic signal to guide cine retrospective reconstruction. We observed decreases in quantitative measures of image quality; C decreased from 3.91 ± 0.65 to 2.36 and 2.21 in the

presence of irregular bigeminy and frequent PVCs respectively. Similarly, $E_{\theta\theta}$ decreased

from 0.11 ± 0.02 mm^{-1} in sinus rhythm images to 0.05 ± 0.01 mm^{-1} in the presence of

PVCs. The image-based slice volume navigator allowed for the precise identification of normal and ectopic systolic and diastolic periods, and preload conditions. This allowed for improvements in image contrast and edge sharpness as well as more efficient scanning with less discarded data. Even in the setting of rhythm disturbances that interrupt diastole, the identification of end-systole (slice volume minimum) allowed for an estimation of the expected RR interval, phase resorting of the data, and increased sampling density prior to the rhythm disturbances as shown in Figure 5.6.

This method permitted functional differences between normal, ectopic, and post-ectopic contractions to be observed and this may have important clinical relevance. Since ectopic contractions affect both filling time and preload for subsequent cardiac contractions, post-ectopic contractions can be very different from beats prior to the ectopic beat. This information may be important for determination of the subject's overall cardiovascular function. Parameters such as ejection fraction or stroke volume could be defined for each type of morphology, normal, ectopic, or post-ectopic, and, when combined with information about the frequency of occurrence of that morphology, provide more detailed information about the subject's cardiac function.

The triple reconstruction approach shares some common features with other published non-Cartesian reconstruction methods. Hansen, et al. recently presented a method for retrospective reconstruction of free-breathing cine MRI data using multiple reconstructions of golden angle radial data, obtaining image-based signals of cardiac and respiratory motion and coil sensitivity maps (90). Instead of using image-based navigators for respiratory motion correction, our approach used the navigator to derive

an estimate of ectopy, which can then inform the following reconstruction about cardiac motion consistency during an arrhythmia. Furthermore, it may be reasonable to obtain all three types of data (beat morphology, cardiac phase, and respiratory motion) in a single free-breathing examination. However, there are complicated relationships between thoracic pressure (during free-breathing or breath-holding), LV pressure and the ectopy occurrence and it is not entirely clear how these variables would affect image reconstruction. Altogether, these applications demonstrate the flexibility and advantageous sampling properties of radial k-space sampling compared to Cartesian cine MRI.

In retrospective cine MRI, the breath-hold duration is determined by the subject heart rate and scan parameters, such as the TR, phase encodes per shot (segment size) and total number of phase encodes. If the subject is unable to complete the breath-hold, substantial respiratory motion corrupts the image series. Analysis of the LV volume from image-based navigators can be used to identify the breath-hold period and any number of heartbeats can be used for retrospective reconstruction. In situations where breath-holds may not be achievable or desired, this approach should allow for reconstruction of high spatial and temporal resolution images via retrospective respiratory phase sorting. The efficiency of this approach would depend on several factors including the rate and depth of respiratory motion as well as the desired acceptance window.

In addition to retrospective cine MRI, real-time acquisitions, driven by recent advances in multi-detector (parallel) signal detection, non-Cartesian sampling or compressed sensing reconstruction, may improve visualization of arrhythmias by providing potentially high

spatiotemporal resolution scenes of every heartbeat with much less data than would be required by the Nyquist sampling criteria. Real-time MRI is ultimately limited by scanner hardware limits and safety tolerances of the human body to MR electromagnetic fields; therefore multi-beat sampling approaches will probably remain important for many applications, especially in 3D. Improvements in real-time MR are also an opportunity to enhance determination of cardiac phase or ectopy through self-gated images in the retrospective reconstruction. Triple reconstruction combines the strengths of real-time, high temporal resolution capture of inconsistent beat-to-beat cardiac motion, and retrospective cine MRI, further enhancing spatiotemporal resolution and beat categorization.

Although the proposed method outlines the use of slice volume, other descriptive signals obtained concurrently with the acquisition or derived from real-time images can be used as a navigator to guide reconstruction. Specifically, for long-axis imaging, slice segmentation may prove more challenging than other attainable signals, since the automatic segmentation approach was not refined to prevent inclusion of the LV outflow tract or left atrium. However, with an appropriate physiologic signal, we expect the triple reconstruction approach will result in high quality images.

One limitation of this approach is the reduction of k-space sampling uniformity that occurs with multi-shot golden angle radial trajectories. Although consecutive, single-shot golden angle radial projections provide near-uniform sampling, retrospective sorting of potentially non-consecutive beats results in sampling patterns that have reduced uniformity. However, combined with the powerful anti-aliasing properties of radial

imaging, the increased number of projections associated with retrospective sorting decreases undersampling and generally improves image quality.

5.6: Conclusions

We developed a reconstruction method for retrospective cine MRI that permitted high spatiotemporal resolution imaging of distinct beat morphologies. The feasibility of this approach proved valid in normal subjects and was further demonstrated in a subject with arrhythmic, pre-ventricular contractions and in another subject in bigeminy. This approach may be very useful in arrhythmia subjects to reduce non-diagnostic cine MRI with arrhythmia rejection or to integrate ectopic beat function to better understand cardiac function in arrhythmia.

Chapter 6: Continuous Adaptive Radial Sampling of K-Space From Real-Time Physiologic Feedback

6.1: Abstract

A limitation of the multi-shot approach outlined in Chapter 5 is that the k-space sampled obtained from multiple shots are no longer uniformly spaced. This limits the potential improvement in 'streaking' artifacts using the technique. Furthermore, advanced processing of physiologic information (such as an LV pressure waveform or ECG) may allow for multi-shot, multi-slice imaging during dynamic studies.

With those goals in mind, we proposed an adaptive real-time radial k-space sampling trajectory (ARKS) to respond to a physiologic feedback signal and ensure sampling consistent motion states while improving sampling uniformity in single- and multi-shot approaches. In this adaptive k-space sampling strategy, the most recent signals from an ECG waveform were continuously matched to the previous signal history. New radial k-space locations for sampling were determined based on the location of data acquired during previous sampling of the same motion state. These MR signals were combined using multi-shot or single-shot radial acquisition schemes. Simulations were performed on ECG data from 10 normal subjects and 2 patients and were compared to random radial sampling and golden angle sampling trajectories. Metrics of sampling uniformity showed near ideal sampling properties for the proposed sampling scheme. Implementation of the approach allowed for initial in vivo results.

6.2: Introduction

Dynamic scenes pose various challenges to magnetic resonance imaging (MRI) that limit spatial and temporal resolution. If the scene is periodic, like the motion of the heart, it is common in MRI to combine data from multiple periods to improve image quality (91). A problem is that, for a number of cardiac MRI applications, including stress testing (92), arrhythmias, and measurement of pressure-volume relationships (85), there can be significant motion artifacts or contrast variation as a result of inconsistent data between heartbeats, limiting the total amount of acquired data.

The main problem with multiple beat acquisitions is that the human heart exhibits only quasi-periodic motion, so it is not guaranteed that the heart will be in the same position. In general, the RR interval exhibits normal fluctuations (93,94) that depend on a host of sympathetic and parasympathetic systems, usually decreases during breath-hold examinations, and the relative diastolic and systolic periods do not change linearly with heart rate. If an arrhythmia occurs, then not only is the heart rate variable, but also the loading conditions and contractile state of the heart may vary. This inconsistent motion can result in artifacts and reduced spatial and temporal resolution.

Respiratory motion is an additional problem affecting segmented data acquisitions. Many clinical exams use breath-held examinations or motion-detecting scans to reduce respiratory motion artifacts, but if the breath-held scan time exceeds the patient's endurance, then inconsistent position data can lead to artifacts or reduced spatial resolution. The efficiency of a navigator examination partly determines the overall scan

time. If the range of accepted motions of the diaphragm is increased to improve scan efficiency, then the position of the heart and lungs may be inconsistent.

It is desirable to reduce some of the artifacts associated with motion by adapting the acquisition dynamically in response to changes in physiology. To some extent, adaptive sampling already is used in most cardiac examinations. In MRI, data is sampled in the multidimensional Fourier domain, called k-space. Typically, in clinical cardiac cine examinations, new k-space data is acquired when an R-wave is detected, permitting complete acquisition of k-space in several heartbeats (41). In most cardiac cine exams, the transition from one part of k-space to the next occurs within a few milliseconds after detection of the R-wave. Another example of adaptive k-space sampling is when, during an arrhythmia, data is rejected if the RR interval falls outside of a previously specified range. The decision to reject and reacquire data occurs within a few milliseconds. In both retro- and prospectively-gated examinations, with or without arrhythmia rejection, the sampling trajectory updates occur infrequently, once every heartbeat. As a result, they are not well designed to respond correctly or quickly, if at all, to more complex signals, such as heart rate variations, arrhythmias, dynamic challenges or contrast changes and result in inconsistent motion and artifacts (Figure 6.1).

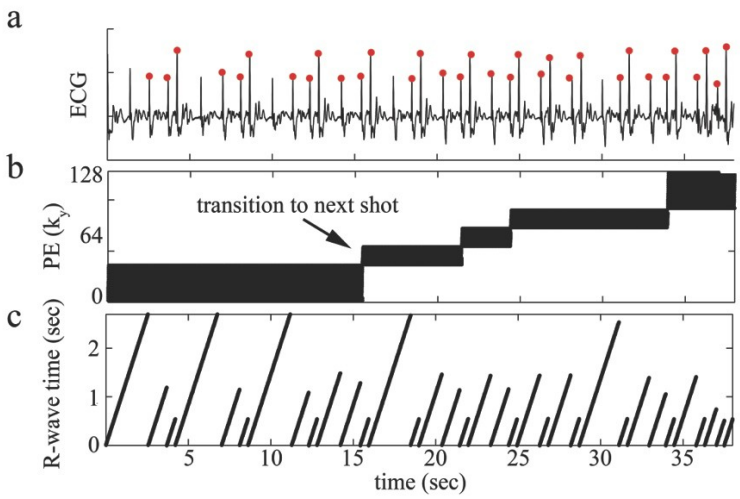

Figure 6.1 Acquisition of retrospective cine MRI k-space data during a severe arrhythmia and using arrhythmia rejection. **a** ECG data is continuously acquired and R-waves (red) are detected. **b** After each detected R-wave, N_{k_y} segments of k-space are collected until, after a number of periods, all 128 k_y phase encodes (PE) are collected. For a normal subject in sinus rhythm, the transition from one N_{k_y} to the next occurs after each R-wave is detected. For this patient with a severe arrhythmia, the inconsistent RR-interval causes these N_{k_y} data to be rejected and reacquired during the subsequent, detected RR-interval. This causes motion artifacts since the beat-to-beat data is inconsistent. **c** a plot of the time from the last detected R-wave to the next clearly shows that the acquisition time is not consistent. Adapted from (95).

We propose a method for continuously adapting the MRI acquisition in response to a real-time physiologic feedback signal (Adaptive Real-time K-space Sampling = ARKS). In this method, the most recent signal is continuously compared to its history and data obtained from previous periods are used to determine how subsequent data is acquired. We hypothesized that the acquisition would have near-optimal sampling properties (uniform sampling density) for all time periods and adapt well in response to arrhythmias. The theoretical basis of the sampling trajectory is shown and simulated results are presented as a proof-of-principal. Initial implementation and scanning of a normal volunteer are shown as proof-of-principle. We compare the results of ARKS sampling to

conventional radial sampling methods, including uniform, random and golden angle strategies.

6.3: Method

6.3.1: MRI Radial K-space Sampling in ARKS

As described in 2.1, the measured signal s is related to the object water ^{1}H spin density m by the Fourier transform

$$s(k_i) = \int_{\Re^2} m(\vec{r}) e^{-i2\pi \vec{k}_i \vec{r}} \, d\vec{r} \qquad [6\text{-}1]$$

where the object is spatially-encoded at k-space locations k_i

$$k = \gamma \int_{\tau}^{t-\tau} G(t) dt \qquad [6\text{-}2]$$

which are dependent on the magnetic field gradients, $G = \left[\frac{\partial B_z}{\partial x}, \frac{\partial B_z}{\partial y}, \frac{\partial B_z}{\partial z} \right]$

Modulation of the magnetic field gradient coil amplitudes G permits sampling of the multidimensional Fourier domain (k-space). For satisfactory reconstruction of m, it is important to sample signals uniformly throughout k-space.

One practical method is to acquire data along multiple radial projections, as described in 2.1 and Chapter 4. The radial data is obtained by switching the magnetic field gradients each pulse sequence repetition time (TR).

As will be seen further, in ARKS, a physiologic signal, such as the ECG waveform from a patient, is measured. This ECG waveform is continuously analyzed and compared to its previous history. Together, the ECG signal history, as well as the most recent sample, are used to determine the next polar sampling angle in k-space. Once this angle is determined, the magnetic field gradients G are updated (Figure 6.2). This is different from other sampling strategies in that (1) the polar sampling angle is not found via a pre-determined schedule and (2) the polar sampling angle is updated much more often than once each cycle of the physiological signal. For the balanced steady-state free-precession MRI sequence shown in Figure 6.2, the polar sampling angle could be updated as often as every few milliseconds. The continuous determination of the polar angle from physiologic data potentially allows the k-space trajectory to respond rapidly to changes in physiology in ways that traditional radial sampling would not allow.

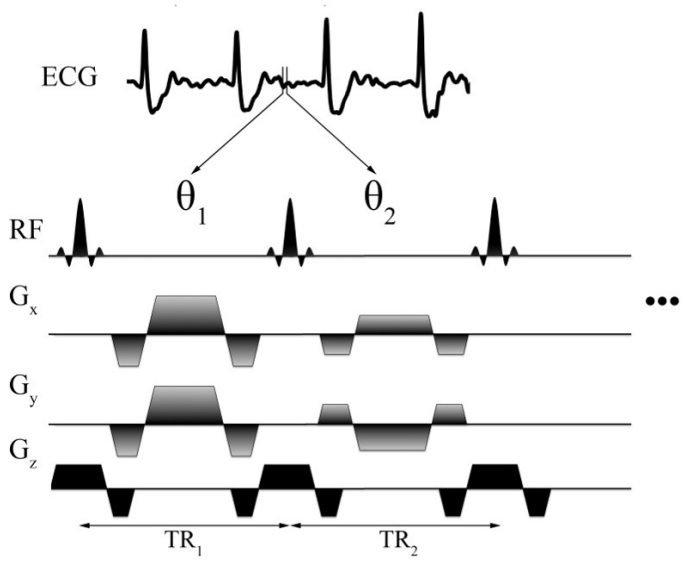

Figure 6.2 A pulse sequence for adaptive radial sampling of k-space from an ECG signal. A physiologic signal, e.g. ECG data, is continuously acquired and compared to its previous history. Instructions to acquire a new radial projection $\theta = \tan^{-1}(G_y / G_x)$ are sent from the physiologic signal analysis routine to the measurement controller of the MRI scanner in real-time. RF = radiofrequency pulses, $G_x = \partial B_z / x$ the orthogonal components of the magnetic field gradients, TR = repetition time. Adapted from (95).

For radial sampling with uniformly-spaced projections, the number of projections N_θ required to fulfill Nyquist sampling and prevent aliasing of the Fourier signal is given by

$$N_{\theta,Nyquist} = \pi N_R / 2 \qquad [3\text{-}15]$$

where N_R is the number of samples per projection. The spacing between projections is not uniform in ARKS and therefore it is not guaranteed that the Nyquist sampling criteria is met for all regions of k-space. Even when the number of projections N_θ exceeds $N_{\theta,Nyquist}$, these projections are not uniformly distributed, so there may be some polar

angles that do not satisfy the Nyquist sampling criterion (Figure 6.3). Unlike Cartesian k-space sampling, it is usually possible to reconstruct useful images with $N_\theta < N_{\theta,Nyquist}$ since radial sampling has different signal aliasing properties (96). In the next section, it is discussed how the selection of the polar angle is determined to satisfy the Nyquist criteria for all image frames in ARKS.

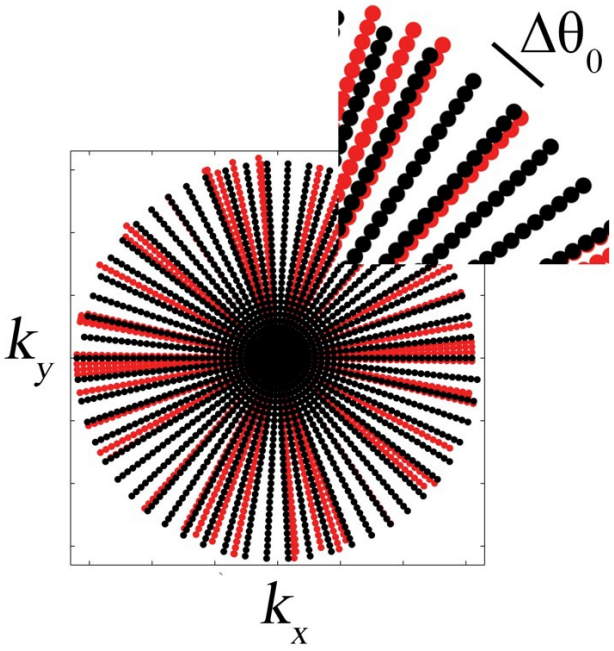

Figure 6.3 Comparison of uniform and radial sampling uniformity in k-space. a, uniform (black) and random (red) radial sampling. Nyquist sampling is satisfied if the arc $\Delta\theta_0$ is small, however, with random sampling, there may be some polar angles θ for which $\Delta\theta_0$ does not satisfy Nyquist sampling in the polar dimension. In general, uniform polar sampling is essential to reduce undersampling artifacts and radial streaks. Adapted from (95).

6.3.2: Determination of the Polar Angle θ in ARKS

An implementation of ARKS for radial k-space sampling is shown in Figure 6.4. In Figure 6.4a, the most recent physiologic signal S_s is stored in a small N x 1 buffer in memory.

The size of the buffer is chosen to capture sufficient important features of the signal to match to a previously acquired signal. For an ECG signal, the buffer size is large enough to include data from 1-2 heartbeats. In Figure 6.4b, a signal sampled for a longer period of time S_L containing a previous record of the physiologic data is stored in a M x 1 buffer in memory. The signals S_s and S_L are cross-correlated

$$S_s * S_L[n] = \sum_{m=0}^{M-1} S_s[m] S_L[m+n] \qquad [6\text{-}3]$$

Local maxima are determined from the result of the cross-correlation as shown in Figure 6.4c and correspond to the signals highlighted in red in Figure 6.4b. The lag n of each local maxima is an index to the maximum overlap of the two signals.

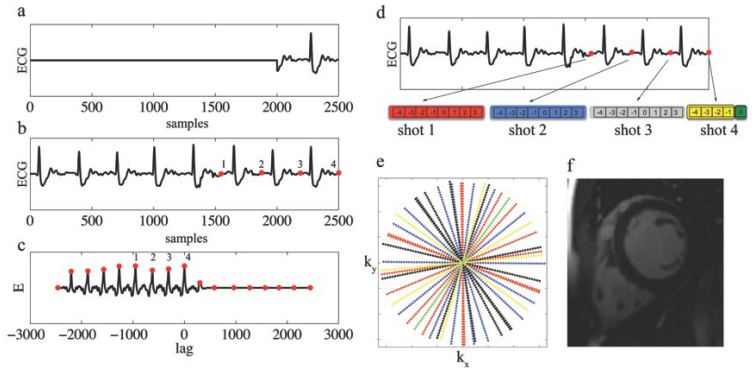

Figure 6.4 Diagram showing how radial projections are adaptively chosen in response to a real-time physiologic signal in ARKS using a 4-8-29 sampling scheme (shots-segments-projections). **a** a signal buffer S_s with the most recent physiologic data (1-2 heart beats). **b** a large buffer S_L storing a previous history of the physiologic signal. 4 similar periods of the cardiac cycle are labeled (red). **c** cross-correlation between buffers S_s and S_L. Local maxima of signal overlap are labeled (red). The negative lags for the first 4 local maxima are used to label the ECG in **b**. **d** For the first 3 shots, 8 radial projections (segments) are acquired and labeled -4 to 3, with the 0 projection corresponding to the lag index in **c**. Only 4 projections are acquired in the last shot and together these 28 projections are used to determine the angle θ of the 29th projection. **e** 29 k-space radial projections. The color of each projection corresponds to the shot index in **d**. **f** simulated reconstructed image for this image frame. Adapted from (95).

Multiple heartbeat k-space trajectories are specified by the number of radial projections (segments) per heartbeat (shot). An example of how segments and shots are defined in ARKS is shown in Figure 6.4d. In the example shown, the number of segments is 8 and the number of shots is 4. The total number of k-space projections per image frame is

$$N_\theta = N_{segments} * N_{shots} - \frac{N_{segments}}{2} + 1 \qquad [6\text{-}4]$$

For this example, the total number of projections would be 29. For each shot, the lag corresponding to the local maxima is the center of the segments of k-space views used. Note that the final shot has less segments than other shots because future segments have not yet been acquired.

From a list of previously acquired projections, the angles corresponding to the identified segments are collated. The list is sorted in ascending order and the angular differences between adjacent radial projections are computed. For all $\theta \in \Re$ on the interval $[0\ 360°)$

$$\Delta\theta_i = \theta_{i+1} - \theta_i \qquad [6\text{-}5]$$

The next projection angle is then chosen such that it bisects the largest $\Delta\theta_i$ from the list. Since each new projection fills in the low data regions of k-space, ARKS provides nearly uniform sampling to the physiology at all times (Figure 6.4e).

6.3.3: Polar angle probability function and cumulative distribution function

To determine the uniformity of ARKS sampling, k-space trajectories were analyzed with a function χ that reports the probability that two adjacent radial projections are separated by a polar angle $\Delta\theta$. χ is a probability distribution

$$\chi = P(\Delta\theta_i = \theta_{i+1} - \theta_i) \qquad [6\text{-}6]$$

where $\Delta\theta$ lies on the interval $(0\ \pi]$. The rationale was that, for an optimal ARKS k-space trajectory, χ would resemble an ideal distribution χ_0 and a plausible way to test its performance would be to compare its distribution χ to the ideal distribution χ_0.

A reasonable function to describe the ideal distribution χ_0 was the Dirac delta function

$$\chi_0 = \delta(\Delta\theta_i - \Delta\theta_0) \qquad [6\text{-}7]$$

where $\Delta\theta_0 = \frac{\pi}{N}$. χ_0 describes the distribution function for uniformly-spaced radial k-space projections and is unity at $\Delta\theta_0$ and 0 elsewhere (Figure 6.5). This distribution is ideal in the sense that k-space is uniformly sampled in the polar dimension θ and would therefore result in an optimal signal-to-noise ratio and artifact level.

An analytical description of χ is possible only for simple k-space trajectories, nevertheless, an approximate distribution, χ_e, can be computed empirically using physiologic data. For this purpose, we used ECG data from normal subjects to

determine the empirical distribution, as described in the next section. In this approximation, a set of angles $S = \Delta\theta_i$ is determined for each image frame. The total number of elements of S is then $N_e = N_\theta N_f$, where N_f is the total number of image frames.

A measurement of uniformity is derived from the cumulative distribution function

$$CDF_i = \frac{1}{A}\sum_{i=0}^{N_e}\Delta\theta_i \qquad [6\text{-}8]$$

where, by definition, the normalization constant A is determined such that

$$\sum_{i=0}^{N_e} CDF_i = 0.5 \qquad [6\text{-}9]$$

The cumulative distribution function is useful in that it provides a simple, quantitative method to compare a polar sampling distribution to the ideal, uniformly spaced distribution. The relationship between approximate and ideal distributions can be expressed as the percent ideal uniformity (related to the Gini coefficient),

$$P = \frac{CDF(\chi_e)}{CDF(\chi_0)} \qquad [6\text{-}10]$$

The percent ideal uniformity was expressed as a fraction of 100%.

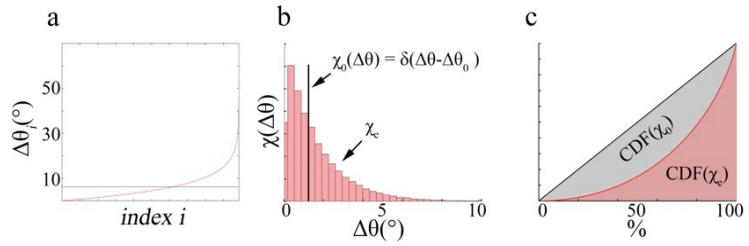

Figure 6.5 Analysis of uniform and random k-space sampling uniformity. **a** graph of sorted angles $\Delta\theta_0$ for uniform (black) and random (red) radial sampling trajectories. **b** Sampling distributions χ for uniform (black = χ_0) and random sampling (red = χ_r). The uniform sampling distribution is a delta function positioned at the $180° / N_\theta$. **c** cumulative distribution functions (CDF) for uniform (black) and random (red) radial sampling trajectories. The percent ideal uniformity P is the relative area of any sampling trajectory CDF to the uniform CDF. Adapted from (95).

6.3.4: Determination of χ_e and $CDF(\chi_e)$

3-lead, chest ECG data was collected from 10 normal subjects at a 400 Hz sampling rate. This data was resampled to the MRI scanner repetition time (TR). The duration of the ECG recordings was 75.7 ± 23.7 sec, corresponding to 2.7 ± 0.85 x 10^4 k-space projections sampled at TR = 2.8 ms. Although MRI data was not collected, it is possible to determine the radial angles that would be chosen from the ECG signal alone.

First, a training period was used to determine an initial array of projections. During the training period, ECG data was collected so that a sufficient number of projections could be used to compute new polar angles in ARKS. The duration of this training period was the time necessary to acquire M k-space projections to fill the large signal buffer S_L for cross-correlation and, during this time, each projection angle was assigned randomly from the interval $[0\,180°)$.

After the training period was complete, the signals were cross-correlated (Equation [6-3]) a list of previously acquired polar angles was sorted and the next angle was determined (Equation [6-5]). This process was repeated until the end of the ECG recording. Then, for the projections belonging to each image frame, the finite difference was determined and the probability distribution χ, cumulative distribution function $CDF(\chi)$ and percent ideal uniformity P were measured. The total number of measurements in the probability distribution χ was $N_e = N_\theta N_f$. These measurements were repeated for the following acquisition schema (shots-segments-projections): 1-128-65, 2-64-97, 4-8-29, 4-16-57, 4-32-117, 4-64-225, and 8-16-121. For comparison, χ, CDF, and P were also measured for two pre-defined k-space trajectories: (1) golden polar angle sampling of k-space (72), in which the polar angle was incremented on a fixed schedule $\theta_{i+1} = \theta_i + 111.25°$ and (2) random polar sampling, in which the polar angle was determined randomly from the interval $[0\,180°)$.

6.3.5: MRI Image Simulations

For simulations, MR image data was obtained from one normal human subject and two patients with arrhythmias. All subjects and patients gave informed consent prior to participating in the study, approved by the Institutional Review Board of the University of Pennsylvania. Image data was acquired on a 1.5 T whole-body MRI system (Avanto; Siemens Healthcare; Erlangen, Germany) equipped with a 40 mT/m gradient coil and a 32 channel RF receiver array (16 anterior and 16 posterior elements). Cardiac gating was obtained with a 3-lead wireless ECG system and logged in real-time. Time-stamps

were communicated using TCP/IP from the pulse sequence to the ECG log file to synchronize image and ECG data. Left ventricular, short-axis, real-time data was obtained using a golden angle radial trajectory and image parameters, flip angle = 70°, TE = 1.4 ms, TR = 2.8 ms, number of frequency encoded points = 128, field-of-view = 340 mm x 340 mm, slice thickness = 8 mm, bandwidth = 1140 Hz/pixel. 10-40 seconds of continuous golden angle radial data was collected, resulting in 6000-20000 golden angle radial projections.

K-space signal data was reconstructed offline using a non-Cartesian SENSE algorithm (48) in open-source software (47) on a Linux workstation. The reconstructed image frame rate was 300 frames per second and exposure time (temporal footprint) was 95 ms (= 34 projections per frame). To remove residual radial streak artifacts, a median filter was applied with a width of 30 frames. The final 128 x 128 images were interpolated to 512 x 512.

Simulated data was created using the MRI signal equation

$$s(k_i) = \sum_{r=0}^{MxN} m(\vec{r}) e^{-i2\pi \vec{k}_i \cdot \vec{r}} d\vec{r} \qquad [6\text{-}11]$$

where s is the encoded k-space signals, N and M are the dimensions of the object (= 512 x 512). The k-space positions k_i were specified by the radial sampling trajectory (random, golden or ARKS projections). Images were reconstructed from the simulated k-space signals using a non-Cartesian SENSE algorithm in open source software, as described above.

6.4: Results

6.4.1: Normal Subjects

The mean heart rate of the 10 normal subjects was 72.2 ± 4.7 bpm. The RR-interval varied from σ_{RR} = 35.5 - 157.3 ms with a median variation of 59.3 ms

For all 10 subjections, the overall ARKS probability distribution χ_e was highly robust to normal ECG variations and could be qualitatively characterized by a superposition of two distributions $\chi_e = \chi_1 + \chi_2$; first, a broad distribution of angles near to the ideal distribution χ_1 , and a second distribution of angles at smaller polar spacing χ_2 (Figure 6.6). χ_1 and χ_2 were present in all normal subjects. The results from a single normal subject are shown in Figure 6.6 Four different sampling schemes with a fixed number of shots, but varying segments and projections, (shots-segments-projections) 4-8-29, 4-16-57, 4-32-113 and 4-64-225, are shown. The distribution was very close in comparison to the ideal distribution angle $\chi_0 = 6.2°$, $\chi_{1,4-8-29,\max} = 7.8 \pm 0.1°$.

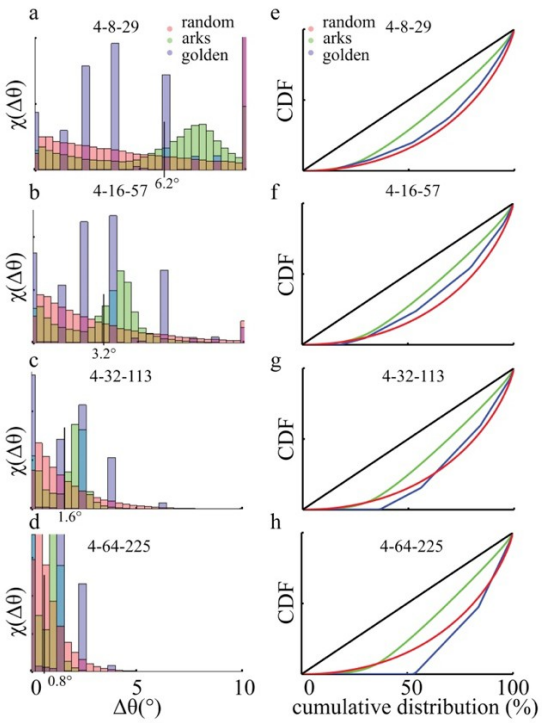

Figure 6.6 Probability distributions X_e (**a** - **d**) and cumulative distribution functions (**e** - **h**) for 4 different sampling schemes (**a** and **e**, 4-8-29), (**b** and **f**, 4-16-57), (**c** and **g**, 4-32-113) and (**d** and **h**, 4-64-225) and 3 radial sampling trajectories (random, arks, and golden angle sampling). The ideal distribution is labeled (black line) and angle shown. Adapted from (95).

The results for other sampling schemes were consistent and are shown in Table 6-1. The cumulative probability distributions CDF for random and golden angle radial sampling schemes are also shown in Figure 6.6 e-h.

	Sampling Scheme (shots-segments-projections)				
	1-128-65*	4-8-29	4-16-57	4-32-113	4-64-225
Ideal, $\Delta\theta_{1,1}$	2.8°	6.2°	3.2°	1.6°	0.8°
ARKS, $\Delta\theta_{1,1}$	2.7 ± 0.1°	7.8 ± 0.1°	4.2 ± 0.2°	2.4 ± 0.1°	1.0 ± 0.1°

Table 6-1 Radial sampling distributions in 10 subjects with normal sinus rhythm. Adapted from (95).

The percent ideal uniformity for all 10 normal subjects is shown in Table 6-2.

	Sampling Scheme (shots-segments-projections)						
	1-128-65	2-64-97	8-16-121	4-8-29	4-16-57	4-32-113	4-64-225
Random	50.1 ± 0.1	50.3 ± 0.2	50.2 ± 0.1	51.0 ± 0.1	50.5 ± 0.1	50.3 ± 0.1	50.1 ± 0.1
Golden	90.6 ± 0.1	61.7 ± 4.9	50.5 ± 5.6	57.9 ± 2.0	56.9 ± 3.9	51.9 ± 7.5	42.7 ± 8.4
ARKS	94.9 ± 0.1	68.5 ± 0.3	64.5 ± 0.1	69.1 ± 0.7	67.1 ± 0.6	65.5 ± 0.3	64.1 ± 0.3

Table 6-2 Percent Ideal performance P in 10 subjects with normal sinus rhythm. Adapted from (95).

Overall, ARKS had P = 64-69% for multi-shot sampling schemes and P = 94.9 ± 0.1% for a single-shot sampling scheme (1-128-65). The percent ideal uniformity variation across all ten subjects was low (P = 0.1-0.7%). In comparison, random sampling consistently was P = 50-51% and golden angle sampling P = 47-61%. As expected, golden angle sampling had very high single-shot percent ideal uniformity P = 90.6 ± 0.1%.

6.4.2: Arrhythmia Subjects

An example of ARKS sampling for a subject with a regular arrhythmia is shown in Figure 6.7. The rhythm in this subject featured a normal beat (0.76 ± 0.03 sec), a second beat interrupted by a pre-ventricular contraction (0.36 ± 0.02 sec), followed by a third long beat with a longer RR-interval (1.2 ± 0.05 sec). Each of the 3 beats were correctly differentiated and segmented for ARKS, despite distortion of the ECG waveform by the electrohemodynamic effect of the 1.5 T MRI scanner (c.f. Figure 6.7a, for which the ECG was obtained outside of the MRI scanner). Simulated ARKS images correctly depicted the tri-beat arrhythmia morphology in real-time (Figure 6.7g).

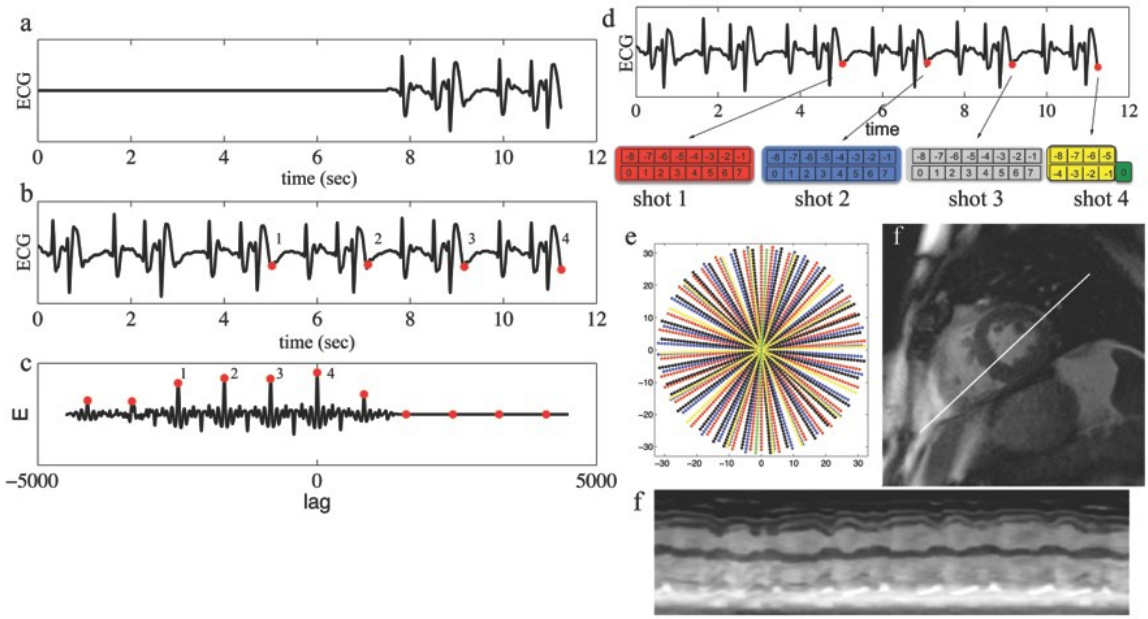

Figure 6.7 Diagram showing adaptive radial projections for a patient with a severe arrhythmia using a 4-16-57 sampling scheme (shots-segments-projections). **a** a signal buffer S_s with the most recent physiologic data (1-2 heart beats). **b** a large buffer S_L storing a previous history of the physiologic signal. 4 similar periods of the cardiac cycle are labeled (red). **c** cross-correlation between buffers S_s and S_L. Local maxima of signal overlap are labeled (red). The negative lags for the first 4 local maxima are used to label the ECG in **b**. **d** For the first 3 shots, 16 radial projections (segments) are acquired and labeled -8 to 7, with the 0 projection corresponding to the lag index in **c**. 8 projections are acquired in the last shot and together these 56 projections are used to determine the angle θ of the 57th projection. **e** 57 k-space radial projections. The color of each projection corresponds to the shot index in **d**. **f** simulated image from the radial projections acquired in **e**. **g** time-varying ventricular volume is shown from the intersection (white line) in **f**. Adapted from (95).

For both subjects, χ_1 and P were within $\sigma < 1$ of normal subjects (c.f. Table 6-1 and Table 6-2). ARKS correctly identified the cardiac phase in both arrhythmia patients and both χ and CDF had robust performance to beat-to-beat variations in rhythm and heart rate (Figure 6.8).

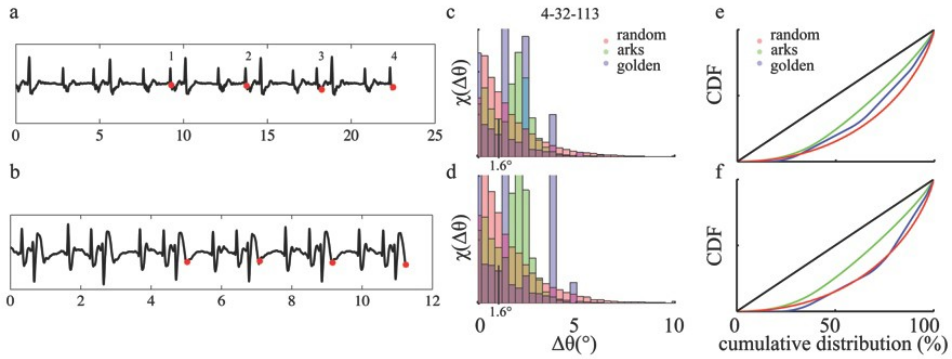

Figure 6.8 ECG signals (**a** - **b**), probability distribution χ (**c** - **d**) and cumulative distribution functions CDF (**e** - **f**) for a 4-32-113 radial acquisition scheme in 2 patients (subject 1 = **a**, **c**, **e**; subject 2 = **b**, **d**, **f**) with abnormal heart rhythm. Adapted from (95).

6.5: Discussion

We designed a method for MRI that continuously adapts a k-space radial sampling trajectory to changes in physiology and maximizes motion consistency between periods using a physiologic feedback signal. We foresee that a main application of this method will be to improve cardiovascular MRI image examinations by combining new data with additional data from previous periods to improve image quality, guaranteeing that the sampling trajectory is uniform, reducing Nyquist undersampling artifacts, and permitting continuous image reconstruction and display in real-time. While commonly used prospective and retrospective cardiac MRI exams do respond to changes in physiology, images are reconstructed and shown only after all data from multiple periods are collected, and, it is usually only a single signal, detection of the R-wave, that is used to inform changes to the k-space trajectory and gradients G for spatial encoding. A disadvantage of infrequent, once-per-period k-space sampling trajectory updates is they

cannot react quickly to complex changes in physiology, such as heart rate variations, arrhythmias, or respiration.

Retrospective cine can adapt to moderate variations in heart rate with minimal motion artifacts and loss of image data from late- and end-diastolic periods (41). Feinstein, et al. reduced the impact of heart rate variations using the beat-to-beat RR-interval to sort, temporally scale and interpolate the acquired MRI signals into the correct cardiac phase (42). ARKS shares the benefits of retrospective MRI scans, including continuous collection of imaging data for reconstruction of all cardiac phases, including late and end-diastole, image display in smooth, continuous cine loop, and uninterrupted RF excitation, so that the magnetization reaches a steady-state, reducing transient fluctuations of the measured signal (lightning artifact), and sharing of data across multiple periods to improve image quality. While a major advantage of ARKS acquisition is that data can be continuously reconstructed and displayed in real-time, there is also the potential to continuously adapt a retrospective Cartesian exam in response to physiology using a signal matching algorithm similar to ARKS (e.g. cross-correlation), to determine a new Cartesian phase-encoding trajectory and fill low k-space signal density.

When ectopy does occur during a retrospective examination, arrhythmia rejection is used to discard inconsistent data and reacquire it during the next normal period. Arrhythmia rejection is not always desirable since useful information about cardiac ectopy and true ventricular function is lost. Moreover, as was shown in Figure 6.1, there are situations in fact where there is no normal sinus rhythm and retrospective cine MRI would fail to correctly synthesize data based on the time from the R-wave alone or if the

correct R-wave was not detected correctly. These retrospective MRI scans are not able to adapt to physiologic changes because the motion is no longer consistent between periods, so the entire data set must be reacquired under the new physiologic condition.

There is considerable interest to collect and reconstruct MRI data in real-time since altogether this avoids the problem of inconsistent motion between periods. In real-time MRI, only consecutive temporal data is combined to form an image, but an important problem is to obtain images with sufficient signal-to-noise ratio and spatial resolution from limited data, without sacrificing intra-period temporal resolution. Recent advances in multiple detector (parallel) imaging and compressed sensing data reconstruction permit high quality images to be reconstructed from k-space data sampled far below the Nyquist limit (48,52,97,98). Nevertheless, it is generally recognized that reconstructing data across multiple periods would provide higher image quality if the motion is consistent across periods. ARKS continuously adapts to the physiologic signal and uses information from previous periods to optimize the uniformity of the sampling trajectory at all times. ARKS potentially has the advantages of both real-time, in that images are shown continuously to the viewer as the data is collected, and multiple period data sampling, in that additional data is used to reconstruct images at higher signal-to-noise ratio and spatial resolution.

On the one hand, it could be argued that multi-shot cine MRI may become increasingly unnecessary as MRI technology and hardware becomes more sophisticated, but, on the other hand, when there exists consistent data, then it can and probably should be used to further reduce artifacts and improve signal-to-noise ratio. In addition, it is not clear that

real-time exams could ever be performed with adequate spatiotemporal resolution with 3D coverage without a multi-period sampling approach. Hence, for 3D spatial encoding trajectories, ARKS is potentially attractive because it could offer both real-time display and 3D coverage.

A limitation of ARKS is that, for multi-shot acquisitions, the number of segments and shots is pre-determined by the user. Since new radial projections are determined in real-time, it is not possible to retrospectively reconstruct data from a different number of segments/shots and guarantee optimal k-space uniformity. Interventional studies may still benefit from ARKS, since the acquisition scheme (segments-shots-projections) can be adapted in real-time time, so that the user may alter the temporal, spatial resolution, artifacts and signal-to-noise while ensuring k-space uniformity. Golden angle sampling was shown theoretically to uniformly sample k-space for any number of consecutive projections and in their paper Winkelmann, et al. derived an analytical formula for the largest occurring azimuthal separation between two projections (72). This formula does not apply well to multi-shot k-space trajectories, since golden angle spacing of projections is appears to be guaranteed only for consecutive, but not non-consecutive, multi-beat data. For some schemes (e.g. 4-64-225, Table 6-2) a multi-shot golden angle sampling trajectory had lower percent ideal performance than random sampling, presumably because there was significant overlap among projections from multiple periods. For ARKS, it was not possible to derive an analytical formula for the angular separation $\Delta\theta$, since the polar angle varies unpredictably between consecutive

projections, but data for the 10 normal subjects and 2 arrhythmia patients suggest that high uniformity is achieved regardless.

The technical challenge of continuously adapting the k-space trajectory requires interaction between at least three potentially asynchronous processes (i.e. physiologic signal measurement, the signal matching routine, and MRI scanning). These signals may be coordinated asynchronously, where signals or new projection angles are simply delivered to the MRI scanner as soon as they are calculated, or synchronously, where one process lies dormant until the other is ready to coordinate a hand-shake. The real-time determination of new projections can be calculated much more rapidly than the MRI scan repetition time. The most time-consuming aspect of the algorithm is cross-correlation, which can be calculated within a millisecond using a fast Fourier transform on a personal computer. It is, therefore, quite reasonable to expect that a new projection would be available.

6.6: Conclusions

Adaptive real-time k-space sampling is a near-optimal sampling scheme that shares the benefits of real-time display, improves the signal-to-noise and artifact levels of a multi-shot radial k-space trajectory and, by adapting to a physiologic signal, mitigates deleterious motion artifacts. We anticipate that this approach to k-space sampling would have benefits for clinical examinations of the heart.

Chapter 7: Real Time-MRI Technique For Determining Left Ventricle Pressure-Volume Loops

7.1: Abstract

As discussed in Chapter 2, determination of the left ventricular (LV) end-systolic pressure-volume (PV) relationships (ESPVR) from rapid variations in loading conditions is the gold standard for assessment of LV function. Cine magnetic resonance imaging (MRI) does not have sufficient spatiotemporal resolution to assess beat-to-beat changes of the LV PV relationship required to measure the LV ESPVR or preload-recruitable stroke work (PRSW). Our aim was to apply the real-time MRI and semi-automated LV measurement of LV volume discussed in Chapter 4 to measure PV relations in large animals under normal and inotropically stressed physiologic conditions.

We determined that PV relationships could be accurately measured using an image exposure time T_{ex} < 100 ms and frame rate T_{fr} < 50 ms at elevated heart rates (~140 bpm) using a golden angle radial MRI k-space trajectory and active contour segmentation. With an optimized exposure time (T_{ex} = 95 ms and frame rate T_{fr} = 2.8 ms), we found that there was no significant difference between cine and real-time MRI at rest in end-diastolic volume (EDV), end-systolic volume (ESV), ejection fraction (EF), stroke volume (SV) or cardiac output (CO) (n=5, P<0.05) at either normal or elevated heart rates. We found ESPVR increased from 1.9 ± 0.7 to 3.1 ± 0.3 mmHg/mL and

PRSW increased from 6.2 ± 1.2 to 9.1 ± 0.9 mmHg during continuous IV dobutamine infusion (n=5, $P<0.05$).

Real-time MRI can assess LV volumes, ESPVR and PRSW at baseline and elevated inotropic states.

7.2: Introduction

Left ventricular (LV) performance is coupled to loading conditions (i.e. preload and afterload) and myocardial contractility (99,100). Therefore, load-independence is an important means to isolate and study LV contractility in preclinical studies of cardiovascular pharmaceuticals and devices (101). Pioneering work by Sagawa, et al. and Glower et al. demonstrated the validity of end-systolic pressure-volume relations (ESPVR) and preload recruitable stroke work (PRSW) as load-independent measures of myocardial contractility (20,102). Both ESPVR and PRSW are dependent on the simultaneous measurement of LV pressure and volume as loading conditions are rapidly varied. Precise and rapid assessment of LV pressure is readily achieved with high fidelity catheter-based pressure transducers; however, such measurements of LV volume are much more difficult and less reliable.

The most commonly used technologies for measuring LV volumes are ultrasonic sonomicrometry transducers and conductance catheters. Sonomicrometry employs small ultrasonic transducers that transmit sound signals to each other; the distance between transducers is determined by the transit-time of the signals. This technique is limited by the requirement for surgical implantation and assumptions related to LV shape

and wall thickness. Conductance catheters measure electrical conductance of LV blood, which is then converted to blood volume using formulae that are dependent on the electrical resistance of blood, distance between electrodes, parallel resistance of the myocardium and poorly defined constants. Most of these parameters are difficult to measure accurately and vary over time and between subjects.

Cardiovascular magnetic resonance allows for excellent tomographic imaging of the LV (103–106); however, slow acquisition times prohibit continuous estimation of LV volume and transient volume changes during preload reduction. Echo planar imaging MRI allows for a significant reduction in scan time (103), but there would be clear advantages to using real-time MRI to continuously measure beat-to-beat changes in LV volume.

In this study, we developed a real-time MRI technique to continuously measure LV volume and pressure during transient loading conditions in anesthetized pigs. Calibration data is first acquired from a volumetric cine MRI scan and then a single short axis real-time scan is performed at mid-ventricle. The real-time approach used a non-Cartesian sampling trajectory, in which consecutive k-space projections are separated by the golden angle (111.25 degrees). Since consecutive golden angle projections are optimally distributed in k-space, we were able to retrospectively reconstruct images from any number of projections to determine the spatiotemporal resolution sufficient to measure LV PV loops and derive ESPVR, PRSW, and other PV relationships.

7.3: Method

7.3.1: Overview

A schematic depicting the methodology used to determine real-time LV PV relationships from MRI is shown in Figure 7.1

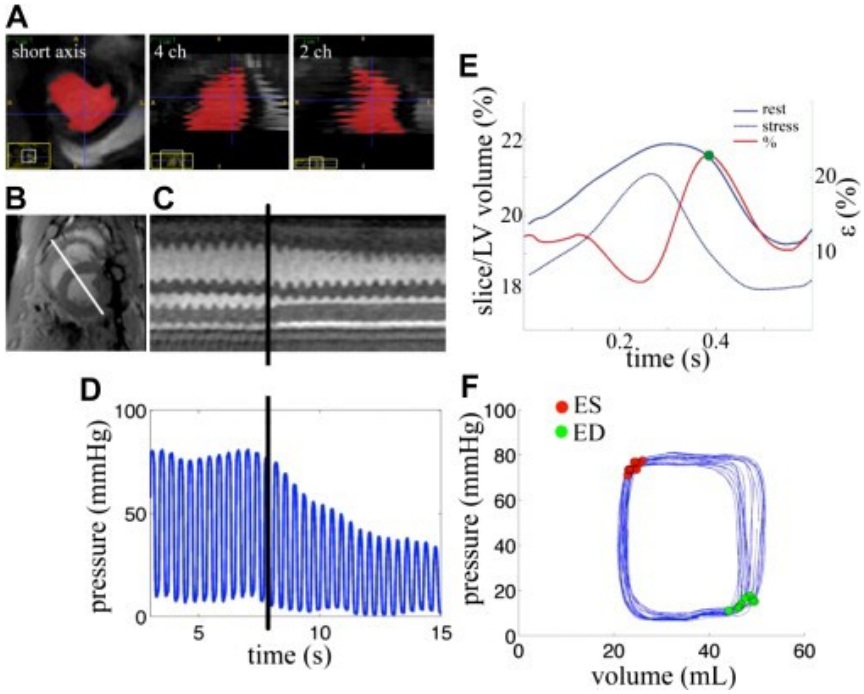

Figure 7.1 Method for real-time magnetic resonance (MR) measurement of left ventricular (LV) pressure volume (PV) loops. **A** Time-varying LV volume; 4 chamber (ch) and 2 chamber views of the segmentation (red) are overlaid on a cine images. **B** single-slice real-time MR image at mid-ventricle. **C** One-dimensional (1D) profile intersecting the septum. A white line indicates the location of the 1D projection in **B**. The occlusion time is indicated with a black bar in **C** and **D**. **D** The LV pressure is matched synchronously to each radiofrequency pulse. **E** The ratio of the slice volume in **B** to the global LV volume in **A**. The time-varying error in the slice to volume ratio is shown in red. Peak error is labeled in green. **F** The PV loop at rest, derived from 2D real-time MRI and scaled to LV volumes using ratio in **E**. (ED = end-diastolic; ES = end-systolic). Adapted from (107).

This approach solves for real-time 3D LV volumes from a 2D single-slice scan at mid-ventricle, using a high-resolution 3D cine MRI scan to calibrate (scale) the real-time

data. 3D cine MRI scans were acquired at each inotropic state (rest and stress) to minimize the calibration error. Time-varying LV volume was determined by semi-automated active contour segmentation of 3D cine data (Figure 7.1A). LV short axis images were reconstructed from undersampled 2D radial k-space data (Figure 7.1B and C) and MR radiofrequency pulses were synchronized with intraventricular pressure to match each image frame to measured pressure in real time (Figure 7.1D). The time-varying relationship between the 2D slice volume and total LV volume was determined during the cardiac cycle (Figure 7.1E) and used to calibrate real-time slice volumes; the result was a measurement of global LV PV relationships (Figure 7.1F).

7.3.2: Instrumentation

A physiologic monitoring system was used to synchronize LV pressure with the MRI acquisition. The fiber optic signal was converted to a 0–5 V electronic signal (O/E converter, Siemens Healthcare). LV pressure was obtained using a pressure transducer (Mikro-Tip; Millar Instruments, Houston, TX) and connected to a transducer amplifier (Gould). 0–5 V LV pressure and radiofrequency pulse timing were digitized at 2 kHz with a manifold analog to digital converter (NI USB6009 Multifunction DAQ, National Instruments, Austin, TX), and recorded (LabView; National Instruments, Austin, TX).

7.3.3: Animal Procedures

The University of Pennsylvania Institutional Animal Care and Use Committee approved all experiments. Healthy Yorkshire swine (N=5, mean weight = 44.3 ± 6.0 kg) were sedated with 25–30 mg/kg intramuscular ketamine, intubated and anesthesia was

initiated and maintained with a mixture of isoflurane (2–5%) and oxygen throughout the procedure. Central arterial and venous access was surgically obtained in each animal. Transient LV preload reduction was achieved by expandable vascular occluders (In Vivo Metric; Healdsburg, CA) placed around the inferior (20 mm) and superior (24 mm) vena cavae. Occluding devices were inflated gradually over 20–30 seconds to transiently reduce LV volume.

7.3.4: MRI

MRI was performed on a 3 T clinical imaging system (Tim Trio Model, Siemens Healthcare, Erlangen, Germany). Cine CMR data was obtained using a 2D multislice retrospectively-gated cine balanced steady-state free-precession acquisition with the following imaging parameters, TE = 1.2 ms, TR = 2.4 ms, matrix = 192 × 156, FOV = 300 × 240 mm2, BW = 1184 Hz/pixel, segments = 7, temporal resolution ~ 20 ms, phases = 30, and 4 mm slice thickness.

Real time cine MRI data was obtained using a 2D radial k-space trajectory with golden angle view ordering (72) and the following imaging parameters, TE = 1.82 ms, TR = 2.8 ms, Np = 128, FOV = 280 × 280 mm, BW = 1184 Hz/pixel.

7.3.5: Non-Cartesian Parallel Image Reconstruction

2D radial k-space data was reconstructed using a non-Cartesian SENSE (108) utilizing view sharing, a conjugate gradient solver (59). Image reconstruction was performed on a graphical processing unit workstation using open source software (47).

7.3.6: Active Contour Segmentation of Cine and Real-Time MRI

One practical challenge was the time-efficient determination of LV volume from thousands of image frames. Manual segmentation of the endocardial contour was exceedingly burdensome because thousands of images from a single experiment require segmentation. To overcome this challenge, we used a semi-automatic active contour, level-set algorithm to segment real-time image frames and extract LV volume. Both cine and real-time LV volumes were measured using a semi-automatic segmentation algorithm. Segmentation was performed by active contours (60).

7.3.7: Calibration Scan

A full volume cine MRI was acquired under rest and stress conditions and used to calibrate (scale) single slice 2D real-time MR images obtained at mid-ventricle. The real-time LV volume was computed from a single slice using the slice-to-volume ratio determined by the calibration scan, using ES and ED as reference points for interpolation at each point in the cardiac cycle. ES was the time at maximum elastance (= P/Vmax) and ED was defined as the bottom right corner of the PV loop. We realized that the calibration approach would introduce error if there were differences in heart rate between the calibration and real-time scan, so we estimated the mean and peak percent difference (ε_m and ε_p) between these curves at normal and elevated heart rates (cf. (Figure 7.1E). Stroke work was calculated by trapezoidal numerical integration. Mean end-systolic volume (ESV), end-diastolic volume (EDV), stroke volume (SV), ejection fraction (EF) and stroke work (SW) were reported for 5–10 heartbeats at end-expiration

at rest. The end-systolic pressure volume relationship (ESPVR) was estimated using a linear model. The volume axis intercept of the ESPVR V_0 was the x-intercept of the ESPVR. PRSW was determined by trapezoidal numerical integration.

7.3.8: Statistical Analysis

To examine differences between cine and real-time measured LV parameters, differences caused by inotropic state or the effect of preload reduction on hemodynamic function, we analyzed results using a paired-samples t-test at a significance level of $P < 0.05$ (SPSS Statistics, IBM, Version 20). Each pair of the paired-samples t-test was from the same animal.

7.4: Results

7.4.1: The Effect of Image Exposure Time and Frame Rate on Temporal Resolution and Measured LV Volume

We did not know *a priori* what temporal resolution was sufficient to measure PV relationships. To address this question, we varied two reconstruction parameters that affect temporal resolution, the image exposure time T_{ex} and image frame rate T_{fr} and measured LV volume and pressure. T_{ex} is analogous to camera shutter opening time, since it determines how much data is used to reconstruct a single image frame. $T_{ex} = N_P TR$, where N_P was the number of radial projections per image frame and TR the usual repetition time of the MRI pulse sequence. Image frame rate T_{fr} was the time

between adjacent image frames in playback and was varied by sharing radial projections between image frames. The highest possible T_{fr} was achieved when $N_P - 1$ radial projections were shared between adjacent image frames, i.e. $T_{fr} = TR$. While observable motion, such as LV wall motion, may be reduced with increasing T_{ex} and T_{fr}, longer T_{ex} improved the image signal-to-noise ratio and facilitated more dense and uniform k-space sampling density, reducing radial streak artifacts.

We measured the relationship between T_{ex} and EDV, ESV, EF and PV loops from 12 consecutive heart beats during rest (mean heart rate = 111 ± 23.1 bpm, n=1) and during continuous infusion of dobutamine (mean heart rate = 140 ± 12.4 bpm, n=1) and in comparison to a breathhold, Cartesian, k-space segmented, retrospective cine acquisition (T_{fr} = 22 ms). We found that there was a reduction in measured EDV and increase in ESV with increasing T_{ex} (Figure 7.2A,B; fixed T_{fr} = 2.8 ms). Overall, LV volume changes were the most rapid at end-systole, resulting in significantly underestimated EF for T_{ex} > 100 ms. Therefore, suboptimal T_{ex} did not capture fast motion to measure LV volume at elevated heart rates.

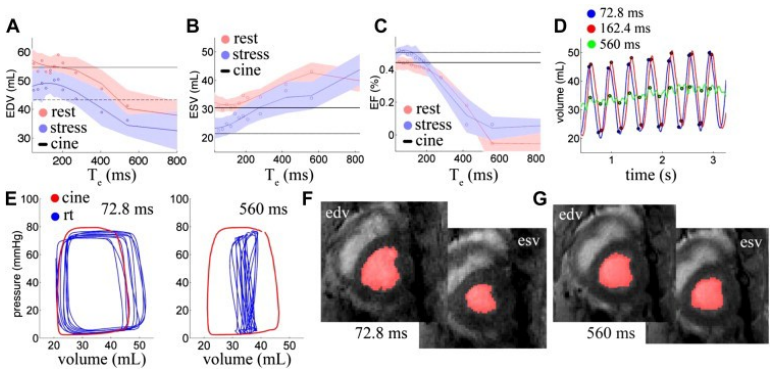

Figure 7.2 Dependence of measured heart function on exposure time (T_{ex}) under rest and stress physiology. **A** End-diastolic volume (EDV) was the lower-right corner of the pressure-volume (PV) loop. **B** The end systolic volume (ESV) was the upper-left corner of the PV loop. **C** Ejection fraction was calculated from **A** and **B**. **D** Time-varying volume under stress conditions for T_{ex} = 72.8, 162.4 and 560 ms and with continuous breathing. **E** The PV loops for cine and real-time acquisitions for T_{ex} = 72.8 and 560 ms. **F** and **G** Image frames at end-diastole and at end-systole with segmented volume overlay for T_{ex} = 72.8 and 560 ms. Error is the SD across 10 end-expiratory heartbeats. Solid black lines indicate cine data. Adapted from (107).

Time-varying volumes for images reconstructed at T_{ex} = 72.8, 162.4 and 560 ms are shown in Figure 7.2D. There was some variation in EDV due to respiratory motion, but overall we observed that accurate volumes could be measured even at intermediate exposure time (T_{ex} = 162.4 ms). The PV loop shape was progressively distorted as T_{ex} increased and this was a direct consequence of image blurring (Figure 7.2E). Maximum loop distortion was observed at high T_{ex}, with overlap of diastolic and systolic isovolumic trajectories. Considerable blurring was observed at very low exposure time (T_{ex} =560 ms; Figure 7.2G) such that EDV and ESV were nearly the same value..

We next found the relationship between T_{fr} and LV function parameters (at fixed exposure time T_{ex}, = 95.2 ms; *Np* = 34). A relationship was observed between EDV,

ESV, EF and T_{fr}, such that sufficiently low frame rate greatly reduced apparent LV EF (Figure 7.3). Overall, we observed that T_{fr} should be somewhat lower (T_{fr} < 50 ms) than T_{ex}, to correctly measure LV volume.

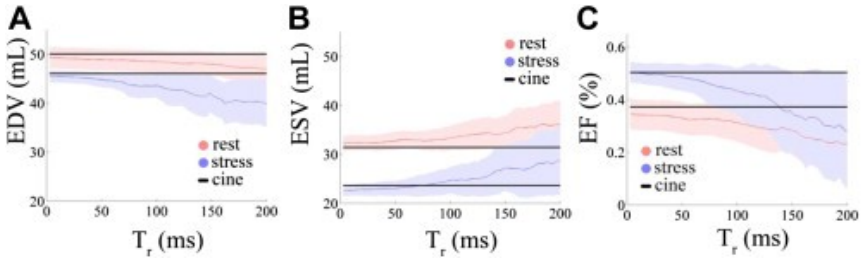

Figure 7.3 Dependence of observed end-diastolic volume (EDV), end-systolic volume (ESV) and ejection fraction (EF) on temporal resolution (T_{fr}) under rest and stress physiology. **A** The EDV was the lower-right of the PV loop. **B** The ESV was the upper-left corner of the PV loop. **C** The EF was calculated from **A** and **B**. Error is the standard deviation across 10 end-expiratory heartbeats. Solid black lines indicate cine data. Adapted from (107).

7.4.2: Comparison of Real-Time and Cine MRI PV Loops

We sought to determine whether real-time MRI could reproducibly measure PV relationships in agreement with cine MRI at baseline in several animals. We compared real-time and cine PV loops, reconstructing real-time image frames at T_{ex} = 95.2 ms and T_{fr} = 2.8 ms based on our observations in Figure 7.2 and Figure 7.3. Time-varying pressure and volume and PV loops are shown for one animal in Figure 7.4.

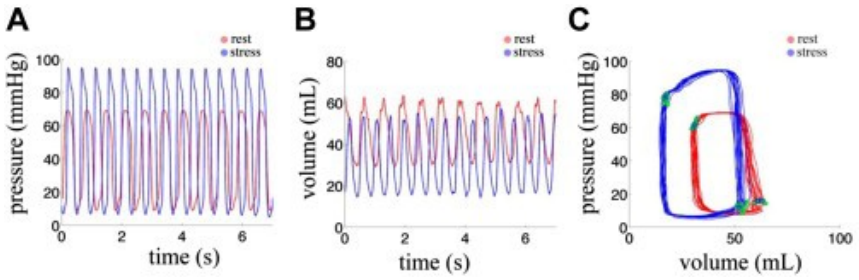

Figure 7.4 Real-time pressure-volume (PV) loops from a swine under rest and stress physiology. (A) The PV loops were measured at rest and during continuous dobutamine infusion. Left ventricular (LV) pressure obtained with an intraventricular catheter was synchronized with each radiofrequency pulse. (B) Time-varying LV pressure, and (C) LV volume during 12 seconds of continuous acquisition. Adapted from (107).

As expected, a left- and upward shift in the PV loop under increased inotropic state was observed. Similar results were observed from PV loops in all animals. Average hemodynamic parameters under rest and stress conditions are shown in Table 7-1. There was no significant difference between EDV, ESV, EF, SV or SW measured with cine and real-time at either normal or elevated heart rates (P <0.05; n=5).

Hemodynamic Values	Real-Time (T_{ex}=95.2 ms, T_{fr} = 2.8ms) Rest (n=5)	Real-Time (T_{ex}=95.2 ms, T_{fr} = 2.8ms) Inotropic Stress (n=5)	Cine Rest (n=5)	Cine Inotropic Stress (n=5)
Heart rate, bpm	112.1 ± 22.9	140.2 ± 20.2	116.8 ± 21.1	147.6 ± 16.1
EDV_{LV}, mL	57.9 ± 13.2	47.0 ± 5.2	61.1 ± 10.Y	54.1 ± 5.7
ESV_{LV}, mL	35.3 ± 7.1	23.6 ± 4.1	35.8 ± 8.0	25.3 ± 10.7
SV_{LV}, mL	22.7 ± 8.3	23.4 ± 7.5	25.3 ± 5.8	28.9 ± 3.7
EF_{LV}	0.37 ±0.09	0.49 ±0.11	0.41 ± 0.07	0.53 ± 0.03
CO_{LV}, L/minute	2.6 ± 0.7	3.2 ± 0.9	2.9 ± 0.6	3.3 ± 1.0
LV properties				
EDPVR, mmHg/mL	0.30 ± 0.13	0.28 ± 0.19		
ESPVR, mmHg/mL	1.9 ± 0.7	3.1 ± 0.3		
V_0, mL	-8.1 ± 13.8	-1.9 ± 4.1		
Stroke work, mmHg mL	221.3 ± 51.9	306.9 ±96.4		
PRSW, mm Hg	6.2 ± 1.2	9.1 ± 0.9		

Table 7-1 Average Hemodynamic Parameters Under Rest and Stress Conditions Adapted from (107).

Although there was excellent agreement between baseline cine and real-time MRI at normal and elevated heart rates, determination of global LV volume from calibrated 2D real-time MRI could introduce errors if the heart rate changed between the calibration and real-time scans. To address this question, we found the error resulting from using calibration data obtained at resting heart rates to calibrate real time data at elevated heart rates. We estimated then the mean and peak error in ventricular volume (ε_m and ε_p) resulting from heart rate differences between rest (mean heart rate = 112 bpm) and stress (mean heart rate = 141 bpm) calibration scans. We found ε_m = 5.6% and ε_p = 14.2% (n=5, cf. Figure 7.1) and, since the anesthetized animals did not greatly increase their heart rate in response to preload reduction, we believe these errors represent upper-limits to the true error. Since, for all other experiments, the calibration scan at

each inotropic condition, measured LV volume was unaffected by heart rate changes between rest and stress studies.

7.4.3: Elastance at Rest and During Augmented Contractility

We then investigated ESPVR, EDPVR, and the volume V_0 at zero pressure by observing PV relations during transient LV volume reduction using real-time MRI (Figure 7.5).

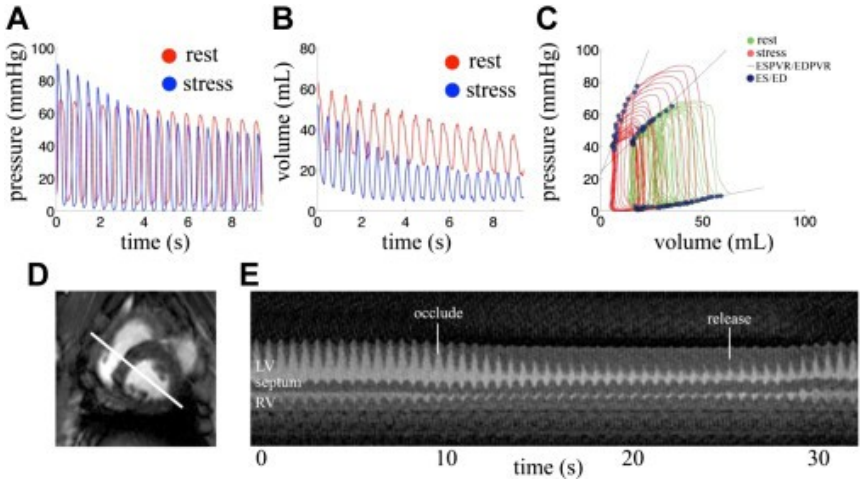

Figure 7.5 Real-time pressure-volume (PV) loops from a swine under rest and stress conditions during a preload reduction experiment. **A** Time-varying left ventricular (LV) pressure and **B** LV volume during 12 seconds of continuous acquisition throughout the preload reduction experiment. **C** The PV loops were measured at rest and at increased inotropic state. The end-systolic pressure volume relationship (ESPVR) was fit with a linear function (solid red line) through ES points (green points). **D** One-dimensional (1D) projection intersecting the LV parallel to the LV outflow tract. **E** 1D profile (magnetic resonance m-mode image) of LV, right ventricle, and septum from the projection of the real-time data in **D**. Occlusion and release times are indicated with white lines. (EDPVR = end-diastolic pressure-volume relationship). Adapted from (107).

We observed that the slope of the ESPVR appeared to increase at low EDV, indicating nonlinearity and load-dependence, possibly a result of sympathetic response to preload reduction. Overall, ESPVR increased from 1.9 ± 0.7 to 3.1 ± 0.3 mmHg/mL ($P < 0.05$; n=5). Residual volumes were not different from zero, suggesting that the normal LV

efficiently eliminated blood (V_0,rest = −0.1 ± 6.5 mL, V0,stress = 2.0 ± 4.5 mL, $P < 0.05$; n=5).

7.4.4: Preload-Recruitable Stroke Work

We investigated whether there was a decrease in stroke work (SW) under reduced loading conditions as expected by the Frank-Starling mechanism and if there was a response to inotropic state. Stroke work was measured continuously throughout the unloading period and during recovery following release using real-time MRI (Figure 7.6A,C).

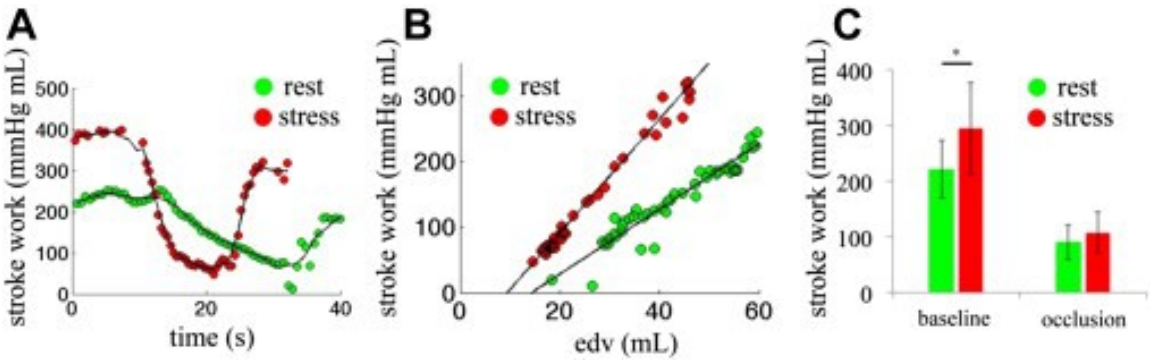

Figure 7.6 Myocardial stroke work under rest and stress conditions during a preload reduction experiment. **A** Time-varying stroke work during transient reduction in end-diastolic volume (EDV) and release. **B** Relationship between stroke work and EDV (preload-recruitable stroke work). **C** Relationship between stroke work, EDV, and inotropic state. Adapted from (107).

Not only was SW reduced under resting conditions (SW = 221.3 ± 51.9 to 90 ± 31.8 mmHg mL, paired t-test, $P < 0.05$; n = 5), but also, in an augmented inotropic state, and for the same EDV, SW was increased as shown by the increased slope of the Frank-Starling curve (6.19 ± 1.2 to 9.1 ± 0.9 mmHg, $P < 0.05$; n = 5) (Figure 7.6B).

7.5: Discussion

Recording LV pressure-volume data during rapidly changing loading conditions can yield important information regarding myocardial systolic performance. The validity of such analysis is highly dependent on an accurate and rapid measurement of LV volume and pressure simultaneously. A number of techniques have been used to rapidly estimate LV volume; however, all require the use of major simplifying assumptions that limit accuracy. We developed a technique utilizing MRI to continuously measure LV volume and pressure simultaneously, allowing for the quantitative assessment of important load-independent measures of LV contractile function.

Image temporal resolution and measured LV volume were found to be dependent on image exposure time and frame rate; the upper limits for these parameters were established at an elevated heart rate (T_{ex} < 100 ms, T_{fr} < 50 ms). A new development was the use of a semi-automated active contour segmentation approach for determination of LV volume from thousands of image frames. Altogether, the strong agreement between real-time and cine MRI demonstrates that the real-time methods, combined with a suitable semi-automated segmentation, can be used to obtain accurate PV relations, even at elevated heart rates.

Besides the approach shown here, PV relationships can be also estimated from stroke volume using real-time 2D through-plane velocity encoded MRI at the ascending aorta (109). We chose instead a 2D intraventricular approach because we plan to measure regional elasticity, which potentially could be obtained from 2D real-time MRI directly

from observed wall motion or strain using computational motion tracking. Variations in regional myocardial elasticity in normal subjects, let alone patients with cardiovascular disease, are relatively unknown. A limitation of this approach is that regional wall motion abnormalities can result in inaccurate measurements of global PV relationships, depending on the position of the 2D real-time imaging slice. If the 2D slice intersected a wall-motion abnormality, this would underestimate global stroke work and overestimate ESPVR.

The ESPVR has been observed to exhibit nonlinearity and dependence on afterload and is not a perfect measure of contractility (110). We observed that the slope of the ESPVR increased at low EDV, also indicating nonlinearity and load-dependence. We observed that ESPVR tended towards greater convexity at increased inotropy.

Golden angle MRI allowed us to retrospectively reconstruct images from a single experiment with variable exposure time and frame rate to optimally determine temporal resolution. In a previous validation study of radial real-time MRI (58), 80 projections were reconstructed per image frame, with T_{ex} = 200 ms and T_{fr} = 66 ms; however, we found these parameters were not sufficiently short to accurately measure LV volume at elevated heart rates.

7.5.1: Limitations

There are additional challenges to assessment of load-independent LV function in patients. Clinical use is hampered by the need for noninvasive pressure monitoring of high fidelity, accurate and continuous monitoring of LV volumes and the need to vary

loading conditions by vena caval occlusion or the use of vasoactive drugs (18). Investigators have utilized the high spatial resolution of MRI to address the second of these challenges by the 'single-beat' approach (111) or by quantification of aortic flow using real-time velocity encoded CMR as described above (109,112,113). These methods are attractive for clinical and preclinical studies, but may be insufficient for estimation of regional cardiac contractility or LV contractility in the presence of shunt or mitral regurgitation, which may often occur in ischemic heart disease.

7.6: Conclusions

In summary, we validated the ability of the method outlined in Chapter 4 to measure LV contractile function using real-time MRI-derived PV relations. Furthermore, by performing preload occlusions in large animals, we demonstrated that the techniques is able to robustly measure LV volume to estimate global ESPVR and EDPVR. This method has the potential to be used in studies of heart disease to assess regional contractile function in preclinical studies. However, this biggest limitation to this potential use is the estimation of global LV volume from a single 2D slice. In Chapter 8, we eliminate this slice-to-global conversion factor and use the 2D approach to investigate regional differences in contractile function between the base, mid-ventricle, and apex.

Chapter 8: Slice-by-slice PV loop analysis demonstrates regional differences in cardiac contractility and regional dependence on inotropic agents

8.1: Abstract

As outlined in Chapter 4 and Chapter 6, the 2D real-time MRI technique is capable of accurately measuring LV slice volume and observes changes in cardiac function due to variations in loading condition. In this project, we utilize the 2D imaging technique to investigate differences in measured contractile function along the long axis. Specifically, we observed differences in ESPVR, V_0, and EDPVR obtained from basal, mid-ventricular, or apical slices. Furthermore, the values were compared to measured slice ejection fraction (sEF), a load-dependent and slice-based measure of function.

8.2: Introduction

Apparent LV function, often quantified via stroke volume or ejection fraction, is a complex combination of myocardial contractility and loading conditions, specifically preload and afterload. Load-independent measures of function decouple cardiac contractility from these loading parameters and have been proposed as improved measures to diagnose cardiac disease (20,102,114–116).

To-date, these load-independent measures of function have described myocardial contractility as a globally uniform value. As a result, regional differences in contractility

due to varying LV geometry, anatomic tethering, or underlying tissue properties throughout the LV are combined into a single global measure. This limits the ability of these methods to detect and describe regional myocardial injury or dysfunction.

The design of interventions to limit adverse LV remodeling after myocardial infarction such as pharmacologic therapy or surgical procedures (14–17) may benefit from the use of these regional measures of function. Currently, regional methods such as slice ejection fraction, visual assessment of akinetic segments and strain are employed to assess regional function, despite their dependence on loading conditions.

In this work, we utilized a previously validated real-time MRI technique (107) to measure slice-derived LV Pressure - Volume relations during transient loading conditions to investigate regional differences in contractility in anesthetized sheep. By imaging different slice locations spanning the left ventricle, regional information was obtained in a load-independent fashion via slice derived end-systolic pressure-volume relations (sESPVR), end-diastolic pressure-volume relations (sEDPVR), and V_0 (sV_0). Regional differences in load-independent measures were observed and compared to changes observed in the slice ejection fraction (sEF), which is load-dependent.

8.3: Method

8.3.1: Overview

The methodology used to obtain slice derived Pressure-Volume (sPV) relations has been previously described by Witschey et al (107). Briefly, 2D real-time single-slice MRI

was performed along the short axis of the LV at several (n = 5 - 7) slice locations per animal ranging from apex to base. Slice volume was obtained via semi-automated segmentation of the dataset and LV pressure was synchronized with the measured slice volume, which resulted in sPV relations. Transient changes in loading condition were used to derive load-independent measures of slice function.

8.3.2: Instrumentation

A physiologic monitoring system was used to synchronize LV pressure with the MRI acquisition. The fiber optic signal sent from the MRI scanner was converted to a 0-5 V electronic signal (O/E converter; Siemens Healthcare, Malvern, PA). The LV pressure was obtained using a pressure transducer (Mikro-Tip; Millar Instruments, Houston, TX) and connected to a transducer amplifier (Millar Instruments, Houston, TX). The 0-5 V LV pressure and radiofrequency pulse timing were digitized at 2 kHz with a manifold analog to digital converter (NI USB6009 Multifunction DAQ, National Instruments, Austin, TX), and recorded (LabView; National Instruments, Clearwater, FL).

8.3.3: Animal Procedures

The University of Pennsylvania Institutional Animal Care and Use Committee approved all experiments. Healthy sheep (n = 11, mean weight = 44.6 ± 7.3 kg) were sedated with 25 to 30 mg/kg intramuscular ketamine, then intubated and anesthesia was initiated and maintained with a mixture of isoflurane (2% to 5%) and oxygen throughout the procedure. Central arterial and venous access was surgically obtained in each animal. Transient LV preload reduction was achieved by expandable balloon catheters placed in

the inferior vena cavae (Infiniti Medical, Menlo Park, CA USA). During each 2D MRI scan, the balloon catheter was inflated gradually over 10-15 seconds to reduce LV filling volume. An inotropic infusion of epinephrine was performed via continuous infusion of 0.5 μg/kg/min.

8.3.4: Measures of Slice Function

From the scanning period prior to changes in loading conditions, slice ejection fraction (sEF) was quantified as a load-dependent measure of function. From the real-time imaging data, slice-derived Pressure-Volume (sPV) relations were obtained during normal loading conditions as well as during the transient occlusion.

We quantified several load-independent measures of function derived from the sPV relations obtained during the occlusion experiment including sESPVR, sEDPVR, and sV_0. sESPVR and sEDVPR were estimate by linear fitting of end-systolic and end-diastolic points. Slice derived V_0 (sV_0) was the x-intercept of the linear sESPVR fit.

8.3.5: Statistical Analysis

The difference in load-dependent and load-independent values obtained between three different slice positions (apical, mid-ventricular, and basal) were compared using a paired Student's t-test ($p<0.05$). Furthermore, the change in values observed during inotropic infusion was also evaluated using a Student's t-test ($p<0.05$).

8.4: Results

8.4.1: Effect of Slice Location on Observed Pressure Volume Relations

For each animal, multiple sPV loops spanning the LV were generated at normal loading conditions; values obtained in one animal are shown in Figure 8.1. The transition from apex (top) to base (bottom) causes an increase in measured slice volume curve (shifting the sPV loops to the right). The slice ejection fraction (sEF) decreases in the apical to basal direction.

As described by Witschey et al, use of a balloon catheter occlusion allows for different PV loops to be measured and the estimation of slice-derived load-independent measures of function. In this study, we obtained estimates of sESPVR, sEDVPR, and sV_0. The slice-derived Pressure Volume loops and corresponding values obtained for different slice locations this subject are shown in the rightmost column in Figure 8.1. The linear fits used to generate the load-independent values resulted in high coefficients of determination for sESPVR and sV_0 (0.958 ± 0.049) as well as sEDPVR (0.923 ± 0.050).

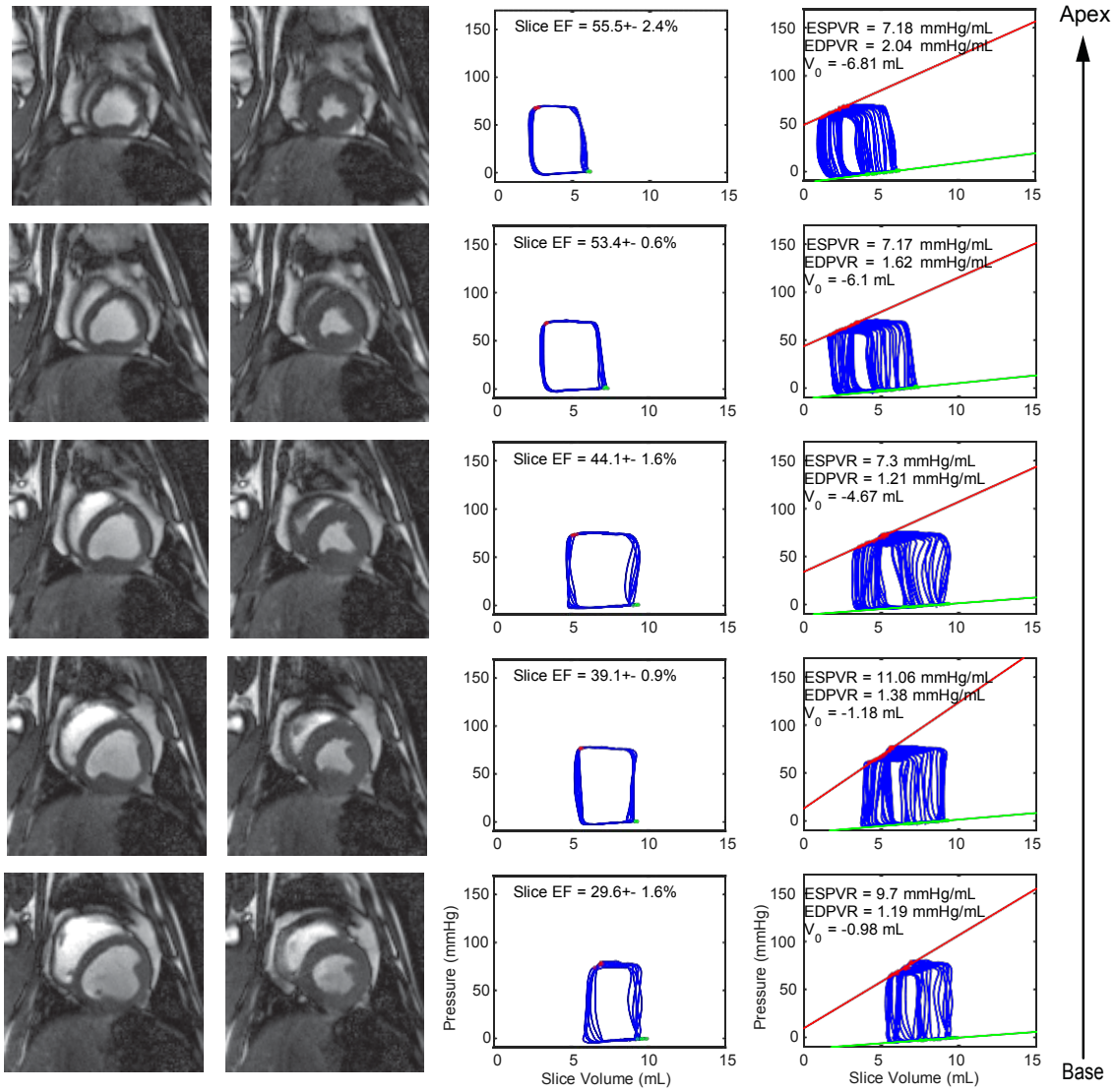

Figure 8.1 Example of Slice Derived Pressure-Volume Recordings across 5 slices from the apex (top) to base (bottom) of the LV. The first and second column show the end-diastolic and end-systolic phases of standard CINE images across the LV. Real-time imaging acquired prior to a preload occlusion allowed for a baseline Pressure-Volume loop to be acquired at each slice location. The corresponding slice EF for each slice is given. The rightmost column shows the Pressure-Volume relations during the preload occlusion. The load-independent measures ESPVR, EDPVR, and V_0 obtained for each slice are indicated on the plot. Adapted from (117).

8.4.2: Variation in Load-Dependent Function due to Slice Location

We observed changes in both load-dependent and load-independent measures of function across the LV. Grouping the slice values into apical, mid-ventricular, and basal sections allowed for regional comparisons. The results of these comparisons are shown in Figure 8.2A.

Slice EF is decreased progressively from the apex to base (59.8 ± 8.6%, 54.7 ± 7.3%, 44.9 ± 10.6%; $p<0.05$) (Figure 8.2.)

In addition to observing the variation in slice-based measures of function across the LV, 9 of the 10 animals had infusion of an inotropic agent to observe increases in contractility. The infusion of epinephrine resulted in modest changes in heart-rate (from 106.9 ± 17.4 bpm to 124.2 ± 16.7 bpm) and end-systolic LV pressure (from 89.2 ± 13.9 mmHg to 112.2 ± 27.0 mmHg).

sEF increased with inotropic infusion to 66.4 ± 14.2% in the apex, 60.1 ± 11.6% in the mid-ventricle, and 54.2 ± 13.8% in the base (Figure 8.2B). The change, relative to the rest condition, is shown in Figure 8.2C. The increase in sEF was highest in the base (123.2 ± 44.8% relative to baseline) compared to the apex (112.0 ± 19.3%) and mid-ventricle slices (110.9 ± 20.3%). The changes, relative to the baseline were all statistically significant and the increase in sEF in the base was statistically significantly higher than the other slices locations ($p<0.05$).

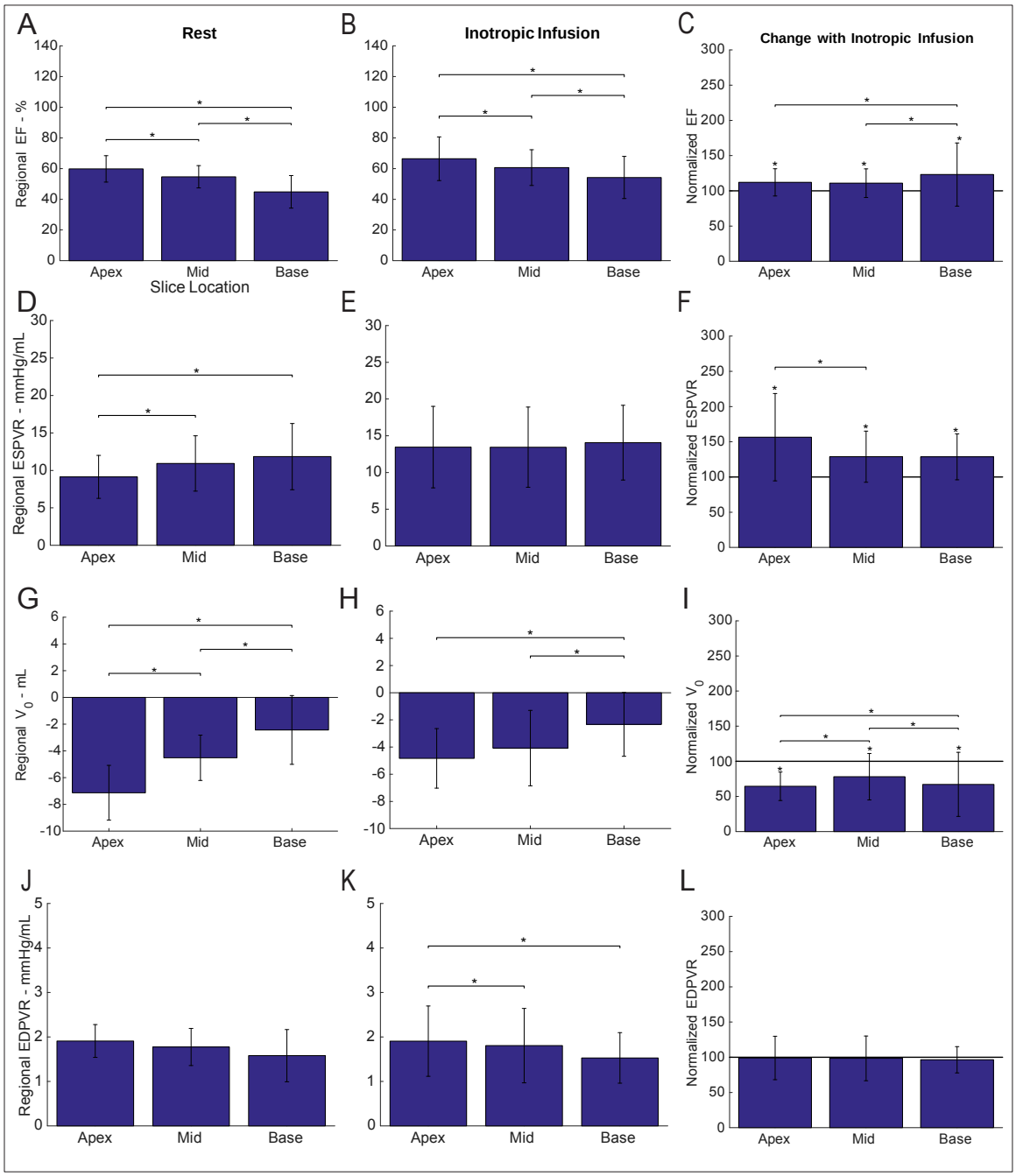

Figure 8.2 Regional differences in measured sEF (A – B), sESPVR (D – E), sV_0 (G – H) and sEDVPR (J – K) across the LV at rest and during inotropic infusion. Change in measured sEF (C), sESPVR (F), sV0 (I), and sEDPVR (L) with inotropic infusion. Adapted from (117).

8.4.3: Variation in Load-Independent Function due to Slice Location

In addition to sEF, real-time MRI allowed for quantification of load-independent measures of slice function including sESPVR, sEDPVR, and sV_0. The sESPVR increased progressively from the apex to base (9.1 ± 2.9 mmHg/mL, 10.9 ± 3.7 mmHg/mL, 11.8 ± 4.4 mmHg/mL). sESPVR in the apex was statistically significantly lower ($p<0.05$) than the mid-ventricle and the base Figure 8.2D. The difference between the mid-ventricle and base was not significant ($p = 0.291$). Inotropic infusion led to a increase in sESPVR in all regions (apex: 13.5 ± 5.5, mid-ventricle: 13.4 ± 5.5, base: 14.1 ± 5.1 mmHg/mL) Figure 8.2E. The increase in the apical slices was significantly higher than the mid-ventricle ($p<0.05$). The marked increase in the apical ESPVR eliminated the difference ($p > 0.563$) between slice regions shown in Figure 8.2F.

sV_0 increased significantly ($p<0.05$) in the apical to basal direction from -7.1 ± 2.1 mL in the apex to -4.5 ± 1.7 mL in the mid-ventricle and -2.4 ± 2.6 mL in the base which is shown in Figure 8.2G. During inotropic infusion, sV_0 increases significantly (becoming less negative) in all three regions (apex: 2.6 ± 1.8 mL, mid-ventricle: 0.8 ± 1.7 mL, and base: 0.6 ± 1.6 mL), shown in Figure 8.2I. The larger increase in the apex eliminates the difference between apex and mid-ventricle during stress ($p=0.187$).

Figure 8.2J shows a small variation in sEDPVR along apical to basal direction which does not achieve statistical significance (apex: 1.9 ± 0.4 mmHg/mL, mid-ventricle: 1.8 ± 0.4 mmHg/mL, and base: 1.6 ± 0.6 mmHg/mL). The inotropic infusion makes the difference between apex (1.9 ± 0.8 mmHg/mL) and base (1.5 ± 0.6 mmHg/mL) more

pronounced ($p < 0.05$). However, the inotropic infusion does not result in a statistically significant change relative to the baseline values.

8.5: Discussion

In this study, we used a method to generate slice-derived PV relations, which allowed for load-independent measures of function to be estimated at different slice locations. In 10 animals, we quantified and described the variation along the apical to basal direction.

The initial portion of a preload occlusion experiment was used for estimation of load-independent measures of function. This limited potential through-plane motion as well as potential non-linear portions of the load-independent measures such as ESPVR (110). In contrast to slice ejection fraction (which decreases in the basal direction), we observed an increase in sESPVR and sV_0, and no significant change in sEDPVR in the base relative to the apex. We believe there are several possible mechanisms that may explain these experimental observations.

First, the anatomic constraints of the valvular apparatus may impact the estimation of sESPVR. When the heart unloads, there is a global decrease in LV pressure. However, basal slices are constrained by the non-contractile valvular appartus which may limit the decrease in slice volume observed with unloading. As a result, basal slices appear to have a smaller ΔV for the same ΔP which results in a higher sESPVR estimate.

Another mechanism which affects basal and apical slices differently is the impact of size on the load-independent measures of function. For basal slices, the PV relations are

shifted rightward, as shown in Figure 8.1. This rightward shift can be expected to impact estimates of sV_0 in the base even if the sESPVR relations were constant across the LV.

In addition to these two mechanisms, higher contractility in the base may be necessary for efficient cardiac contraction. Specifically, the basal region may require higher contractility to ensure that the blood properly ejects from the ventricle. If the end-contractility of the base was lower, then blood moved by the apex may enter the basal slices but not be ejected (since the base could serve as an energy sink). Although the lack of changes in EDPVR indicates the passive properties of the tissues are similar, the active properties may be different to the increased stress (estimated via Laplace's law).

8.5.1: Regional response to inotropic infusion

Inotropic infusion caused a statistically significant increase in measure sESPVR and sV_0 without affecting sEDPVR . However, the scale of the magnitude is not comparable to the expected increase in myocardial work and energy consumption. The apparent dampening of the increase may be due to the increase in heart rate as well as the work per beat. To capture the change in work per unit time (per minute, for example), the change in heart rate would also need to be included.

The marked increase in sESPVR in the apex relative to the mid-ventricle and basal slices may be partly attributed to the underlying anatomy of the heart. Specifically, the apex is less encumbered by the valvular apparatus and the wringing motion can nearly empty the apical slices. Also, through-plane motion may become larger during inotropic infusion causing more of a slice shift that leads to perceived higher contractility.

In the initial experimental preparations used to develop these load-independent measures, a cardiometer was used to obtain a global volume measurement (20). The use of conductance catheters allowed for in vivo experimentation (118,119). Both the ex vivo and in vivo approaches treat a decrease in blood volume as a uniform decrease in loading conditions in the LV.

However, the geometry of the LV as well as anatomical constraints such as the right ventricle and valvular apparatus may limit the ability of certain regions to unload uniformly. In the case of regional dysfunction such as ischemic injury, this effect may become pronounced and limit the ability of global load-independent measures such as ESPVR to describe the injury. Furthermore, in the case of regional injury, global values cannot provide direct information regarding the location, spatial extent (transmurality) and remodeling process ongoing in the ventricle.

This work has allowed us to gain valuable insight into the underlying regional differences in contractility. This will serve as a first step towards characterizing the impact of regional injury (such as ischemia) in a more detailed fashion.

8.6: Conclusions

The regional differences in contractility observed in this work provide a critical step towards more region-based analysis of contractile function. Typically, ESPVR and V_0 are used to describe the entire myocardium with a single functional value. In this work, we show our approach can be tailored to provide regional information.

Despite the regional information provided, a particular slice may contain normal myocardium as well as infarcted and borderzone tissue. In this case, the volume-based ESPVR measures do not provide information related to borderzone function. Chapter 9 builds on these results and utilized motion tracking to observe changes in wall thickness in the borderzone, providing even more regional information.

Chapter 9: Assessment of Borderzone Function via Load-Independent Measures of Function

9.1: Abstract

Chapter 4 demonstrated that 2D real-time MRI can accurately measure LV slice volume. Subsequent work in Chapter 6 showed that global load-independent measures could be estimated by synchronizing the imaging experiment with LV pressure measurement and Chapter 8 used the 2D imaging technique to estimate load-independent measures of function in a slice-by-slice fashion, demonstrating regional variations. However, these approaches did not provide the ability to characterize borderzone function and distinguish it from normal myocardial or infarcted tissue. In this chapter, we address this limitation by applying motion-tracking algorithms to the 2D real-time MRI images to measure wall-thickness within regions of a slice and over time. During the imaging experiments, we performed the preload occlusions experiments described previously and measured LV pressure via a catheter. This approach allowed for regional Loop Area (a surrogate for regional myocardial work) to be estimated in different regions of a slice allowing for the borderzone to be characterized in a load-independent manner.

9.2: Introduction

As mentioned in Chapter 2, the adverse LV remodeling that occurs after a myocardial infarction is associated with poor prognosis and is a public health concern. To address this problem, several therapeutic approaches have been proposed to limit the adverse

remodeling (14–17). However, one unmet need is the ability to evaluate the impact these therapies have on the contractile function of the borderzone.

Measures obtained via conventional imaging are either global (such as end-diastolic volume to quantify dilation), load-dependent (such as strain or slice ejection fraction), or do not provide functional information (such as LGE-MRI to quantify scarring). Regional and load-independent measurements have been published but require invasive implantation of either strain gauges or Sonomicrometry crystals. This limits the locations where wall thickness or strain can be measured, the number of simultaneous measurements possible, and the widespread use of the technique.

In this work, we utilized motion-tracking techniques to measure regional wall thickness at multiple locations within a single 2D image series and measure regional Loop Area throughout a dynamic inflow occlusion experiment. We hypothesize that ischemia results in regional variations in myocardial work due to the change in tissue properties. We expect to observe normal myocardial function in tissue that is remote to the infarct and substantially depressed function in the infarct itself. We expect that the borderzone function may be impaired despite the normal perfusion due to the change in LV geometry and remodeling process in the adjacent infarct.

9.3: Method

To establish this approach two different studies were performed. First, several motion-tracking algorithms were evaluated in real-time images of clinical patients. After selecting

an algorithm, regional measures of wall-thickness in infarcted swine provided regional Loop Area estimates.

9.3.1: Motion-tracking Estimation

Nine clinical patients (age: 45.7 ± 15.7, 55% male, EF: 11 – 75%) were imaged as part of an IRB approved research study. The epicardial and endocardial borders of the myocardium were manually delineated in each image to generate a binary image of the myocardium. Motion-tracking methods were evaluated via the accuracy of tracking the binary myocardium images.

9.3.2: MR Imaging and Reconstruction

As outlined in Chapter 4, Chapter 6, and Chapter 8, short-axis, golden angle radial, bSSFP data were acquired with the following imaging parameters: TE/TR = 1.45/2.9ms, BW=900 Hz/pixel, N=128, FOV=280 mm. The reconstruction and LV slice volume quantification validated in Chapter 4 was performed using a non-Cartesian SENSE-based reconstruction with N_{spokes} = 34 on Gadgetron. (7, 8)

9.3.3: Comparison of Motion-Tracking Methods

Several non-rigid registration algorithms were utilized to obtain motion estimates relative to a baseline image frame (120). Two key elements of the motion-tracking pipeline were modified. First, the algorithm used to determine motion between two images was varied (optical flow, non-rigid b-splines, and several ANTS based techniques) (121). Second,

as described below, three different approaches for estimating motion between a series of images were implemented.

The accuracy of these two different elements was evaluated using manually contoured myocardial binary images. These manually drawn images provided a goal, which the motion-tracking algorithms tried to achieve. The accuracy of the motion-tracking-based results was quantified via the Dice Coefficient, which penalizes both false negative and false positives. For two binary images, the Dice Coefficient varies from 0 to 1 and is calculated as

$$Dice = \frac{2|A \cap B|}{|A| + |B|} \qquad [9\text{-}1]$$

where A and B are the pixels labeled as the myocardium and $|A \cap B|$ is the number of pixels shared between both images. In addition to the Dice Coefficient, the area overlap, false positive, and false negative rates were evaluated to further understand the failure modes of the algorithms.

Three different methods of non-rigid registration were performed and are described below:

Sequential Motion Registration

In image registration approaches such as optical flow, a small motion assumption is introduced (122). Therefore, the first approach implemented was a sequential registration, depicted below. By estimating the motion between consecutive frames, the

anatomical motion between consecutive frames is small (and consistent throughout the image series). However, There are several potential drawbacks to this approach. First, when there is little or no change in anatomy, the motion registration may be driven by the changes in the noise pattern (specifically, radial streaking in the 2D real-time MRI). Furthermore, this approach is sensitive to changes in the imaging frame rate or subject heart rate. If either parameter is varied, the amount of motion between frames in the registration will change. Furthermore, the sequential approach can result in the accumulation of errors. Specifically, if one of the motion estimates fail, the location of points of interest will be incorrect for subsequent registration steps leading to incorrect estimation of wall-thickness.

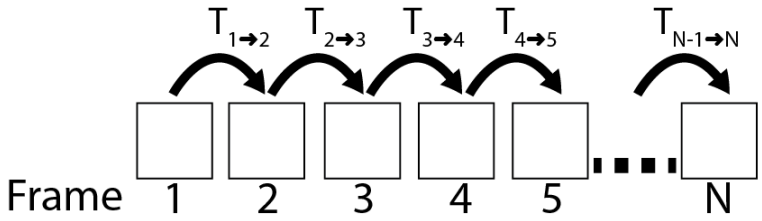

Figure 9.1 Sequntial Motion-Tracking. Adapted from (120)

Alternative Motion Registration

Due to these potential drawbacks, another motion estimation approach was implemented. In this method (depicted below), all the registrations are performed with reference to the first frame (an end-diastolic timepoint). As a result, the amount of cardiac motion estimated by the registration varies with large deformations found when the target image is in end-systole or occurs during a different respiratory phase.

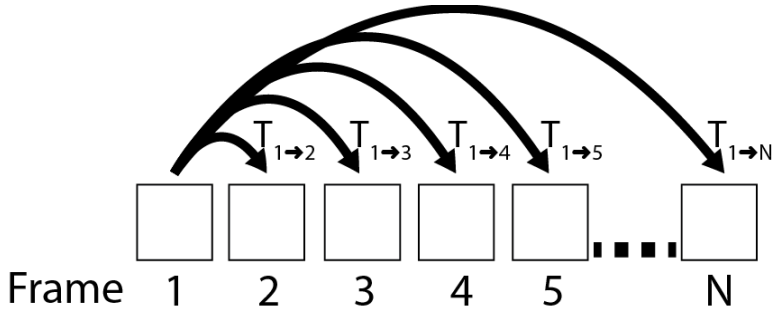

Figure 9.2 Alternative Motion-Tracking. Adapted from (120)

Although this difference in motion may prove problematic, this approach may be more robust since each registration is an independent event, which does not corrupt future motion-tracking results. As a result, discrete errors in tracking can be identified and manually removed without loss of wall-thickness measurement accuracy. Furthermore, this approach allows for temporal regularization (explored by Mohammed Shahid as part of his Master's dissertation).

Template Based Motion Registration

Finally, the registration of images from multiple patients to a common atlas or a group average has recently been exploited to understand variation in individual subjects (123). As a result, algorithms have been developed to generate a single template image from a series of observed images. We utilized this template technique to introduce an registration approach that falls between the first and second approaches described above. By generating a template image, the size of the largest deformation calculated should be decreased as it is now performed in two steps (First the registration to the template, and then the registration from the template to the desired frame). However, the drawback of this approach is that small deformations (for example between Frame 1 and

Frame 2 below), are now calculated as a deformation from Frame 1 to the template, and subsequently from the template to Frame 2.

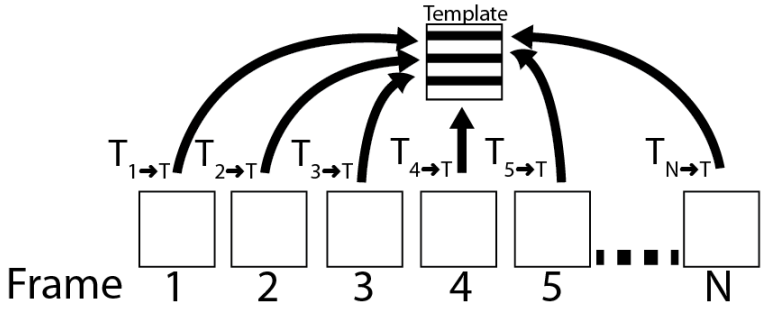

Figure 9.3 Template Based Motion-Tracking. Adapted from (120)

9.3.4: Animal Model

Swine (N=3, weight = 43kg) were entered in an IACUC-approved myocardial infarction model. After MI, the animals were allowed to recover one week before the MRI study. Balloon catheters were positioned in the vena cavas and inflated to perform an inflow occlusion. The one-week timepoint was chosen to limit the amount of wall thinning that occurs during LV remodeling. Substantial thinning of the infarct introduces noise into the wall thickness measurement and higher resolution imaging to address this limitation is left for future work.

9.3.5: MR-Compatible Physiologic Monitoring

As in Chapter 6 and Chapter 8, for the swine study, a physiologic monitoring system was used to synchronize LV pressure with the MRI acquisition. The fiber optic signal sent from the MRI scanner was converted to a 0-5 V electronic signal (O/E converter; Siemens Healthcare, Malvern, PA). The LV pressure was obtained using a pressure

transducer (Mikro-Tip; Millar Instruments, Houston, TX) and connected to a transducer amplifier (Millar Instruments, Houston, TX). The 0-5 V LV pressure and radiofrequency pulse timing were digitized at 2 kHz with a manifold analog to digital converter (NI USB6009 Multifunction DAQ, National Instruments, Austin, TX), and recorded (LabView; National Instruments, Clearwater, FL).

9.3.6: Wall Thickness Estimation and Regional Loop Area

Wall thickness (WT) over time was calculated based on epicardial and endocardial point pairs manually selected along the circumferential direction of a short-axis image. Regional Loop Area was calculated by integration of the Pressure-Wall Thickness loop generated for different regions within a slice.

As described in Chapter 2, we have utilized the time-varying elastance model for cardiac tissue in this dissertation. With this approach, we expect to find that normal myocardium during the inflow occlusion has: (1) increased end-diastolic wall thickness due to decreased loading and (2) decreased regional Loop Area via the Frank-Starling relation. Similarly, we expect infarcted tissue will show (1) dampened wall thickening due to decreased number of contracting fibers during contraction and (2) limited increase in end-diastolic wall thickness due to its passive tissue properties during the preload reduction. The properties of the borderzone are expected to vary along this spectrum based on the extent of regional dysfunction.

By performing real-time MRI imaging with regional wall-thickness tracking during a preload occlusion experiment, we obtained regional Pressure-Wall Thickness loops and quantified Loop Area as a function of loading conditions.

Linear fits of the Loop Area as a function of end-diastolic wall thickness provided a regional Frank-Starling-type of relation. Normal myocardium should demonstrate a negative relationship that is linear (Loop Area decreases as the wall thickness increases). Infarcted tissue should have a “flatter” relationship with decreased correlation between work and loading conditions due to predominantly passive properties.

9.4: Results

9.4.1: Comparison of Motion-Tracking Methods

The Dice score after motion-tracking was used to evaluate the success of the motion-tracking algorithm. The image below illustrates a successful motion-tracking algorithm where the changes in Dice coefficient from cardiac motion prior to registration are eliminated.

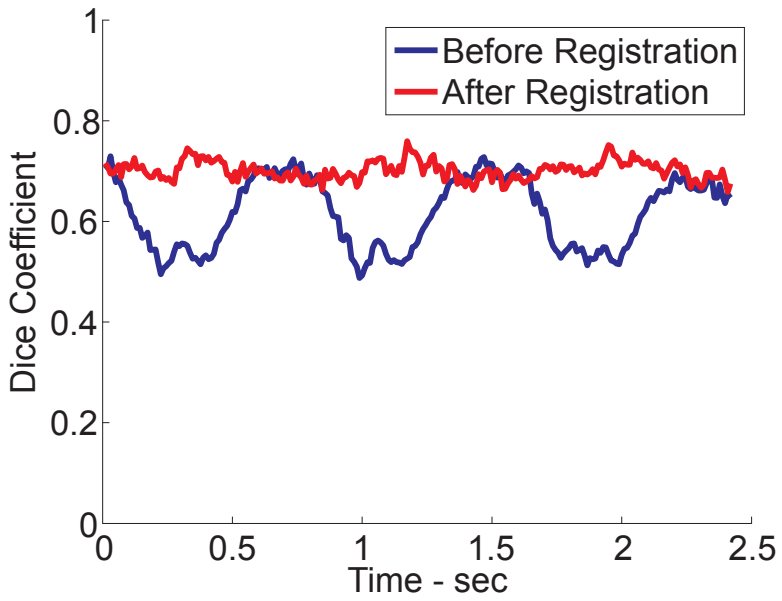

Figure 9.4 Dice Coefficient as a Function of Time Before and After Registration. Adapted from (120)

The average Dice score and the standard deviation in the Dice score across 9 patients was calculated and compared to the pre-registration values.

The values across the 9 patients outlined several key results. First, the Optical Flow method provided the highest Dice scores after registration (coupled with the smallest standard deviation). Furthermore, the optical flow method was the fastest implementation. As a result, Optical Flow was utilized in the animal portion of the wall thickness measurement.

Second, the use of a template (either the initial frame or the normtemplate) provided improved results in comparison to the sequential registration. The accumulation of errors in the sequential approach made it likely to fail, especially considering the large number of images that are consecutively registered.

Calculation of the normtemplate however, introduces several factors into the estimation of wall thickness. First, the normtemplate has to be calculated which is a time-consuming process. Furthermore, the template generation needs to be successful and not converge on a smoothed or anatomically inaccurate result. Based on our results, we did not see an improvement in the Dice coefficient in the normtemplate approach over the initial frame. As a result, the simplest approach (initial frame registration with Optical Flow) was utilized for the subsequent wall thickness measurement in animals.

9.4.2: Regional Wall Thickness Tracking

Wall thickness obtained using motion-tracking of real-time MRI in an infarct model demonstrate regional differences in thickening at rest ($t < 10$ seconds) as well as during the previously described preload occlusion experiment ($t>10$ seconds). A phase-sensitive inversion recovery (PSIR) MRI acquisition was utilized to identify infarct regions via hyperintense signal intensity and normal myocardium (green), borderzone (orange), and infarct (red) tissue regions were denoted for regional analysis (Figure 9.5).

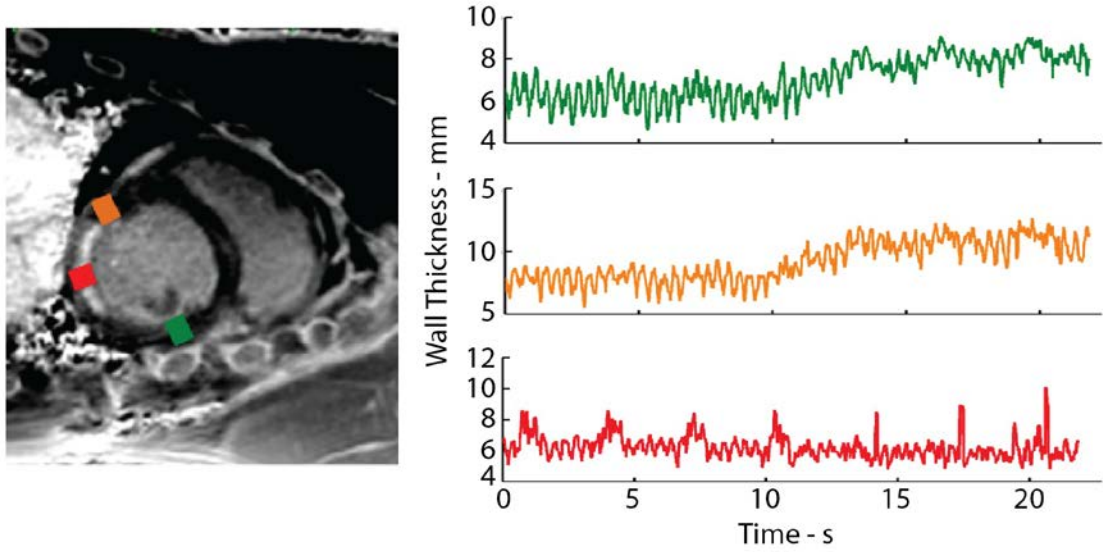

Figure 9.5 Regional Wall Thickness During Preload Occlusion. Difference in wall thickness prior to and during inflow occlsuion can be observed in the normal (green), borderzone (orange), and infarcted (red) myocardium. Adapted from (124)

The wall thickness plots over time demonstrate regional differences in function. Specifically, normal myocardium demonstrates large changes in wall thickness with contraction and the preload occlusion (t>10 seconds) causes a thickening that corresponds with the unloading of the heart. As the heart unloads, the walls thicken and the amplitude of the contraction decreases. The infarct shows markedly diminished contraction amplitudes and does not respond to the preload occlusion. The deflections observed every 2-3 seconds are due to respiratory motion. The borderzone appears to show a dampened contraction pattern but demonstrates an unloading pattern similar to normal myocardium.

9.4.3: Estimation of Regional Loop Area and Frank Starling Relations

Synchronizing the wall thickness measurement to the LV pressure allows for estimation of regional Loop Area. Measuring regional Loop area during a preload occlusion allows for the development of regional Frank-Starling relations by plotting the measured loop area vs. end-diastolic wall thickness (EDWT). These plots demonstrate regional differences in function.

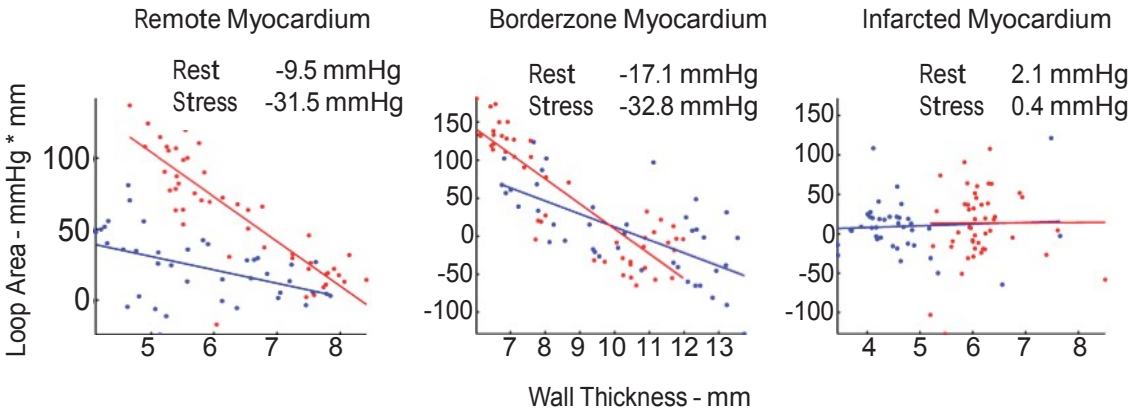

Figure 9.6 Regional Loop Area as a Function of End-Diastolic Wall Thickness. Remote (healthy) myocardium demonstrates positive Loop Area at rest, a linear decrease during the occlusion, and a shift with inotropic agent. Infarcted myocardium does not demonstrate the same response and the borderzone function appears imparied. Adapted from (124)

The normal myocardial tissue (left) showed a positive regional Loop area (~50 mmHg mm) prior to the preload occlusion. The preload occlusion decreased the amount of work performed as the end-diastolic wall thickens (blue fit). Inotropic infusion (red points) increased Loop Area at rest (> 100 mmHg mm) and increased the slope of the linear fit (31.5 mmHg vs. 9.5 mmHg). The infarcted tissue (right) has regional Loop Area values centered at 0 at rest and did not demonstrate a change with preload occlusion (slope of linear fit nearly flat). The inotropic infusion caused a rightward shift of the points

(meaning the wall thickened) but there is no upward shift of the regional Loop Area. Furthermore, there is no relationship associated with the preload occlusion experiment. The borderzone demonstrates regional Loop Area that is close to normal prior to the preload occlusion (~ 50 mmHg mm). Furthermore, the preload occlusion shows a decrease in regional Loop Area with preload occlusion. The regional Loop Area measured at the end of the preload occlusion is negative which implies the borderzone has stop contributing to contractile function and now has worked being performed on it (by the rest of the myocardium). Inotropic infusion caused an increase in the slope (to a value similar to that since in normal myocardium 32.8 mmHg). However, this is a dampened response relative to the baseline slope (17.1 mmHg).

9.5: Discussion

9.5.1: Motion Tracing Methods

The success of Optical Flow (relative to more advances registration methods) may be partly attributed to the simplicity of the Optical Flow technique. The only parameter required is a weighting term that balances the matching of image intensity with the divergence of the displacement field. More advanced methods such as b-spline registration or ANTS diffeomorphic approaches typically require tuning and calibration. It is likely that these methods may surpass the success of Optical Flow after a more robust tuning of the method-specific parameters.

The speed of the optical flow method makes it appealing for this application due to the large number of registrations necessary. Therefore, subtle improvements via temporal

regularization were explored. Temporal regularization further constrains the registration. Initial attempts to introduce these constraints were pursued by Mohammed Shahid as part of the BE537 Biomedical Image Analysis in a semester-long project entitled *Temporal Regularization for Cardiac Motion Tracking*. The methods were then applied to real-time images of patients with ectopy (described in Chapter 10) and demonstrated regional differences in motion, presented as a poster entitled *Regional Alteration in Myocardial Contraction during Ectopy* at the 2015 University of Pennsylvania Pendergrass Symposium.

9.5.2: Regional Borderzone Function Assessment via Loop Area

The result demonstrate that the 2D real-time MRI technique holds the potential to obtain load-independent measures of borderzone function. However, before the method can be broadly utilized, several key validations need to be performed.

First, in these results, a remote piece of myocardium is used as the control for infarcted and borderzone tissue function. However, based on the results presented in Chapter 8 regional variations in function are likely due to variations in anatomical tethering, stress patterns, and native differences in myocardial contractility, As a result, a thorough understanding of regional variations in Loop Area prior to infarction is necessary. Real-time imaging data during preload occlusions at multiple slice locations in non-infarcted animals was acquired as part of the sheep study outlined in Chapter 8. This data is being processed to generate an atlas or map of baseline regional function.

Furthermore, the temporal changes that occur during the LV remodeling process observed with this method should match those observed via ex-vivo material property characterization (125,126). The dataset referenced above also includes imaging performed 1-week and 4-weeks after myocardial infarction, which would allow for the temporal changes to be observed.

Finally, characterization of the borderzone everywhere around the infarct (in 3D) is necessary. In addition to scanning multiple slices, this approach could be adapted to provide information in the long-axis via long-axis slice orientation, decreased gap between slices, and eventually, 3D imaging. However, these approaches result in substantial changes to the image acquisition and processing pipeline and are beyond the scope of this project.

9.6: Conclusions

We found evidence of depressed regional work density in the peri-infarct borderzone and a differential effect of loading conditions. Evaluation of the borderzone function is critical for the development of novel treatments to prevent heart failure. The presented method allows for evaluation of regional work density and loading conditions with high spatial and temporal resolution. This can aid development of novel medical therapies by improving the understanding of borderzone physiology during infarct remodeling.

Chapter 10: Quantification of LV function pre, during, and post premature ventricular complexes reveals variable hemodynamics

10.1: Abstract

Premature ventricular complexes (PVC) are prevalent in the general population and are frequently associated with reduced ventricular function. Current echocardiographic and cardiovascular magnetic resonance imaging (CMR) techniques do not account for data acquired during PVCs and do not adequately address the effect of PVCs on global function.

Twelve subjects with a history of PVCs undergoing CMR were imaged using a recently validated real-time CMR imaging technique, which allows for real-time slice volume quantification. Two subjects had imaging repeated to observe changes in function with different ectopic patterns. Synchronization of real-time imaging with patient ECG allowed for different beats to be categorized by the loading beat RR-duration and beat RR-duration. For each beat pattern, global volumes were quantified and temporal averages were obtained using the frequency of each beat pattern.

Two subjects did not have any PVCs during the imaging session despite a history of frequent PVCs and 2 subjects had very infrequent PVCs. As a result, a single beat pattern (sinus rhythm) was observed across all slice locations in these four studies. The remaining subjects had different patterns of ectopy including isolated PVCs, bigeminy,

trigeminy, and interpolated PVCs. Global functional measurement of the different beat patterns based on timing demonstrated differences in stroke volume and cardiac output associated with different beat clusters. A temporal average of function was quantified for each subject depending on the frequency of each observed beat pattern.

Application of a novel real-time CMR imaging technique to patients with PVCs revealed differential contribution of PVCs to hemodynamics depending on timing and frequency. Use of the technique may provide insight related to PVC-associated symptoms and induced cardiomyopathy.

10.2: Introduction

Premature ventricular complexes (PVCs) are early depolarizations originating in the ventricular myocardium. The association of mechanical contraction with electrical depolarization is not guaranteed. Idiopathic PVCs may create variable symptoms and even cause a cardiomyopathy if the burden is sufficiently high. Clinically, PVC-induced cardiomyopathy remains a diagnosis of exclusion and conventional imaging is often employed to rule out underlying disease (127).

Accurate assessments of left ventricular (LV) function using echocardiography and cardiovascular magnetic resonance (CMR) examinations are hindered by the presence of frequent PVCs. In CMR, data acquired during multiple heartbeats is combined and arrhythmias can result in incorrect data synthesis leading to considerable image corruption (128). Recent improvements in real-time CMR have eliminated the need for synthesis of data acquired from multiple heartbeats and have allowed for observation of

each cardiac contraction and measurement of function slice parameters such as stroke volume (SV) and ejection fraction (EF) in a per beat fashion (76,85).

In this work, we present a novel method for evaluation of patients with PVCs using real-time MRI with imaging synchronized to electrocardiographic (ECG) recordings. The real-time imaging allows for each cardiac contraction to be observed and slice volume to be quantified. The synchronous ECG recording allows for multiple beat patterns to be characterized. For repeatedly observed beat patterns, slice volume values from multiple slices can be combined, leading to global volume measurements for each beat pattern.

10.3: Method

10.3.1: Patient Population

The prospective study was approved by the Institutional Review Board at the University of Pennsylvania and all subjects (n=12, 47.8 ± 24.3 years old and 33.3% male) gave written informed consent. PVC burden was quantified via the ECG synchronously recorded during MRI acquisition. 2 subjects had no PVCs during the CMR exam despite a history of frequent PVCs. 10 patients had PVCs during real-time CMR (burden 28 ± 14%, range 4-50%) and they demonstrated a range of arrhythmic patterns including bigeminy, trigeminy, and interpolated PVCs. Two of the 10 subjects (#4 and #5) were imaged twice. #4 was imaged pre and post PVC ablation and #5 had two different PVC burdens and ectopic patterns during two imaging sessions.

10.3.2: CMR Acquisition

CMR was performed on a 1.5 T imaging system (Avanto, Siemens Healthcare, Erlangen, Germany) equipped with nominal 40 mT/m magnetic field gradients, body RF transmit and a 32-channel, anterior and posterior RF receiver array.

Real-time data was obtained using a 2D, multi-slice, free-breathing bSSFP sequence with a golden-angle radial trajectory with the following imaging parameters, TE = 1.4 ms, TR = 2.8 ms, number of radial k-space data = 128, FOV = 220 mm - 300 mm, pixel size = 1.72 – 2.34 x 1.72 – 2.34 mm, bandwidth = 1000-1221 Hz/pixel, slice thickness = 8 mm, slice spacing = 10 mm, and k-space sampling according to the golden-angle $\Phi = 111.25°$. Imaging was performed in the short axis of the left ventricle. 6000 - 8000 radial projections (16 - 22 seconds) per slice were acquired.

10.3.3: Image Reconstruction and Slice Volume Quantification

The real-time image reconstruction and slice volume quantification methods have recently been validated in animal as well as clinical patients (76,85). Briefly, image reconstruction was performed using a non-Cartesian SENSE algorithm in open-source software (45,47,59). Quantification of real-time images was performed through user-initialized active contour segmentation which has been shown to provide slice volume values comparable to manual segmentation using clinical tools (76). 2D image data was arranged in a 3D stack Nx x Ny x Nt in open-source software (ITK-SNAP, University of Pennsylvania, Philadelphia, PA) with a typical size 192 x 146 x 6,000 (60). Intensity thresholding was used to generate a set of feature images of the LV intraventricular

volume. Ventricular segmentation was initialized using a 3 x 3 x Nt pixel column centered in the ventricle and 3D active contour segmentation was performed using region competition with user-defined balloon and curvature forces (87). This arrangement yields temporally consistent and smooth LV slice volume estimates. Papillary muscles were excluded from the segmentation using the feature image and manual correction. The basal slice was determined by identification of the slice with mitral valve annular plane at end-systole. LV slice volume was quantified from segmented data using the pixel size and slice thickness.

10.3.4: ECG Recording and Synchronization

Conventional cine CMR acquisitions require cardiac phase information to accurately sort the acquired data. As a result, robust 3-lead ECG acquisition, filtering, and real-time display are standard on clinical MRI scanners. For this work, we implemented a logging algorithm to capture the ECG signal acquired during the imaging experiment and it was synchronized to the CMR data using TCP/IP commands. This results in synchronization between the ECG signal, real-time MRI image frames, and derived slice volume estimates as shown in Figure 10.1. As a result, ECG information was utilized to synchronize slice volume data across slices.

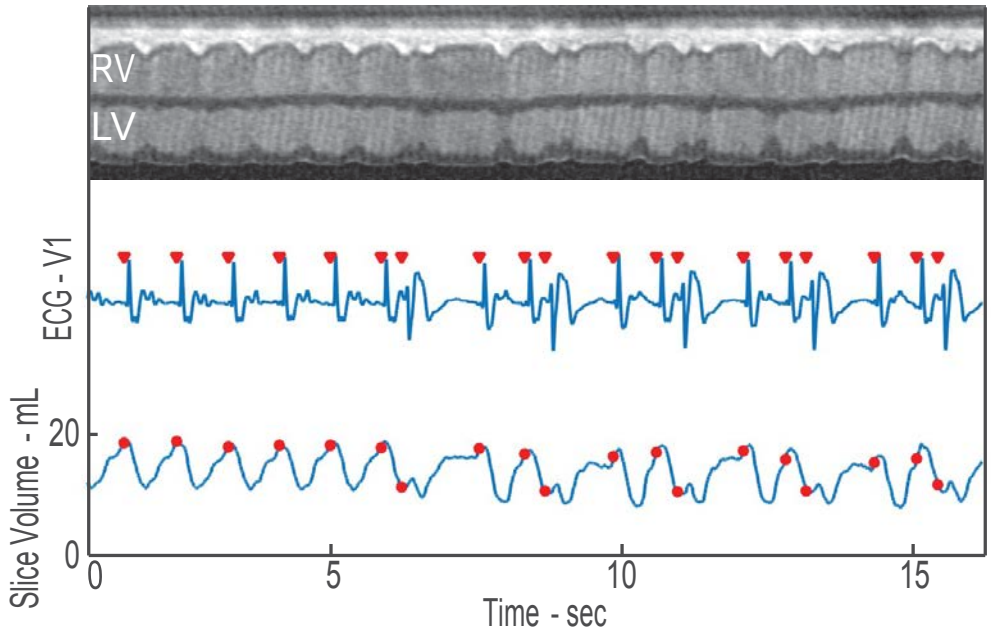

Figure 10.1 Synchronized real-time MRI imaging and ECG. Top row shows a projection through the heart where the contraction of the left ventricle in sinus and during arrhythmia can be observed. Quantification of slice volume (bottom row) allows for observation of the change in slice function due to arrhythmia. Adapted from (129).

10.3.5: Categorization of Beat Patterns and Global Volume Estimation

Beat patterns were identified and categorized based on two measured RR-durations. QRS detection was obtained via Pan-Tompkins algorithm implemented in Matlab (Mathworks, Natick MA) (130). As shown in Figure 10.2, plotting the RR-duration of the prior (loading) beat versus RR-duration of the subsequent beat allowed for clustering of distinct beat patterns. Specifically, in sinus rhythm, a single cluster is observed (Figure 10.2A). In patients with infrequent PVCs, the clustering acts as robust arrhythmia rejection as only the sinus rhythm beats are sampled across all slices (Figure 10.2B).

Multiple beat patterns result in multiple clusters and when a cluster is observed across all slice locations, global volume quantification can be performed (Figure 10.2C).

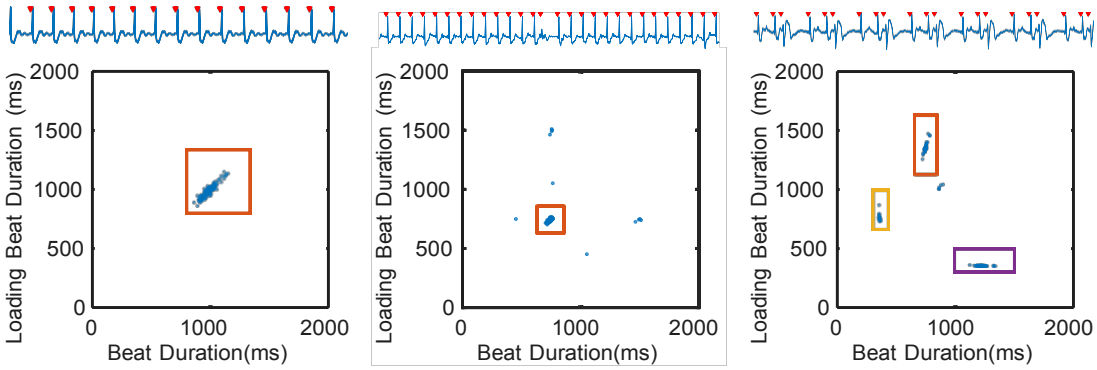

Figure 10.2 2D RR-duration. Grouping of beat types based on current beat duration and loading (previous beat) duration. On the left, a patient with sinus rhythm is shown with a single slice ECG and one 2D cluster. In the middle, a patient with infrequent PVCs demonstrates how the algorithm can be used to provide arrhythmia rejection. On the right, a patient in trigeminy exhibits four beat clusters. Three clusters (with colored boxes) were observed at all slice locations. The remaining cluster (sinus-sinus) was only observed at a single slice location and is therefore excluded from further analysis. Adapted from (129).

For each ectopic contraction, there is a potential for four distinct beat patterns to be observed via the 2D clustering of loading RR-duration and beat of interest RR-duration. The four beat patterns can be described in a sequential order. First, during normal sinus rhythm there are two normal duration RR-intervals: normal loading beat RR and normal beat of interest RR. Second, when a PVC occurs during sinus there is a normal loading beat RR followed by a short RR due to the premature depolarization. Third, after the PVC there is a short RR as a loading beat followed by a long RR for the beat of interest (due to the typical compensatory pause post-PVC). Finally, as there is a transition back to sinus rhythm, there is a long RR (compensatory pause) as the loading beat followed by a normal RR for the beat of interest. In any particular patient, not all four beat patterns

may be present or distinguishable using this 2D clustering with loading RR-duration and beat RR-duration. For example, in regular trigeminy, the pair of regular RR intervals (sinus-sinus-sinus) pattern does not occur. Similarly in bigeminy, only an interrupted sinus and PVC beat are observed, resulting in only two patterns: short-long RR and long-short RR. Even in irregular ectopic patterns where all four beat patterns occur, identification of these beat patterns based solely on two RR-durations may result in some beat patterns being classified together due to negligible differences in pre-load durations and beat durations.

Slice volumes observed for each beat pattern were combined to generate global estimates of LV volume. To account for small variations in RR-duration, non-linear beat duration normalization was performed (88). A particular beat pattern resulted in global volume estimates only if the beat pattern was observed at all LV slice locations. If a particular beat pattern was observed multiple times in a single slice, the median value was used for global volume estimation.

10.3.6: Quantification of Beat-by-Beat Function

Global end-diastolic volume (EDV), end-systolic volume (ESV), SV, and EF were quantified for each observed beat pattern. The prevalence of each pattern was used to obtain a temporally averaged estimate of function depending on the frequency of each beat pattern.

10.4: Results

In 4 subjects (Table 1, Patients 1-3 and 4 Post Ablation), only one beat pattern (sinus rhythm) was observed across all slice locations and thus one mode of ventricular volume and function was quantified (Figure 10.3). These subjects were in sinus rhythm despite having a history of frequent PVCs (n=2) or had infrequent PVCs (n=2, 4% and 8% PVC burden, subject 4 post ablation), which were not observed at all slice positions.

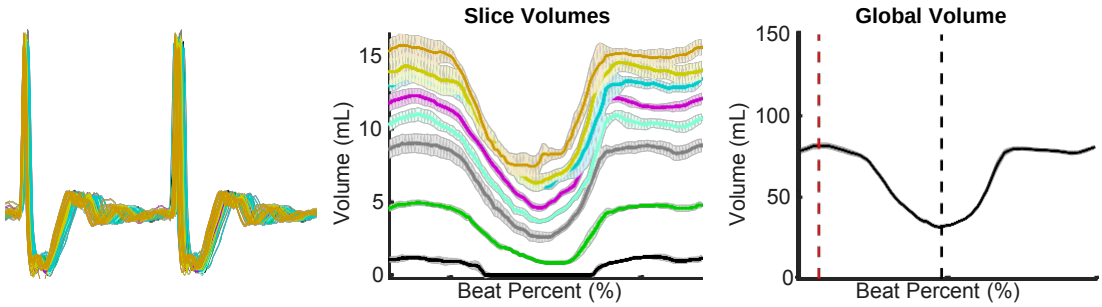

Figure 10.3 Global quantification of individual beat types. In a subject with sinus rhythm, there is temporal agreement in the duration of the loading beat as well as the beat of interest in the 2 beat ECG (left). Slice volumes for the second beat are shown across the LV (middle) and summed to obtain the global volume curve (right). The global volume curve shows a normal contraction pattern and demonstrates a small increase in global volume due to atrial contraction. Adapted from (129).

Patient Number	Age	Sex	Patient Info Arrhythmia Pattern	PVC Prevalence	Beat Pattern	Volumetric Measures EDV (mL)	SV (mL)	EF (%)	Beat Frequency	Temporal Average EF (%)
1	31	F	History of PVC	0%	Sinus	81.1	44.0	54.3	N/A	
2	22	M	History of PVC	0%	Sinus	143.1	55.2	38.6	N/A	
3	90	F	PVC	4%	Sinus	152.3	59.3	38.9	N/A	
4	19	F	Irregular Bigeminy	41%	Interrupted Sinus	162.2	59.3	36.5	11%	23.0
					PVC	145.6	24.0	16.5	22%	
			Post Ablation	8%	Sinus	170.7	60.1	35.2	N/A	
5	28	F	Bigeminy	50%	Interrupted Sinus	123.7	67.9	54.9	44%	48.7
					PVC	125.8	53.3	42.4	43%	
			PVC	40%	Post-PVC Sinus	84.9	52.9	62.2	19%	50.1
					Interrupted Sinus	102.3	63.2	61.8	32%	
					PVC	77.4	23.5	30.4	30%	
6	51	M	Trigeminy	33%	Post-PVC Sinus	126.9	88.2	69.5	29%	44.5
					Interrupted Sinus	132.8	67.0	50.5	31%	
					PVC	62.5	9.6	15.3	31%	
7	58	M	Interpolated PVC	19%	Sinus	126.8	54.0	42.6	47%	36.3
					Post-PVC Sinus	94.4	32.7	34.6	13%	
					Interrupted Sinus	124.3	49.2	39.6	16%	
					Interpolated PVC	100.0	14.0	14.0	14%	
8	59	F	PVC	35%	Post-PVC Sinus	83.9	61.7	73.6	39%	69.1
					Interrupted Sinus	85.5	63.1	73.9	13%	
					PVC	38.8	20.2	52.1	14%	
9	42	F	Irregular Trigeminy	33%	Post-PVC Sinus	65.8	42.6	64.8	22%	61.7
					Interrupted Sinus	72.5	45.1	62.3	29%	
					PVC	62.7	35.6	56.9	18%	
10	56	F	PVC	24%	Sinus	104.9	56.7	54.1	44%	54.9
					Post-PVC Sinus	108.3	75.3	69.5	10%	
					Interrupted Sinus	122.4	66.6	54.4	15%	
					PVC	73.6	35.1	47.7	14%	
11	90	M	PVC	14%	Post-PVC/Sinus	126.6	65.1	51.4	69%	47.4
					Interrupted Sinus	127.1	65.5	51.5	9%	
					PVC	66.9	7.8	11.6	9%	
12	27	F	PVC	13%	Post-PVC/Sinus	87.2	49.0	56.2	64%	50.8
					Interrupted Sinus	99.2	57.5	58.0	12%	
					PVC	63.2	8.7	13.8	12%	

Table 10-1 Beat characteristics, volumetric measures, and weighted average of study subjects. Adapted from (129).

The remaining 8 subjects had frequent PVCs during imaging (13 - 50%). Subject 5 was imaged twice and was in regular bigeminy during the first real-time MRI. As a result, two beat patterns were observed (Figure 10.4). The lower EF of the PVC is a result of less effective contraction with similar loading volume as sinus, but higher ESV. During the second imaging session, the same subject had frequent PVCs (40%) without a regular pattern. The PVCs were less effective than the PVCs while in bigeminy and contributed to half of the SV compared to normal depolarization beats (23.5 ml vs. 52.9 ml). Despite the difference in ectopic patterns at different time points, the temporally averaged EFs were similar (48.7% vs. 50.1%) in the two imaging sessions.

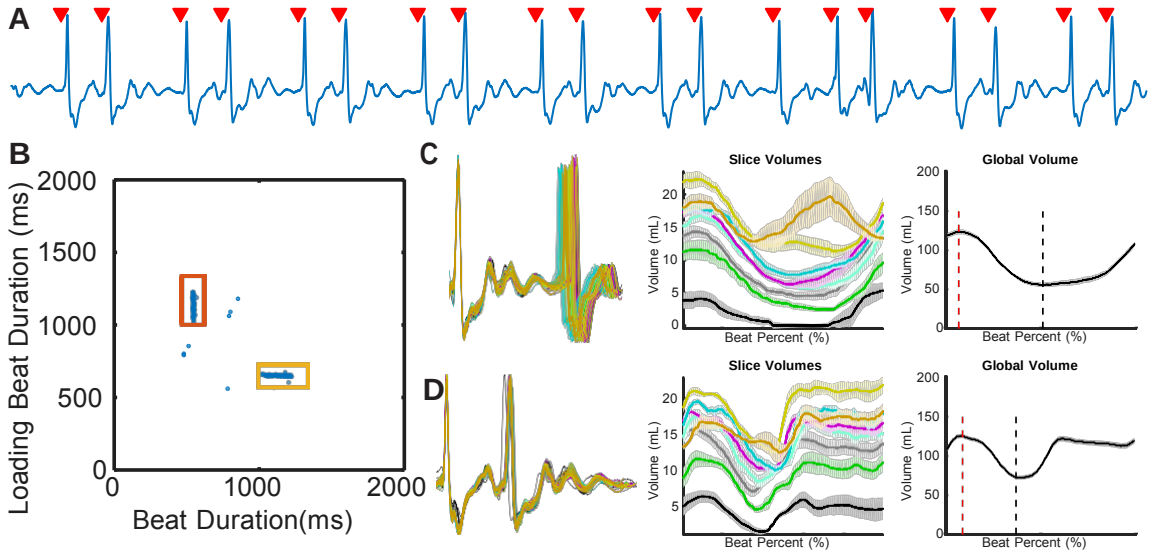

Figure 10.4 LV function of a subject with bigeminy. A representative ECG (**A**) from a single slice demonstrates the bigeminy pattern. Two beat clusters are observed in the 2D plot of beat duration (**B**). As a result, two different global patterns can be quantified in **C** and **D**. Corresponding global volume measurements are found in Table 1 (Patient 5). Adapted from (129).

Subject 6 was in regular trigeminy during the real-time MRI, which resulted in 3 beat clusters (Figure 10.5). In addition to the PVC, the 2D RR-duration plot allowed for the

interrupted sinus cluster to be quantified separately from the post-PVC sinus and sinus-sinus cluster, shown in Figure 10.5C and D. ESV associated with the post-PVC sinus is lower than the interrupted sinus (38.7 ml vs. 65.8 ml) which results in a higher calculated EF (69.5 vs. 50.5%). The PVCs (Figure 10.5E) in this pattern had a small stroke volume (9.6 ml). As a result, this patient demonstrated two productive contractions (interrupted sinus and post-PVC sinus) with one relatively unproductive contraction (PVC).

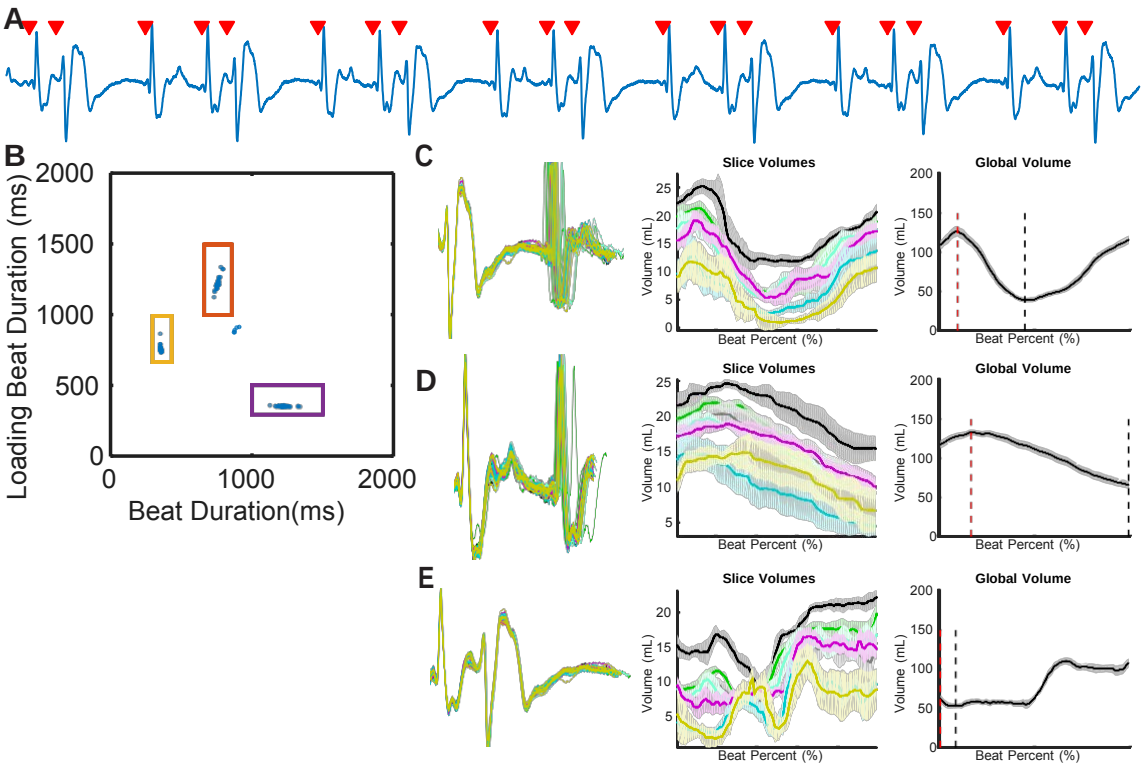

Figure 10.5 LV function with trigeminy. Three beats (post-PVC, interrupted sinus, and PVC) can be observed in the ECG (**A**). This leads to three distinct clusters and varying global volume measurements (**B** - **E**). Global volume measurements are found in Table 1 (Patient 6). Adapted from (129).

Subject 7 had interpolated PVCs during the image acquisition (Figure 10.6), which resulted in a unique pattern not described above. In an interpolated PVC, the PVC is an

‘extra’ depolarization in between sinus activity, which does not change the P wave to P wave duration: in this case, there are two short RR intervals occurring sequentially. Our results demonstrate that this type of PVC can be observed using the 2D RR-duration plot. The loading volume for the post-PVC sinus contraction (94.4 mL) decreased relative to normal sinus beats (126.8 mL). The post-PVC contraction resulted in a decrease in EF (34.6 vs. 42.6 %). Furthermore, the PVC did not result in substantial SV (14.0 mL). As a result, interpolated PVCs resulted in a decreased SV in the PVC and post-PVC beats. Therefore, the extra systole not only did not contribute to cardiac output but also impaired the post-PVC sinus contraction by reducing preload for that beat.

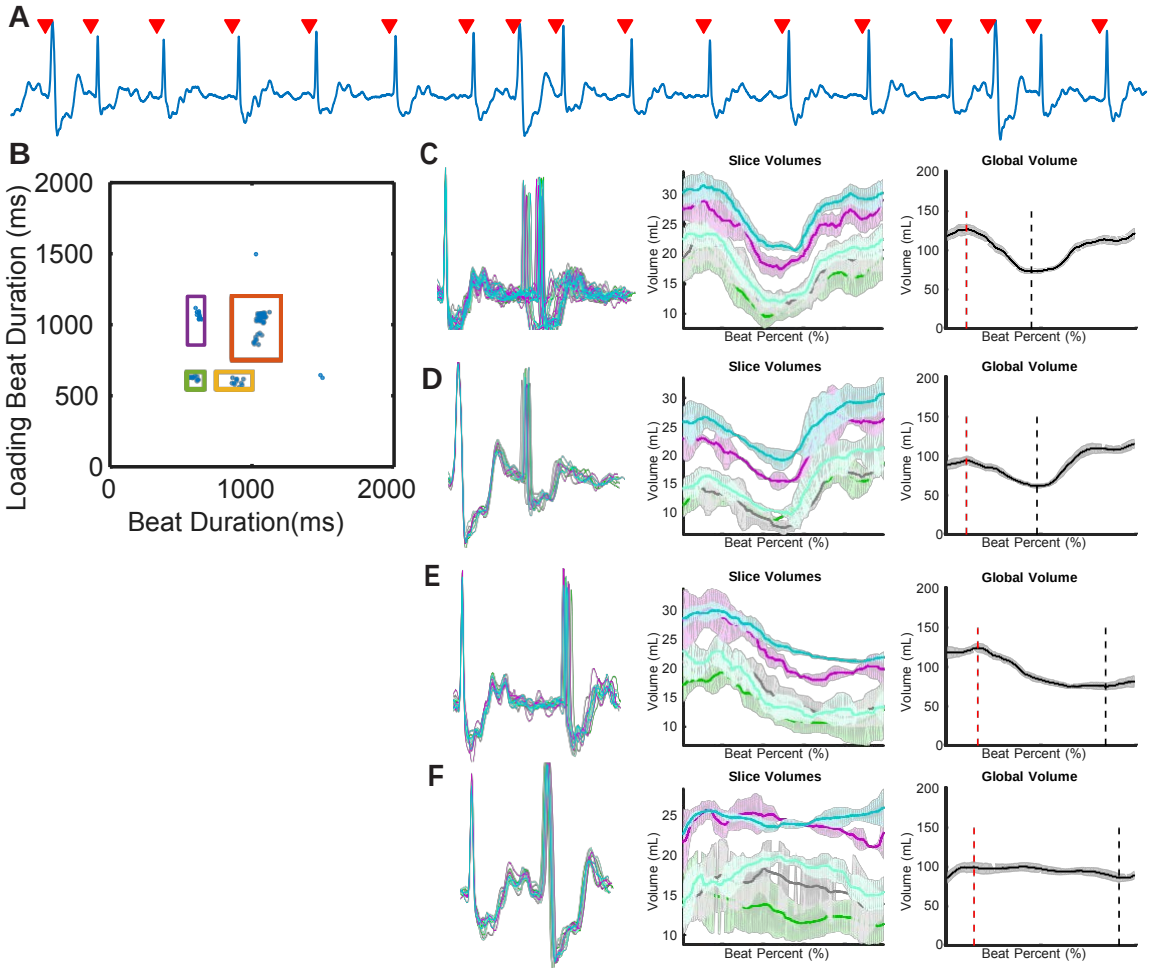

Figure 10.6 LV function with interpolated PVCs. The ECG (**A**) and 2D plot (**B**) depict 4 beat patterns: sinus rhythm (**C**), post-PVC sinus (**D**), interrupted sinus (**E**), and the interpolated PVC contractions (**F**). Global volume quantification suggests interpolated PVCs affect post-PVC loading and do not result in substantial stroke volume. Global volume measurements are found in Table 1 (Patient 7). Adapted from (129).

Subjects 8-12 and subject 4 prior to ablation had a variety of patterns including periods of bigeminy and trigeminy, as well as PVCs late in diastole. The different arrhythmia patterns resulted in different number of beat patterns being observed, which is quantified in Table 1. Amongst the 12 subjects, if we consider the “true” LV function to be represented by the “normal depolarization” beats including sinus, interrupted sinus, and

post-PVC sinus beats, then subjects 5, 6, 8, 9, 10, and 12 would have “normal” function. Their burden of PVCs measured by PVC frequency was not significantly different from the remaining subjects with “abnormal” LVEF ($p=0.25$). If we instead consider the average EF of all beats as the representation of LV function, only subjects 8 and 9 are normal. These two subjects had high burdens of PVCs (35% and 33%) but also had the 2 latest occurring PVCs (675 ms and 766 ms after the previous QRS, respectively) and therefore these PVCs produced stroke volumes that were similar to sinus beats, which limited the hemodynamic impact.

To understand the relationship of PVC timing to stroke volume produced by the PVCs, we plotted the SV of the PVC (normalized to the maximum SV observed in that subject) versus timing of PVC (normalized by the duration of sinus beats in the same subject) as shown in Figure 10.7. The SV of PVC is linearly correlated to the timing in the cardiac cycle (linear fit: slope = 0.74, y-intercept = 2.38, R^2 = 0.20, correlation coefficient = 0.452).

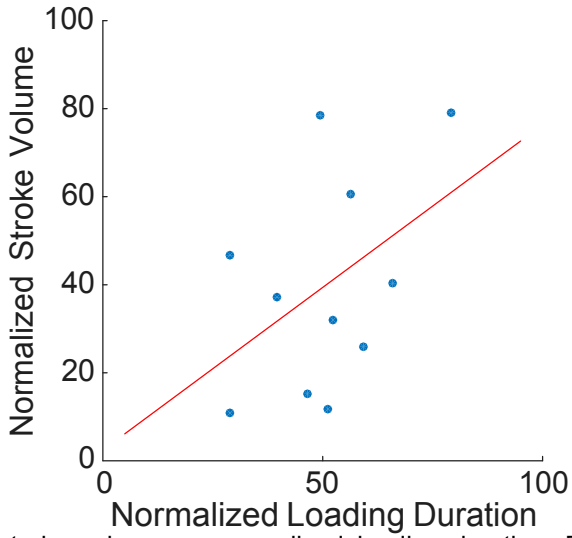

Figure 10.7 Normalized stroke volume vs. normalized loading duration. For patients with ectopic contractions the normalized stroke volume (percentage of maximum observed stroke volume) was plotted as a function of normalized loading duration (percentage of loading duration for sinus contraction). Adapted from (129).

10.5: Discussion

A variety of mechanisms have been proposed for PVC-induced cardiomyopathy including hemodynamic impairment, alterations in heart rate, vascular autonomic dysregulation, increased oxygen consumption, ventricular dyssynchrony, tachycardia-induced cardiomyopathy, or alterations in calcium and ionic currents (127), but it remains unclear which of these factors are the most relevant. We utilized a novel method to assess the hemodynamic contribution of PVCs and detailed their hemodynamic impact on the adjacent sinus depolarizations. Our findings suggest that different PVC patterns contribute differentially to the hemodynamics of the cardiac contractions, impacting adjacent sinus depolarizations depending on their timing, frequency, and location.

In assessing LV function in the presence of PVCs, there is currently no other published method to assess the volumes and functions of PVCs in addition to sinus contractions. Echocardiography, which has been used in evaluating patients with suspected PVC-induced cardiomyopathy, ignores PVCs in situations other than bigeminy (in which case sinus beats and PVC beats are averaged) (131). In CMR, arrhythmia rejection is usually employed to isolate sinus contractions. In this work, we have presented a novel method to assess LV function in patients with frequent ventricular rhythm disturbances. We describe the volumetric values (EDV, ESV, SV, and EF) for each observed beat pattern, prevalence (percentage of total beats) for each pattern, and temporally weighted averages for each measure.

It has long been recognized that PVC burden is only one of the many factors contributing to impairment of LV systolic function (132,133). PVC interpolation has been identified as an additional independent predictor of PVC-induced cardiomyopathy but the hemodynamic mechanism was not elucidated (134). In our study, we observed that a patient in regular bigeminy had two distinct beat patterns that both contributed substantial stroke volume. However, patients with other PVC patterns including trigeminy and interpolated PVCs demonstrated low stroke volume beat patterns. Furthermore, in the case of interpolated PVCs, the function of a post-PVC contraction was also impaired, which is previously unreported. Using this method, we can start to explore the difference between productive PVCs (contribute significantly to hemodynamics, such as demonstrated in subjects 5, 8, 9, 10), and non-productive PVCs (contractions that contribute minimally to cardiac output) in subjects 4, 6, 7, 11, and 12. This differential

contribution to hemodynamics compounded by PVC frequency may be more important than frequency alone. For example, subject 5 has 40-50% PVCs, but all PVCs were productive compared to subject 4 who has 41% of PVCs and those PVCs were not productive. A lower frequency of non-productive PVCs, as demonstrated in subjects 11 and 12, may be less detrimental, as there is a smaller impact on hemodynamics with temporally averaged EF (Table 1, last column).

The relationship between the timing of the PVC (in diastole) and the productivity (in terms of stroke volume) was explored in Figure 7. It appears that the later the PVC occurs in diastole, the higher the stroke volume. Another study also reported the PVC coupling interval ≤600 ms had a lower mean LVEF (135). However, this Frank-Starling-type response may be affected by several factors including the origin of the PVC, the level of dyssynchrony associated with the PVC contraction, and the degree of underlying cardiomyopathy. This may account for how subject 5's PVCs were productive and occurrred earlier (RR = 530 -560 ms) than in subject 4 (RR = 666 ms) whose PVCs were unproductive, despite a similar prevalence and a later occurrence.

Our method provides information regarding the hemodynamic and possibly energetic consequences of different PVC contraction patterns. The difference between productive and nonproductive PVCs may have direct consequences from an energetic perspective since ATP is consumed during each depolarization. PVC beats with no or little stroke volume result in 'wasted' ATP and thus decreased myocardial efficiency. Our approach provides a quantitative tool to better understand the impact of PVCs on cardiac physiology.

In the patients with infrequent PVCs, our approach provides quantification similar to clinical CMR acquisitions with arrhythmia rejection where only the predominant contraction mode is observed. In itself, this method is a more robust arrhythmia rejection technique as current arrhythmia rejection can fail in several ways. First, conventional arrhythmia rejection utilizes the RR-duration to categorize beats and may have variable success depending on the ectopic morphology and frequency. Second, if the RR-duration acceptance window is too small, a high rejection rate will lead to prolonged breathholds and the potential for respiratory motion corruption. Third, not all PVC beats are reliably detected by the vector ECG since depolarizations can sometimes resemble a T-wave. Using the real-time imaging technique, our approach is not sensitive to any of these failure modes.

Recently, animal models with PVC pacing have been developed to try to understand myocardial dysfunction caused by PVCs (136,137). These models have found changes in global LV dimensions and function after 2-4 weeks of pacing with bigeminy that were programmed with a short coupling interval. Huizar et al also found that the remodeling associated with the PVCs is reversible and microscopic evaluation did not yield any changes in inflammation, fibrosis, apoptosis, or mitochondrial oxidative phosphorylation (137). Huizar postulates that postextrasystolic potentiation which causes increased intracellular calcium and myocardial oxygen consumption might contribute to the development of cardiomyopathy. These animal models suggest that PVC can cause a reversible cardiomyopathy in structurally normal hearts but the question of what differentiates benign PVCs and myopathy-causing PVCs remains unanswered.

Our approach opens doors to elucidate the mechanisms of PVC-induced cardiomyopathy. First, the method allows for direct observation of hemodynamic impairment due to the PVCs in all heartbeats. In addition to the PVC burden during the MRI exam, the distribution of PVCs and the impact on hemodynamics can be directly measured. For example, a 25% PVC burden can be observed in two different ways: a patient can regularly have a PVC every fourth beat or the patient can spend 50% of the period in regular bigeminy. These two different mechanisms may present as having the same overall PVC burden but may lead to different impact on myocardial function, possibly through the impact on vascular regulation, oxygen consumption, and intra-cellular calcium and ionic currents.

There are several limitations to the study. First, the entire heart is acquired with a slice-by-slice 2D real-time imaging technique. In patients with infrequent PVCs, PVC might not occur at all slice positions, which limits the quantification of rare PVCs. In these instances, data from the rare PVCs is discarded and the quantitative values are similar to those obtained using conventional cine CMR with arrhythmia rejection. Future development of 3D real-time imaging or prolonged scans in these patients would allow for analysis of these infrequent PVCs.

A second limitation of this study is the potential impact of respiratory motion on measured cardiac function. We performed the real-time acquisition during free respiration to minimize the overall acquisition time. We did not use a respiratory window since it would reduce the number of observed beats and would compromise our ability to observe multiple beat patterns across slice locations. However, the potential effect of

respiratory motion is likely small because large variations were not present in the slice volume curves (as shown in Figures 3-6). Furthermore, recent publications indicate that the effect of respiratory position on LV volume quantification is negligible potentially due to a predominant in-plane as opposed to through-plane motion (138). Imaging during breathholds or selection of images based on respiratory motion could be employed in future studies to isolate the impact of respiratory motion.

It is believed that PVC-induced cardiomyopathy develops in a time-dependent fashion where the cumulative burden over time may play an important role (139). Future longitudinal work capturing the temporal progression of PVC-induced cardiomyopathy as well as changes in myocardial function associated with ablation therapy is needed.

10.6: Conclusions

We have presented a novel CMR-based method to assess LV function in subject with frequent ventricular ectopy, which provides volumetric assessment of multiple beat patterns. This method reveals that different PVC patterns contribute differently to hemodynamics depending on the timing and frequency of the PVCs. Our findings open the doors to accurate interrogation of the LV function during PVCs in each individual patient and may provide new insight into PVC-induced cardiomyopathy and symptoms associated with PVCs.

Appendix

Appendix 1: Moore-Penrose Pseudoinverse

One approach to solve for x in a linear system with observed signal s and a linear operator A with noise ε such as

$$s = Ax + \varepsilon \quad \text{[A1-1]}$$

is to find $\hat{x}$ which minimize the error measured as

$$\varepsilon = s - A\hat{x} \quad \text{[A1-2]}$$

This can be performed using the sum of squares of the error as the term to minimize. This is analogous to a least-squares fit.

$$SoS = \varepsilon'\varepsilon = (s - A\hat{x})'(s - A\hat{x}) \quad \text{[A1-3]}$$

This metric can be expanded and using the derivative, a minimum can be found

$$\begin{aligned} SoS &= \varepsilon'\varepsilon = (s - A\hat{x})(s - A\hat{x}) \\ &= s's - s'A\hat{x} - \hat{x}'A's + \hat{x}A'A'\hat{x} \\ \frac{\partial}{\partial \hat{x}} SoS &= -2A's + 2A'A\hat{x} = 0 \\ A'A\hat{x} &= A's \\ \hat{x} &= (A'A)^{-1}A's \end{aligned} \quad \text{[A1-4]}$$

Appendix 2: Iterative Solver Example

Below, an example of iterative solving using the gradient descent is adapted from Shewchuk. Although the iterative solvers used in this thesis utilize a conjugate gradient algorithm, the example demonstrates the steps involved in solving a linear equation and gives a flavor for the convergence of a solution.

In the example, we aim to solve a two-dimension linear system given by

$$Ax = b \text{ where } A = \begin{bmatrix} 3 & 2 \\ 2 & 6 \end{bmatrix} \text{ and } b = \begin{bmatrix} 2 \\ -8 \end{bmatrix} \qquad \text{[A2-1]}$$

This set of linear equations and the solution at $(2, -2)$ is shown on 2D plot below.

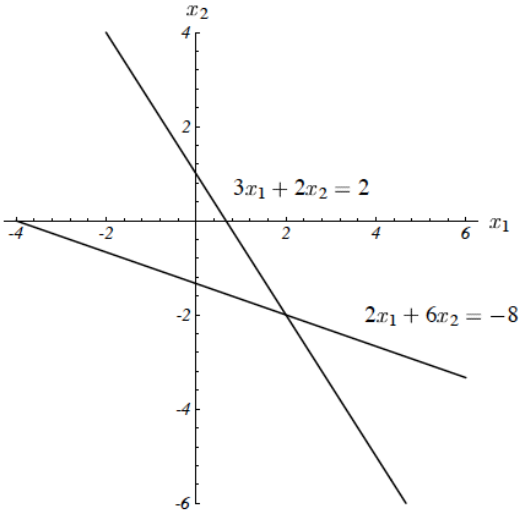

Figure A2-1 Plot of Linear System and Solution

First, a cost or energy function ψ is defined for a given a current estimate of the solution x where the minimum energy occurs at the desired solution. For symmetric and positive-definite A matrices, the solution to $Ax = b$ lies at the minimum of ψ when ψ takes the quadratic form

$$\psi(x) = \frac{1}{2}x^T Ax - b^T x + c \qquad \text{[A2-2]}$$

The value of this quadratic form in the 2D space is shown below

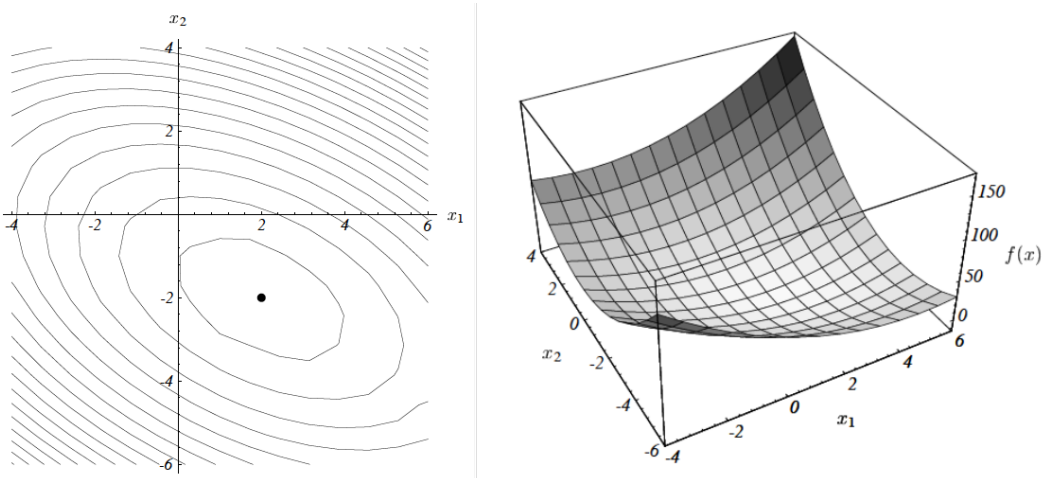

Figure A2-2 Visualization of Cost Function ψ for Example System

Given this energy function ψ, the goal of the iterative process is to proceed from an initial estimate x_0 to the location which minimizes ψ via a series of iterative steps. At each iteration, the size and direction of a particular step need to be calculated and performed. For the gradient descent approach, the direction of the step is based on the gradient of the energy function $\psi'(x)$.

For an n dimension system, this is described as

$$\psi'(x) = \begin{bmatrix} \frac{\partial}{\partial x_1}\psi(x) \\ \frac{\partial}{\partial x_2}\psi(x) \\ \vdots \\ \frac{\partial}{\partial x_n}\psi(x) \end{bmatrix} = \frac{1}{2}A^T x + \frac{1}{2}Ax - b \qquad \text{[A2-3]}$$

If A is symmetric, Equation A2-3 simplifies to

$$\psi'(x) = Ax - b \qquad \text{[A2-4]}$$

Setting the gradient to 0, we can obtain the same equation as in A2-1.

As mentioned above, the goal is to take a step in the steepest direction available to move down the parabola towards the minimum value. The direction of the steepest descent is the opposite of the gradient

$$-\psi'(x_i) = b - Ax_i \qquad \text{[A2-5]}$$

For the example shown above, the gradient is shown in the figure below.

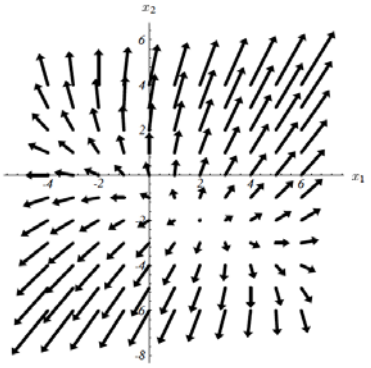

Figure A2-3 Visualization of Gradient of the Cost Function ψ' for Example System

At this point, it is useful to introduce two terms: error and residual. The error e_i indicates how far the current guess x_i is from the solution x and can be described as $e_i = x_i - x$. The residual r_i indicates how far we are from the correct value of b where $r_i = b - Ax_i = Ax - Ax_i = -Ae_i$. With this definition, the residual r_i is the direction of the steepest descent for a given x_i.

In the example presented above, if an initial guess of (-2,-2) is used, the direction of the steepest descent is shown below in a solid line.

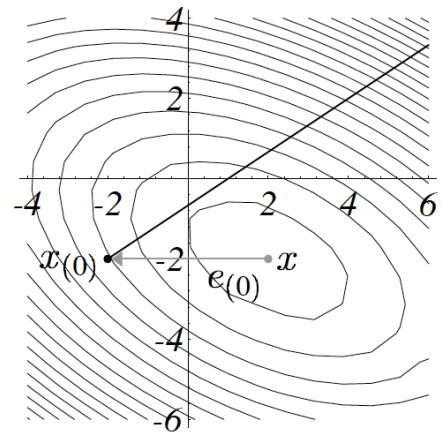

Figure A2-4 Direction of Initial Step for Example System

Once the direction is determined, the size of the step must be calculated. In the gradient descent approach, this is performed by looking at the values of ψ along the proposed direction and finding the minimum value.

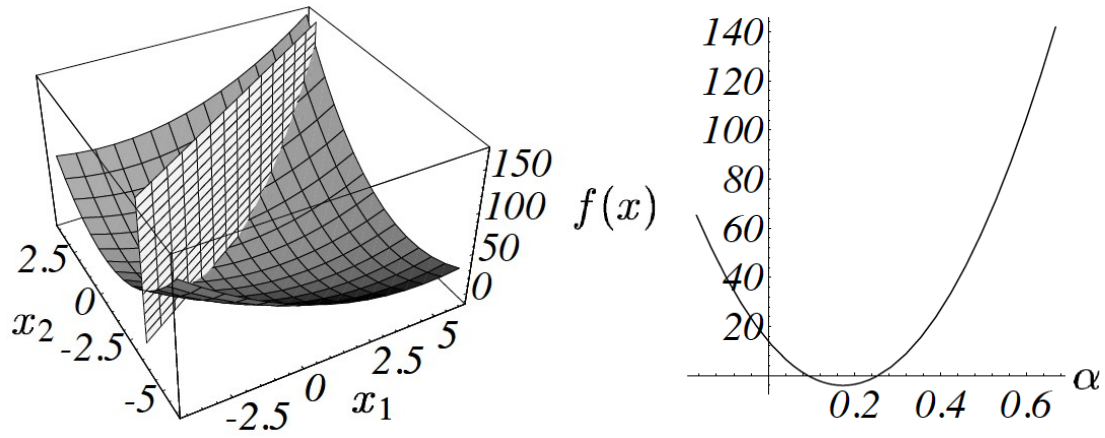

Figure A2-5 Value of ψ Along the Proposed Step Direction for Example System

The value of α which leads to the minimum value of ψ shown in Figure A2-5 can be found by determining when the direction derivative $\frac{d}{d\alpha}\psi(x_i)$ is equal to zero. The chain rule allows for this to be calculated as:

$$\frac{d}{d\alpha}\psi(x_i) = \psi'(x_i)^T \frac{d}{d\alpha} x_i = \psi'(x_i)^T r_{i-1} \qquad \text{[A2-6]}$$

The process of calculating α for the gradient descent approach is omitted for brevity. However, calculation of α results in steps which are orthogonal to the prior step direction. This can be seen below in the iterative steps according to the algorithm.

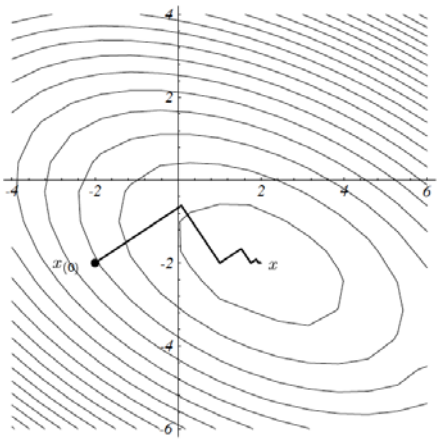

Figure A2-6 Series of Iterative Orthogonal Steps for Sovling the Example System

To briefly summarize, the gradient descent algorithm involves three key steps:

Calculate residual: $r_i = b - Ax_i$

Calculate α: $\alpha i = \frac{r_i^T r_i}{r_i^T A r_i}$

Calculate x: $x_{i+1} = x_i + a_i r_i$

The process of calculating the residua r, step size α, and new step x depends on the approach. More advanced methods (such as the conjugate gradient) use additional constraints to improve the direction and step calculation to improve the convergence properties of the algorithms.

Bibliography

1. Orozco-beltran D, Cooper RS, Gil-guillen V, Bertomeu-martinez V, Cea-calvo L, Pita-fernandez S, et al. Trends in Mortality From Myocardial Infarction. A Comparative Study Between Spain and the United States: 1990-2006. Rev Española Cardiol. 2012;65(12):1079–85.

2. Weisman HF, Healy B. Myocardial infarct expansion, infarct extension, and reinfarction: pathophysiologic concepts. Prog Cardiovasc Dis. 1987;30(2):73–110.

3. Erlebacher J a, Weiss JL, Weisfeldt ML, Bulkley BH. Early dilation of the infarcted segment in acute transmural myocardial infarction: role of infarct expansion in acute left ventricular enlargement. J Am Coll Cardiol. American College of Cardiology Foundation; 1984;4(2):201–8.

4. Eaton LW, Weiss JL, Bulkley BH, Garrison JB, Weisfeldt ML. Regional cardiac dilatation after acute myocardial infarction: recognition by two-dimensional echocardiography. N Engl J Med. UNITED STATES; 1979 Jan;300(2):57–62.

5. Roger VL, Go AS, Lloyd-Jones DM, Adams RJ, Berry JD, Brown TM, et al. Heart disease and stroke statistics--2011 update: a report from the American Heart Association. Circulation. 2011 Feb 1;123(4):e18–209.

6. Go AS, Mozaffarian D, Roger VL, Benjamin EJ, Berry JD, Borden WB, et al. Heart disease and stroke statistics-2013 update: A Report from the American Heart Association. Circulation. 2013;127(1).

7. Chen J, Normand S. National and regional trends in heart failure hospitalization and mortality rates for Medicare beneficiaries, 1998-2008. JAMA J …. 2011;306(15).

8. Jackson BM, Gorman JH, Moainie SL, Guy TS, Narula N, Narula J, et al. Extension of borderzone myocardium in postinfarction dilated cardiomyopathy. J Am Coll Cardiol. 2002;40(6):1160–7.

9. Lima J a, Becker LC, Melin J a, Lima S, Kallman C a, Weisfeldt ML, et al. Impaired thickening of nonischemic myocardium during acute regional ischemia in the dog. Circulation. 1985;71(5):1048–59.

10. Jackson BM, Gorman JH. Border zone geometry increases wall stress after myocardial infarction : contrast echocardiographic assessment. Am J …. 2003;(October 2002).

11. Kramer CM, Lima J a, Reichek N, Ferrari VA, Llaneras MR, Palmon LC, et al. Regional differences in function within noninfarcted myocardium during left ventricular remodeling. Circulation. 1993;88(3):1279–88.

12. Epstein FH, Yang Z, Gilson WD, Berr SS, Kramer CM, French B a. MR tagging early after myocardial infarction in mice demonstrates contractile dysfunction in adjacent and remote regions. Magn Reson Med. 2002;48(2):399–403.

13. Pilla JJ, Blom AS, Gorman JH, Brockman DJ, Affuso J, Parish LM, et al. Early Postinfarction Ventricular Restraint Improves Borderzone Wall Thickening Dynamics During Remodeling. Ann Thorac Surg. 2005 Dec;80(6):2257–62.

14. Blom AS, Pilla JJ, Arkles J, Dougherty L, Ryan LP, Gorman JH, et al. Ventricular Restraint Prevents Infarct Expansion and Improves Borderzone Function After Myocardial Infarction: A Study Using Magnetic Resonance Imaging, Three-Dimensional Surface Modeling, and Myocardial Tagging. Ann Thorac Surg. 2007 Dec;84(6):2004–10.

15. Ryan LP, Matsuzaki K, Noma M, Jackson BM, Eperjesi TJ, Plappert TJ, et al. Dermal Filler Injection: A Novel Approach for Limiting Infarct Expansion. 2009;87:148–55.

16. Koomalsingh KJ, Witschey WRT, McGarvey JR, Shuto T, Kondo N, Xu C, et al. Optimized Local Infarct Restraint Improves Left Ventricular Function and Limits Remodeling.

17. Jones RH, Velazquez EJ, Michler RE, Sopko G, Oh JK, O'Connor CM, et al. Coronary Bypass Surgery with or without Surgical Ventricular Reconstruction. N Engl J Med. 2009;360:1705–17.

18. Burkhoff D, Mirsky I, Suga H. Assessment of systolic and diastolic ventricular properties via pressure-volume analysis: a guide for clinical, translational, and basic researchers. Am J Physiol Heart Circ Physiol. 2005 Aug;289(2):H501–12.

19. Sagawa K, Suga H, Shoukas a a, Bakalar KM. End-systolic pressure/volume ratio: a new index of ventricular contractility. Am J Cardiol. 1977 Nov;40(5):748–53.

20. Suga H, Sagawa K, Shoukas a. a. Load Independence of the Instantaneous Pressure-Volume Ratio of the Canine Left Ventricle and Effects of Epinephrine and Heart Rate on the Ratio. Circ Res. 1973 Mar 1;32(3):314–22.

21. Suga H. Ventricular Energetics. Physiol Rev. 1990 Apr 1;70(2):247–77.

22. Kim RJ, Fieno DS, Parrish TB, Harris K, Chen E, Bundy J, et al. Irreversible Injury , Infarct Age , and Contractile Function. 2002;1992–2002.

23. Bers DM. Cardiac excitation-contraction coupling. 2002;415(January):198–205.

24. Lehman W, Craig R, Vibert P. Ca2+-induced tropomyosin movement in Limulus thin filaments revealed by three-dimensional reconstruction. Nature. 1994 Mar 3;368(6466):65–7.

25. Spudich J a. The myosin swinging cross-bridge model. Nat Rev Mol Cell Biol. 2001;2(5):387–92.

26. García X, Mateu L, Maynar J, Mercadal J, Ochagavía a., Ferrandiz a. Estimating cardiac output. Utility in the clinical practice. Available invasive and non-invasive monitoring. Med Intensiva (English Ed. 2011;35(9):552–61.

27. Goodman & Gilman's the pharmacological basis of therapeutics. 11th ed. /. New York: McGraw-Hill; 2006.

28. Suga H. Total mechanical energy of a ventricle model and cardiac oxygen consumption. Am J Physiol Circ Physiol. 1979;

29. Sinning D, Kasner M, Westermann D, Schulze K, Schultheiss H-P, Tschöpe C. Increased left ventricular stiffness impairs exercise capacity in patients with heart failure symptoms despite normal left ventricular ejection fraction. Cardiol Res Pract. 2011 Jan;2011(Lv):692862.

30. Baan J, van der Velde ET, de Bruin HG, Smeenk GJ, Koops J, van Dijk a. D, et al. Continuous measurement of left ventricular volume in animals and humans by conductance catheter. Circulation. 1984 Nov 1;70(5):812–23.

31. Lee W, Nakayama M, Huang W-P, Chiou K-R, Wu C-C, Nevo E, et al. Assessment of left ventricular end-systolic elastance from aortic pressure-left ventricular volume relations. Heart Vessels. 2002 Mar;16(3):99–104.

32. Schmitt B, Steendijk P, Lunze K, Ovroutski S, Falkenberg J, Rahmanzadeh P, et al. Integrated assessment of diastolic and systolic ventricular function using diagnostic cardiac magnetic resonance catheterization: validation in pigs and application in a clinical pilot study. JACC Cardiovasc Imaging. Elsevier Inc.; 2009 Nov;2(11):1271–81.

33. Bogen DK, Rabinowitz S a., Needleman A, McMahon T a., Abelmann WH. An analysis of the mechanical disadvantage of myocardial infarction in the canine left ventricle. Circ Res. 1980 Nov 1;47(5):728–41.

34. Tyberg J V., Forrester J, Wyatt HL, Goldner SJ, Parmley WW, Swan HJC. An Analysis of Segmental Ischemic Dysfunction Utilizing the Pressure-Length Loop. Circulation. 1974 Apr 1;49(4):748–54.

35. Theroux P, Ross J, Franklin D, Kemper WS, Sasyama S. Regional Myocardial function in the conscious dog during acute coronary occlusion and responses to morphine, propranolol, nitroglycerin, and lidocaine. Circulation. 1976 Feb 1;53(2):302–14.

36. Pagani M, Vatner SF, Baig H, Braunwald E. Initial myocardial adjustments to brief periods of ischemia and reperfusion in the conscious dog. Circ Res. 1978 Jul 1;43(1):83–92.

37. Oppelt A, Graumann R, Barfuss H, Fischer H. FISP—a new fast MRI sequence. Electromedica. 1986. p. 8.

38. Duerk JL, Lewin JS, Wendt M, Petersilge C. Remember true FISP? A high SNR, near 1-second imaging method for T2- like contrast in interventional MRI at .2 T. J Magn Reson Imaging. 1998;8(1):203–8.

39. Scheffler K, Hennig J. Is TrueFISP a gradient-echo or a spin-echo sequence? Magn Reson Med. 2003;49(2):395–7.

40. Home Tech Answers. Digital Camera Shutter Speed - Aperture and Shutter Speed [Internet]. 2015 [cited 2015 May 15]. Available from: http://www.hometechanswers.com/digital-photography/digital-cameras-shutter-speed.html

41. Lenz GW, Haacke EM, White RD. Retrospective cardiac gating: A review of technical aspects and future directions. Magn Reson Imaging. 1989;7:445–55.

42. Feinstein J a, Epstein FH, Arai a E, Foo TK, Hartley MR, Balaban RS, et al. Using cardiac phase to order reconstruction (CAPTOR): a method to improve diastolic images. J Magn Reson Imaging. 1997;7(5):794–8.

43. Larson AC, White RD, Laub G, McVeigh ER, Li D, Simonetti OP. Self-gated cardiac cine MRI. Magn Reson Med. 2004 Jan;51(1):93–102.

44. Burkhoff D. Mechanical Properties of the Heart and Its Iteration With the Vascular System. Columbia University; 2002.

45. Pruessmann KP, Weiger M, Börnert P, Boesiger P. Advances in sensitivity encoding with arbitrary k-space trajectories. Magn Reson Med. 2001 Oct;46(4):638–51.

46. Fessler J, Noll D. ITERATIVE RECONSTRUCTION METHODS FOR NON-CARTESIAN MRI. ISMRM Work Non-Cartesian MRI. 2007;

47. Hansen MS, Sorensen TS, Sørensen TS. Gadgetron: an open source framework for medical image reconstruction. Magn Reson Med. United States: Wiley Subscription Services, Inc., A Wiley Company; 2013 Jun;69(6):1768–76.

48. Pruessmann KP, Weiger M, Scheidegger MB, Boesiger P. SENSE: sensitivity encoding for fast MRI. Magn Reson Med. 1999/11/05 ed. Institute of Biomedical Engineering and Medical Informatics, University of Zurich and Swiss Federal Institute of Technology Zurich, Zurich, Switzerland.; 1999 Nov;42(5):952–62.

49. Sodickson DK, Manning WJ. Simultaneous acquisition of spatial harmonics (SMASH): Fast imaging with radiofrequency coil arrays. Magn Reson Med. 1997;38(4):591–603.

50. Walsh DO, Gmitro AF, Marcellin MW. Adaptive reconstruction of phased array MR imagery. Magn Reson Med. 2000 May;43(5):682–90.

51. Haacke EM, Brown RW, Thompson MR, Venkatesan R. Magnetic Resonance Imaging: Physical Principles and Sequence Design. Book. 1999. 914 p.

52. Block KT, Uecker M, Frahm J. Undersampled radial MRI with multiple coils. Iterative image reconstruction using a total variation constraint. Magn Reson Med. 2007 Jun;57(6):1086–98.

53. Bauer R, Radtke I, Block KT, Larson MC, Kerl JM, Hammerstingl R, et al. True real-time cardiac MRI in free breathing without ECG synchronization using a novel sequence with radial k-space sampling and balanced SSFP contrast mode. Int J Cardiovasc Imaging. 2013 Jun;29(5):1059–67.

54. Voit D, Zhang S. Real-time cardiovascular magnetic resonance at 1.5 T using balanced SSFP and 40 ms resolution. J Cardiovasc Magn Reson. Journal of Cardiovascular Magnetic Resonance; 2013 Sep;15(1):79.

55. Muthurangu V, Lurz P, Critchely JDJD, Deanfield JE, Taylor AM, Hansen MS. Real-time Assessment of Right and Left Ventricular Volumes and Function in Patients with Congenital Heart Disease by Using High Spatiotemporal Resolution Radial k-t SENSE. Radiology. United States; 2008 Sep;248(3):782–91.

56. Boll DT, Merkle E, Seaman D, Gilkeson RC, Larson AC, Simonetti O, et al. Comparison of ECG-Gated Rectilinear vs. Real-Time Radial K-Space Sampling Schemes in Cine True-FISP Cardiac MRI. J Cardiovasc Magn Reson. 2004 Dec 1;6(4):793–802.

57. Kühl HP, Spuentrup E, Wall A, Franke A. Assessment of Myocardial Function with Interactive Non–Breath-hold Real-time MR Imaging: Comparison with Echocardiography and Breath-hold Cine MR Imaging. Radiology. 2004;(231):198–207.

58. Spuentrup E, Schroeder J, Mahnken AH, Schaeffter T, Botnar RM, Kühl HP, et al. Quantitative Assessment of Left Ventricular Function with Interactive Real-Time Spiral and Radial MR Imaging1. Radiology. 2003;(227):870–6.

59. Sorensen T, Atkinson D. Real-time reconstruction of sensitivity encoded radial magnetic resonance imaging using a graphics processing unit. IEEE Trans Med Imaging. 2009;28(12):1974–85.

60. Yushkevich PA, Piven J, Hazlett HC, Smith RG, Ho S, Gee JC, et al. User-guided 3D active contour segmentation of anatomical structures: significantly improved efficiency and reliability. Neuroimage. 2006/03/21 ed. Penn Image Computing and Science Laboratory, Department of Radiology, University of Pennsylvania, PA 19104-6274, USA. pauly2@grasp.upenn.edu; 2006;31:1116–28.

61. Li H, Haltmeier M, Zhang S, Frahm J, Munk A. Aggregated motion estimation for real-time MRI reconstruction. Magn Reson Med. United States; 2014 Nov 18;72(4):1039–48.

62. Lurz P, Muthurangu V, Schuler PK, Giardini A, Schievano S, Nordmeyer J, et al. Impact of reduction in right ventricular pressure and/or volume overload by percutaneous pulmonary valve implantation on biventricular response to exercise: an exercise stress real-time CMR study. Eur Heart J. 2012 Oct;33(19):2434–41.

63. Jones A, Steeden J a, Pruessner JC, Deanfield JE, Taylor AM, Muthurangu V. Detailed assessment of the hemodynamic response to psychosocial stress using real-time MRI. J Magn Reson Imaging. 2011 Feb;33(2):448–54.

64. Seiberlich N, Lee GR, Ehses P, Duerk JL, Gilkeson RC, Griswold MA. Improved temporal resolution in cardiac imaging using through-time spiral GRAPPA. Magn Reson Med. 2011 Dec;66(6):1682–8.

65. Seiberlich N, Ehses P, Duerk JL, Gilkeson RC, Griswold MA. Improved radial GRAPPA calibration for real-time free-breathing cardiac imaging. Magn Reson Med. 2011 Feb;65(2):492–505.

66. Saybasili H, Derbyshire JA, Kellman P, Griswold M a, Ozturk C, Lederman RJ, et al. RT-GROG: parallelized self-calibrating GROG for real-time MRI. Magn Reson Med. 2010 Jul;64(1):306–12.

67. Uecker M, Zhang S, Voit D. Real-time MRI at a resolution of 20 ms. NMR Biomed. 2010 Oct;23(8):986–94.

68. Uecker M, Zhang S, Frahm J. Nonlinear inverse reconstruction for real-time MRI of the human heart using undersampled radial FLASH. Magn Reson …. 2010 Jun;63(6):1456–62.

69. Zhang S, Uecker M, Voit D, Merboldt K, Frahm J. Real-time cardiovascular magnetic resonance at high temporal resolution : radial FLASH with nonlinear inverse reconstruction. J Cardiovasc Magn Reson. 2010 Jan;12:39.

70. Zhang S, Block KT, Frahm J. Magnetic resonance imaging in real time: advances using radial FLASH. J Magn Reson Imaging. 2010 Jan;31(1):101–9.

71. Lurz P, Muthurangu V, Schievano S, Nordmeyer J, Bonhoeffer P, Taylor AM, et al. Feasibility and reproducibility of biventricular volumetric assessment of cardiac function during exercise using real-time radial k-t SENSE magnetic resonance imaging. J Magn Reson Imaging. 2009 May;29(5Radia):1062–70.

72. Winkelmann S, Schaeffter T, Koehler T, Eggers H, Doessel O. An optimal radial profile order based on the Golden Ratio for time-resolved MRI. IEEE Trans Med Imaging. 2007 Jan;26(1):68–76.

73. Spuentrup E, Mahnken AH, Kühl HP, Krombach G a, Botnar RM, Wall A, et al. Fast interactive real-time magnetic resonance imaging of cardiac masses using spiral gradient echo and radial steady-state free precession sequences. Invest Radiol. 2003 May;38(5):288–92.

74. Larson AC, Simonetti OPO. Real-time cardiac cine imaging with SPIDER: Steady-state projection imaging with dynamic echo-train readout. Magn Reson Med. 2001 Dec;46(6):1059–66.

75. Shankaranarayanan A, Simonetti O. Segmented k-Space and Real-Time Cardiac Cine MR Imaging with Radial Trajectories. Radiology. 2001;827–36.

76. Contijoch F, Witschey WR, Rogers K, Rears H, Hansen MS, Yushkevich PA, et al. User-Initialized Active Contour Segmentation and Golden-angle Real-Time Cardiac MRI Enable Accurate Assessment of LV Function in Patients with Sinus Rhythm and Arrhythmias. J Cardiovasc Magn Reson. 2015;17(37):In Press.

77. Zhu SC, Lee TS, Yuille AL. Region competition: unifying snakes, region growing, energy/Bayes/MDL for multi-band image segmentation. Computer Vision, 1995. Proceedings., Fifth International Conference on. 1995. p. 416–23.

78. Setser R. Quantification of left ventricular function with magnetic resonance images acquired in real time. J Magn Reson Imaging. 2000;438:430–8.

79. Song HK, Dougherty L. k-space weighted image contrast (KWIC) for contrast manipulation in projection reconstruction MRI. Magn Reson Med. 2000 Dec;44(6):825–32.

80. Lee VS. Cardiovascular MRI: Physical Principles to Practical Protocols. Lippincott Williams & Wilkins; 2006. 295 p.

81. Contijoch F, Han Y, Berisha S, Pilla JJ, Gorman RC, Gorman JH, et al. Retrospective cine MRI reconstruction of multiple beat morphologies in the presence of arrhythmias. Magn Reson Med. 2015;In Revision.

82. Winkelmann S, Schaeffter T, Koehler T, Eggers H, Doessel O. An optimal radial profile order based on the Golden Ratio for time-resolved MRI. IEEE Trans Med Imaging. 2007;26(1):68–76.

83. Jackson JI, Meyer CH, Nishimura DG, Macovski A. Selection of a convolution function for Fourier inversion using gridding [computerised tomography application]. IEEE Trans Med Imaging. 1991 Jan;10(3):473–8.

84. Fessler J, Sutton B. Nonuniform fast Fourier transforms using min-max interpolation. Signal Process IEEE Trans …. 2003;51(2):560–74.

85. Witschey WRT, Contijoch F, McGarvey JR, Ferrari VA, Hansen MS, Lee ME, et al. Real-Time Magnetic Resonance Imaging Technique for Determining Left Ventricle Pressure-Volume Loops. Ann Thorac Surg. Elsevier; 2014 Nov 25;97(5):1597–603.

86. Yushkevich PA, Piven J, Hazlett HC, Smith RG, Ho S, Gee JC, et al. User-guided 3D active contour segmentation of anatomical structures: Significantly improved efficiency and reliability. Neuroimage. 2006;31(3):1116–28.

87. Zhu S, Yuille A. Region Competition: Unifying Snakes, Region Growing, and Bayes/MDL for Multiband Image Segmentation. IEEE Trans Pattern Anal Mach Intell. 1996;18(9).

88. Bacharach S, Bonow R, Green M. Comparison of fixed and variable temporal resolution methods for creating gated cardiac blood-pool image sequences. J Nucl Med …. 1990;(31):38–42.

89. Muthurangu V, Lurz P, Critchely JD. Real-time Assessment of Right and Left Ventricular Volumes and Function in Patients with Congenital Heart Disease by Using High Spatiotemporal Resolution Radial k-t SENSE. Radiology. 2008;248(3).

90. Hansen MS, Sørensen TS, Arai AE, Kellman P. Retrospective reconstruction of high temporal resolution cine images from real-time MRI using iterative motion correction. Magn Reson Med. 2012 Sep 21;68(3):741–50.

91. Glover GH, Pelc NJ. A rapid-gated cine MRI technique. Magn Reson Annu. UNITED STATES; 1988;299–333.

92. Klem I, Heitner JF, Shah DJ, Sketch MH, Behar V, Weinsaft J, et al. Improved Detection of Coronary Artery Disease by Stress Perfusion Cardiovascular Magnetic Resonance With the Use of Delayed Enhancement Infarction Imaging. J Am Coll Cardiol. 2006;47(8):1630–8.

93. Wieling W. Heart rate variability in healthy subjects: effect of age and the derivation of normal ranges for tests of autonomic function. Br Heart J. 1987;57:109–10.

94. Garrard CL, Weissler a M, Dodge HT. The relationship of alterations in systolic time intervals to ejection fraction in patients with cardiac disease. Circulation. 1970;42(3):455–62.

95. Contijoch F, Han Y, Hansen MS, Kellman P, Gualtieri G, Elliott M, et al. Continuous adaptive radial sampling of k-space from real- time physiologic feedback in MRI. Magn Reson Med: 2015;In Revision.

96. Lauzon ML, Lauzon ML, Rutt BK, Rutt BK. Effects of polar sampling in k-space. Magn Reson Med. 1996;36(6):940–9.

97. Otazo R, Kim D. Combination of compressed sensing and parallel imaging for highly accelerated first-pass cardiac perfusion MRI. Magn Reson Med. 2010;776:767–76.

98. Lustig M, Donoho D, Pauly JM. Sparse MRI: The application of compressed sensing for rapid MR imaging. Magn Reson Med. 2007 Dec;58(6):1182–95.

99. Suga H. Time course of left ventricular pressure-volume relationship under various enddiastolic volume. Jpn Heart J. JAPAN; 1969 Nov;10(6):509–15.

100. Suga H, Sagawa K. Instantaneous pressure-volume relationships and their ratio in the excised, supported canine left ventricle. Circ Res. 1974;35(1):117–26.

101. Sagawa K. The end-systolic pressure-volume relation of the ventricle: definition, modifications and clinical use. Circulation. 1981;63(6):1223–7.

102. Glower DD, Spratt JA, Snow ND, Kabas JS, Davis JW, Olsen CO, et al. Linearity of the Frank-Starling relationship in the intact heart: the concept of preload recruitable stroke work. Circulation. 1985 May 1;71(5):994–1009.

103. Pattynama P, Roos A. Magnetic resonance imaging analysis of left ventricular pressure-volume relations: Validation with the conductance method at rest and during dobutamine stress. Magn Reson Med. 1995;di:728–37.

104. Kuehne T, Yilmaz S, Steendijk P, Moore P, Groenink M, Saaed M, et al. Magnetic resonance imaging analysis of right ventricular pressure-volume loops: In vivo validation and clinical application in patients with pulmonary hypertension. Circulation. 2004;110(14):2010–6.

105. Jerzewski A, Steendijk P, Pattynama PMT, Leeuwenburgh BPJ, De Roos A, Baan J. Right ventricular systolic function and ventricular interaction during acute embolisation of the left anterior descending coronary artery in sheep. Cardiovasc Res. 1999;43(1):86–95.

106. Dell'Italia LJ, Blackwell GG, Urthaler F, Pearce DJ, Pohost GM. A stable model of left ventricular dysfunction in an intact animal assessed with high fidelity pressure and cinemagnetic resonance imaging. Cardiovasc Res. 1993;27(6):974–9.

107. Witschey WRT, Contijoch F, McGarvey JR, Ferrari VA, Hansen MS, Lee ME, et al. Real-Time Magnetic Resonance Imaging Technique for Determining Left Ventricle Pressure-Volume Loops. Ann Thorac Surg. Elsevier; 2015 Jan 28;97(5):1597–603.

108. Pruessmann K, Weiger M. Advances in sensitivity encoding with arbitrary k-space trajectories. Magn Reson …. 2001;651:638–51.

109. Schmitt B, Steendijk P, Lunze K, Ovroutski S, Falkenberg J, Rahmanzadeh P, et al. Integrated assessment of diastolic and systolic ventricular function using diagnostic cardiac magnetic resonance catheterization: validation in pigs and application in a clinical pilot study. JACC Cardiovasc Imaging. 2009;2:1271–81.

110. Velde E Van der, Burkhoff D, Steendijk P. Nonlinearity and load sensitivity of end-systolic pressure-volume relation of canine left ventricle in vivo. Circulation. 1991;315–27.

111. Macron L, Lim P, Bensaid A, Nahum J, Dussault C, Mitchell-Heggs L, et al. Single-beat versus multibeat real-time 3d echocardiography for assessing left

ventricular volumes and ejection fraction: A comparison study with cardiac magnetic resonance. Circ Cardiovasc Imaging. 2010;3(4):450–5.

112. Schmitt B, Steendijk P, Ovroutski S, Lunze K, Rahmanzadeh P, Maarouf N, et al. Pulmonary vascular resistance, collateral flow, and ventricular function in patients with a fontan circulation at rest and during dobutamine stress. Circ Cardiovasc Imaging. 2010;3(5):623–31.

113. Körperich H, Gieseke J, Barth P, Hoogeveen R, Esdorn H, Peterschröder A, et al. Flow Volume and Shunt Quantification in Pediatric Congenital Heart Disease by Real-Time Magnetic Resonance Velocity Mapping: A Validation Study. Circulation. 2004;109(16):1987–93.

114. Kass DA, Yamazaki T, Burkhoff D, Maughan WL, Sagawa K. Determination of left ventricular end-systolic pressure-volume relationships by the conductance (volume) catheter technique. Circulation. 1986 Mar 1;73(3):586–95.

115. Kass DA, Maughan WL, Guo ZM, Kono A, Sunagawa K, Sagawa K. Comparative influence of load versus inotropic states on indexes of ventricular contractility: experimental and theoretical analysis based on pressure-volume relationships. Circulation. 1987 Dec 1;76(6):1422–36.

116. Kass DA, Marino P, Maughan WL, Sagawa K. Determinants of end-systolic pressure-volume relations during acute regional ischemia in situ. Circulation. 1989 Dec 1;80(6):1783–94.

117. Contijoch F, Witschey WR, McGarvey JR, Lee M, Gorman JH, Gorman RC, et al. Slice-by-slice PV loop analysis demonstrates native differences in regional cardiac contractility and response to inotropic agents. Am J Physiol - Hear Circ Physiol. :In Preparation.

118. Burkhoff D, van der Velde E, Kass DA, Baan J, Maughan WL, Sagawa K. Accuracy of volume measurement by conductance catheter in isolated, ejecting canine hearts. Circulation. 1985 Aug 1;72(2):440–7.

119. Kass DA. Clinical evaluation of left heart function by conductance catheter technique. Eur Heart J. 1992 Nov;13 Suppl E:57–64.

120. Contijoch F, Rogers K, Avants B, Yushkevich P, Hoshmand V, Gorman RC, et al. Quantification of left ventricular deformation fields from undersampled radial, real-time cardiac MRI. J Cardiovasc Magn Reson. BioMed Central Ltd; 2014;16(Suppl 1):P366.

121. Avants B, Tustison NJ, Song G, Cook PA, Klein A, Gee JC. A reproducible evaluation of ANTs similarity metric performance in brain image registration. Neuroimage. 2010/09/21 ed. Penn Image Computing and Science Laboratory, University of Pennsylvania, Philadelphia, PA 19104, USA. avants@grasp.cis.upenn.edu; 2011;54:2033–44.

122. Horn BKP, Schunck BG. Determining optical flow. Artif Intell. 1981 Aug;17(1-3):185–203.

123. Avants BB, Yushkevich P, Pluta J, Minkoff D, Korczykowski M, Detre J, et al. The optimal template effect in hippocampus studies of diseased populations. Neuroimage. Elsevier Inc.; 2010;49(3):2457–66.

124. Contijoch F, Witschey WRT, Mcgarvey J, Lee M, Kondo N, Shimaoka T, et al. Regional Frank-Starling relations in infarcted swine via dynamic real-time MRI. ISMRM 2014 Annu Meet.

125. Sacks MS. Biaxial mechanical evaluation of planar biological materials. J Elast. 2000;61(1-3):199–246.

126. Morita M, Eckert CE, Matsuzaki K, Noma M, Ryan LP, Burdick J a., et al. Modification of infarct material properties limits adverse ventricular remodeling. Ann Thorac Surg. Elsevier Inc.; 2011;92(2):617–25.

127. Cha Y-M, Lee GK, Klarich KW, Grogan M. Premature ventricular contraction-induced cardiomyopathy: a treatable condition. Circ Arrhythm Electrophysiol. 2012 Feb;5(1):229–36.

128. Chia J, Fischer S. Performance of QRS detection for cardiac magnetic resonance imaging with a novel vectorcardiographic triggering method. J Magn Reson Imaging. 2000 Nov;12(5):678–88.

129. Contijoch F, Rogers K, Rears H, Kellman P, Gorman JH, Gorman RC, et al. Quantification of LV function pre, during, and post premature ventricular complexes reveals variable hemodynamics. J Am Coll Cardiol. 2015;In Review.

130. Pan J, Tompkins WJ. A real-time QRS detection algorithm. IEEE Trans Biomed Eng. 1985;32(3):230–6.

131. Del Carpio Munoz F, Syed FF, Noheria A, Cha Y-M, Friedman P a., Hammill SC, et al. Characteristics of premature ventricular complexes as correlates of reduced left ventricular systolic function: Study of the burden, duration, coupling interval, morphology and site of origin of PVCs. J Cardiovasc Electrophysiol. 2011;22(7):791–8.

132. Bogun F, Crawford T, Reich S, Koelling TM, Armstrong W, Good E, et al. Radiofrequency ablation of frequent, idiopathic premature ventricular complexes: Comparison with a control group without intervention. Hear Rhythm. Elsevier; 2007 Apr 13;4(7):863–7.

133. Sekiguchi Y, Aonuma K, Yamauchi Y, Obayashi T, Niwa A, Hachiya H, et al. Chronic hemodynamic effects after radiofrequency catheter ablation of frequent monomorphic ventricular premature beats. J Cardiovasc Electrophysiol. 2005;16(10):1057–63.

134. Olgun H, Yokokawa M, Baman T, Kim HM, Armstrong W, Good E, et al. The role of interpolation in PVC-induced cardiomyopathy. Hear Rhythm. Elsevier Inc.; 2011;8(7):1046–9.

135. Sun Y, Blom N a., Yu Y, Ma P, Wang Y, Han X, et al. The influence of premature ventricular contractions on left ventricular function in asymptomatic children without structural heart disease: An echocardiographic evaluation. Int J Cardiovasc Imaging. 2003;19(4):295–9.

136. Akoum NW, Daccarett M, Wasmund SL, Hamdan MH. An animal model for ectopy-induced cardiomyopathy. PACE - Pacing Clin Electrophysiol. 2011;34(3):291–5.

137. Huizar JF, Kaszala K, Potfay J, Minisi AJ, Lesnefsky EJ, Abbate A, et al. Left ventricular systolic dysfunction induced by Ventricular Ectopy: A novel model for premature ventricular contraction-induced cardiomyopathy. Circ Arrhythmia Electrophysiol. 2011;4(4):543–9.

138. Hamlet SM, Wehner GJ, Suever JD, Powell D, Haggerty CM, Jing L, et al. Effect of variable breath-hold positions during cardiac magnetic resonance on measures of left ventricular mechanics. J Cardiovasc Magn Reson. BioMed Central; 2014 Jan 16;16(Suppl 1):P78–P78.

139. Yarlagadda RK, Iwai S, Stein KM, Markowitz SM, Shah BK, Cheung JW, et al. Reversal of cardiomyopathy in patients with repetitive monomorphic ventricular ectopy originating from the right ventricular outflow tract. Circulation. 2005;112(8):1092–7.